NORTHWESTERN UNIVERSITY

Studies on DC-Driven Single and Multiterminal Josephson Junctions

A DISSERTATION

SUBMITTED TO THE GRADUATE SCHOOL
IN PARTIAL FULFILLMENT OF THE REQUIREMENTS

for the degree

DOCTOR OF PHILOSOPHY

Field of Physics and Astronomy

By

Maxwell Wisne

EVANSTON, ILLINOIS

February 2026

ABSTRACT

Since its discovery over 60 years ago, the Josephson junction has provided an invaluable experimental tool to the superconductivity community. State-of-the-art superconducting qubits deployed en masse today could not exist without the nonlinear Josephson element — a sentiment echoed by this year's Nobel prize in physics.

Despite its promotion to industry frontlines, the Josephson junction continues to be of interest in the academic setting, especially for its role in decoherence mechanisms. In this thesis, we study the low-frequency transport characteristics of Josephson junctions intended for use in transmon qubits. We find an unexpected commonality in the data across a variety of junctions suggesting that the intrinsic capacitance plays an important role in phase fluctuations.

The conceptual simplicity of the Josephson junction affords a degree of fabrication flexibility, allowing experimentalists to adapt junctions to a variety of use cases in superconducting circuits. We show that multiterminal junctions fabricated from diffusive normal metal wire display a range of interesting phenomena arising from the proximity effect, including correlated Josephson effects in four-terminal junctions and topologically non-trivial states in three-terminal junctions.

ACKNOWLEDGMENTS

Most prominently, I thank my advisor, Venkat Chandrasekhar, for his encouragement, investment, and nurturing of my scientific abilities over the last 78 months. I know of no other person who pursues with greater intent the success of his students, academically and professionally. You've taught me the importance of attention to detail, and you've demonstrated leadership through difficult times. Never once did I think I couldn't do it. Because of you, I would do it all again.

My entry into Northwestern's physics department happened in no small part thanks to my friends Kevin Ryan and Patrick Krantz, who, after toiling for many hours in Tech have still never beat me at cards. To Patrick, I'm grateful for your patient mentorship, especially now after reminding new students to turn off the soldering iron. To Kevin, I can't think of anyone with whom I'd rather tag-team SQMS meetings — the bond we've formed is stronger than Niobium.

I also thank Yanpei Deng, who will have to generously restock office chocolates for someone else now (sad), Austin Marga, whose penchant for dairy is second only his sense of humor, and John Scott, whose duty to the lab is second only to his loyalty to fellow condensed-matter students.

Ever a work in progress, I thank the mentors who have shaped me as a student: Ms. Lisa Lemon, who taught me the unit circle (Eq. (2.2) is for you!); Ms. Rachel Turk, from whom I beg forgiveness for every "is" used passively in this thesis; Ms. Jennifer Patton, whose strict quota on exclamation marks continues to guide my emails; Prof. Elizabeth Hewitt, who taught me *Moby Dick* with such enthusiasm I *nearly* choose English over physics; and Mr. Rick Tivers, without whom my life would be far, far more concrete.

Outside of the lab, I thank the people who kept me *me*. To Aidan Falk, Esq., you made home and Chicago one and the same. Together, we faked it until we made it. To Nick Harvey, for 10 years you've been the base to my acid. Or something — you're the chemist. To Dee Wisne,

you modeled hard work before I ever solved an integral, and to Lydia Wisne, you've shown more enthusiasm for research than I could ever muster. I'm so proud.

To my girlfriend, Emma Westbrook, always the good sport, the down-for-anything, the patient, loving and generous, you were the first person to show enthusiasm for my little metal wires, and the last person to read my *entire thesis* for clarity. You filled me up outside the lab so I could pour myself out inside. Your kindness is boundless.

And lastly, to my parents, Ms. Bridgette Mariea and Mr. Joseph Wisne, the mountains on which I stand. Dad, I've never wondered if you're proud because you made sure I never had to. You put the crowbar in my hands so that one day I might wield the Gravity Gun. Mama, from my first visit to NU 13 years ago to taking my picture in the lab last month, you've never missed a time when I needed you. A son couldn't ask for more.

To you two, I dedicate this thesis.

TABLE OF CONTENTS

LIST OF FIGURES

LIST OF TABLES

CHAPTER 1
INTRODUCTION

Mesoscopic physics explores the intersection between quantum physics and classical mechanics. One-dimensional (1D) metallic wires are a natural platform to perform measurements on such a scale. At low temperatures, certain metals exhibit the phenomenon of superconductivity which allows the construction of mesoscopic devices consisting of both superconducting and non-superconducting materials placed in direct contact. Josephson predicted [1] that when two superconductors are separated by a thin insulating barrier, dissipationless supercurrent could flow between them without an applied voltage. This *Josephson effect* was later generalized to include superconducting electrodes weakly connected by *any* link, such as a normal metal. In this case, the superconductor imparts its characteristics into the normal metal via the proximity effect, inducing a "minigap" in the electronic density of states (DOS), and enabling supercurrent to flow across several *microns* of normal metal. From a fabrication standpoint, the superconducting-normal metal-superconducting (SNS) junction has the distinct advantage of being long enough to allow room for additional superconducting wires to couple to the common piece of normal metal, transforming a single Josephson junction (JJ) into a *multiterminal* JJ, the physics of which is much less studied.

Central to this thesis is the junction current-phase relation (CPR) which, as the name suggests, describes the supercurrent I_s as a function of the superconducting phase difference ϕ imposed across the junction. In an ideal SIS junction, this relationship is $I_s = I_c \sin(\phi)$ where I_c is the maximum allowed supercurrent. The CPR gives JJs tremendous utility in superconducting qubits where a degree of nonlinearity is required for their operation. Such Josephson-based qubits show great promise as scalable solid-state quantum computers despite suffering from limited coherence

times. While a global effort is underway to improve the performance of these qubits by eliminating materials-level sources of energy dissipation, this thesis is concerned with understanding limitations inherent to the qubit junction itself.

In multiterminal SNS junctions where the CPR deviates from a pure sinusoidal form, we seek a more *fundamental* understanding of the interplay between more than one phase difference. This is done by driving multiple supercurrents simultaneously or by directly phase-biasing the device. In either case, the voltage response of the junction is measured either directly across a pair of superconducting leads, or across a segment of normal metal wire coupled to the junctions.

The Josephson effect in SIS JJs is often explained using a macroscopic approach. We treat them distinctly from the SNS JJs, which are described by a microscopic quasiparticle-mediated charge-transfer process inside the normal metal. Consequently, the theoretical background and experimental sections involving SIS junctions are separated from analogous sections on SNS junctions. The unifying characteristic of this work, however, is the low-frequency transport measurement performed on all devices.

The chapters of this thesis are broken down into the following.

Chapter 2 discusses the background theory on SIS Josephson junctions typically found in superconducting qubits. The phenomenological framework needed to motivate the study of small-junction current-voltage characteristics is established.

Chapter 3 includes a theoretical description of SNS junctions using the quasiclassical Green's function approach. The model described here incorporates multiterminal JJs into the picture.

Chapter 4 contains a description of the experimental methods used in device fabrication and a discussion of the all measurement techniques performed.

Chapter 5 includes experimental results on SIS junctions fabricated for use in superconducting qubits. We suggest possible areas of further study in single SIS JJs.

Chapter 6 includes experimental results on single and multiterminal SNS junctions. A variety of device geometries and measurements are discussed.

In Chapter 7 we provide concluding remarks and suggestions for further study.

CHAPTER 2

THEORY: SIS JUNCTIONS

The first published current-voltage (IV) curve of a Josephson junction appeared in 1963 [2]. The junction was fabricated with 200-nm-thick superconducting films of Sn and Pb separated by a PbO_x barrier. The overlapping area of the junction was rough 250×650 μm^2, giving a normal state resistance R_N of $0.4\ \Omega$. From a mesoscopic physics point of view, this junction was massive. When current-biased up to 650 μA, *zero* voltage was measured across the junction. Exceeding this current resulted in a sudden jump to a finite voltage which eventually resolved into a perfectly linear slope corresponding to R_N. These few key features of the IV curve — the zero-voltage state at small current, the transition to a finite voltage at some particular higher current, and the linear voltage response that follows — define the *fingerprint* of a dc-current-biased JJ.

As fabrication technology became more precise, JJs became smaller. The area A of overlap between the top and bottom superconducting electrodes shrunk. Today, in junctions used as the essential circuit element in superconducting quantum computers, $A < 1$ μm^2 [3]. In these small JJs, while the overall IV fingerprint remains, several additional features reflecting the quantum character of the junctions have appeared. Among these are the emergence of a *resistance* in the nominally pure superconducting region of the IV and a *premature switch* into the finite voltage state, a phenomenon central to the recently awarded Nobel Prize in Physics [4], [5]. The Nobel-recognized experiments paved the way for early Josephson-based qubits [6], [7], which eventually evolved into the field of solid-state quantum information.

At the heart of the superconducting qubit boom endures the humble Josephson junction to which the field owes much of its success and, importantly for us, about which there is much

yet to be discovered. It is the goal of this theory chapter to build the framework needed to analyze dc-current-driven JJs in the context of superconducting qubits. Given most qubits today undergo microwave readout measurements, the traditional IV curve is largely ignored in this field. Nonetheless, we believe that valuable information about superconducting qubits, specifically in the transmon configuration, may be gained from good old-fashioned dc transport.

2.1 Josephson phase parameters

In SIS JJs, supercurrent *tunnels* from one superconducting electrode to another in the absence of a voltage. Unlike quasiparticle tunneling, which we discuss in the next section, supercurrent tunneling does not primarily involve excitations. One may think of supercurrent transported across an insulating barrier as a result of the spatial distribution of the superconducting wave function. Due to the suppression of the order parameter at the insulator-superconductor interface, coupling between superconductors occurs only for an insulator thickness $d \sim 1$ nm.

In order to describe the basic phenomenology of a junction, we must examine the phase dynamics of the superconducting condensate order parameter wavefunction

$$\Psi = |\Psi(\vec{r})|\exp(i[\phi_n(\vec{r})]) \tag{2.1}$$

with ϕ_n representing the phase of the nth superconducting electrode and $\vec{r}$ the position vector. Since the phases of the two superconducting reservoirs are arbitrarily defined, we are concerned only with the difference between them. That is, the phase difference $\Delta\phi = \phi_1 - \phi_2$ between superconducting electrode 1 and electrode 2 contains information needed to determine the tunneling supercurrent. Without loss of generality, we may define $\phi_1 = 0$ and $\phi_2 = \phi$ such that, throughout this thesis, ϕ stands for the phase difference between two spatially separated superconductors.

2.1.1 Josephson relations

In 1962, Brian Josephson predicted that supercurrent would flow across a thin insulating barrier according to

$$I_s = I_c \sin(\phi) \tag{2.2}$$

and, if a voltage *was* maintained across the junction, the phase would evolve with time t as

$$V = \frac{\hbar}{2e}\frac{d\phi}{dt} \tag{2.3}$$

Commonly referred to as the CPR, Eq. (2.2) and its inverse $\phi = \sin^{-1}(I_s/I_c)$ are frequently leveraged in experiments attempting to probe the effect of ϕ on measurable junction characteristics. When a small dc supercurrent $I_s < I_c$ is driven across an SIS junction, time-evolution of the phase, and thus the voltage, is zero. The maximum allowed supercurrent across the junction is referred to as the *critical current*, I_c. The exact value of I_c depends on intrinsic physical characteristics of the junction such as barrier thickness, junction area and the density of superconducting charge carriers in the electrodes.

In this thesis, we will not be considering voltage-biased junctions for the following reason. According to Eq. (2.3), applying a dc voltage linearly time-evolves the phase at currents $I_s < I_c$ which, when substituted into Eq. (2.2), results in an ac supercurrent response whose frequency depends on the magnitude of applied voltage. This so-called ac Josephson effect has applications in the frequency-volt conversion standard but lies outside the scope of this thesis. The experiments discussed in this work focus solely on current- and phase-biased junctions.

2.1.2 Josephson junction energy scales

By integrating Eq. (2.2) and (2.3) together in time, one finds the electrical work done by a current source in changing the phase

$$E_J = \int I_s \left(\frac{\hbar}{2e}\right)\, d(\Delta\phi) = I_c \left(\frac{\hbar}{2e}\right) \cos(\phi) \tag{2.4}$$

referred to as the *Josephson coupling energy*. In the literature, the coupling energy is often evaluated at its phase-independent maximum value, $E_J = \hbar I_c/2e$ [8]. For the remainder of this chapter, we accordingly view E_J *as proportional to* I_c. This simple relation is important to keep in mind throughout this thesis. To give a sense of numbers, for many SIS junctions designed for qubits, the value of E_J is $\sim 1 - 10$ GHz ($\sim 4 - 40$ μeV) [3]. The corresponding expected value of I_c is therefore on the order of 10 nA.

At low temperatures T, other relevant energy scales include the thermal energy $E_T = k_b T$ and the Coulomb charging energy $E_C = e^2/2C_\Sigma$ where C_Σ signifies the total capacitance of the device. The intrinsic junction capacitance $C < C_\Sigma$ of JJs frequently utilized in superconducting qubits is quite small, about 10 fF. The large charging energy places these junctions in the so-called *quantum* regime defined by $E_T < E_J \sim E_C$. Here, the quantum conjugate properties of ϕ and the charge number N play a significant role in the junction dynamics, and the IV curve develops certain endemic features exclusive to junctions of this size, henceforth referred to as "small" junctions.

A rough estimate for E_C of a particular junction with area A may be calculated through a simple parallel-plate capacitance formula $C = \epsilon A/d$ where d and ϵ is the barrier thickness and dielectric constant, respectively. Conversely, estimating I_c, and by extension, E_J, requires knowledge about the superconducting order parameter. The full temperature dependence of the (large) Josephson junction critical current I_c was worked out using microscopic theory in 1963 by Ambegaokar and

Baratoff [9] to be

$$I_c R_N = \left(\frac{\pi\Delta}{2e}\right) \tanh\left(\frac{\Delta}{2k_b T}\right) \tag{2.5}$$

As $T \to 0$, Eq. (2.5) reduces to $I_c R_N = \pi\Delta(T=0)/2e$, or, in terms of the Josephson energy,

$$E_J = \left(\frac{h}{8e^2}\right)\left(\frac{\Delta}{R_N}\right) \tag{2.6}$$

which is particularly important for designing qubits. Since the qubit excitation frequency $\omega_q \propto \sqrt{E_J}$, one may approximate ω_q *before* cooling the qubit to mK temperatures. A familiar workflow first assumes a particular superconductor gap Δ for the junction material of choice, typically Nb, Ta or Al, and a measurement of R_N at room temperature is made to estimate E_J [3].

2.2 Quasiparticle tunneling between superconductors

A more precise experimental determination of E_J comes from examining the quasiparticle contribution to the low-temperature IV curve. In fact, because measurements of Josephson junctions occur at finite temperatures, any discussion of tunneling in superconductors is incomplete without incorporating thermally activated quasiparticles. We take a brief moment now to describe the quasiparticle contribution to JJ IV curve. For a more thorough discussion of quasiparticle transport in superconducting tunnel junctions measured in this lab, see Ref. [10].

Quasiparticles are elementary excitations above the superconducting condensate. The density of states (DOS) of quasiparticle excitations inside the superconductor is given by [11]

$$\begin{cases} N_s(E) = N_n(0)E/(E^2+\Delta^2)^{1/2} & |E| \geq \Delta \\ N_s(E) = 0 & |E| < \Delta \end{cases} \tag{2.7}$$

where $N(0)$ represents the DOS in the normal state, and E is the quasiparticle excitation energy evaluated above the gap Δ. The probability of a thermally excited quasiparticle with energy E tunneling into an adjacent superconductor depends on the probability that the available state is not occupied by condensate electron pairs. The factors $N_s f\, dE$ and $N_s(1-f)\, dE$ give the numbers of occupied and empty states, respectively, where $f = (e^{E/k_b T} + 1)^{-1}$ is the usual Fermi distribution function. Clearly, then, quasiparticle tunneling is a temperature-dependent process. The sharp increase in $N_s(E)$ above Δ in Eq. (2.7) is responsible for a sharp non-linearity in the IV curve shown in Fig. 2.1(b).

It is convenient to represent these excitations at finite temperature in a "semiconductor model" shown in Fig. 2.1(a). Here, energy from the bias voltage eV shifts the Fermi energy of the superconducting electrodes with respect to one another. At $T > 0$, the result is a subgap current across the junction that tails off toward the purely superconducting part of the IV. At higher temperatures, more quasiparticles are thermally promoted above the gap and the tail broadens.

The net quasiparticle current across the junction is found by integrating the number of occupied states with the number of available states in an energy interval [8]. This results in a quasiparticle current

$$I_{qp} = \frac{1}{eR_N} \int_{-\infty}^{\infty} \frac{|E|}{|E^2 - \Delta^2|^{1/2}} \frac{|E + eV|}{|(E + eV)^2 - \Delta^2|^{1/2}} [f(E) - f(E + eV)]\, dE \qquad (2.8)$$

where values of $|E| < |\Delta|$ are excluded. The qualitative features of Eq. (2.8) are depicted in an IV curve in Fig. 2.1(b) (where the gaps Δ_1, Δ_2 of the electrodes are not the same). Since $N_s(E)$ is infinite at the gap edge, there is a discontinuous jump in I_{qp} at $V = (\Delta_1 + \Delta_2)/e$, marking the onset of the so-called *quasiparticle branch*. As previously alluded to, thermal broadening of this transition provides an indication of the effective electronic temperature of the junction. Experimentally, therefore, an IV with a quasiparticle branch of significant rounding is judged to be

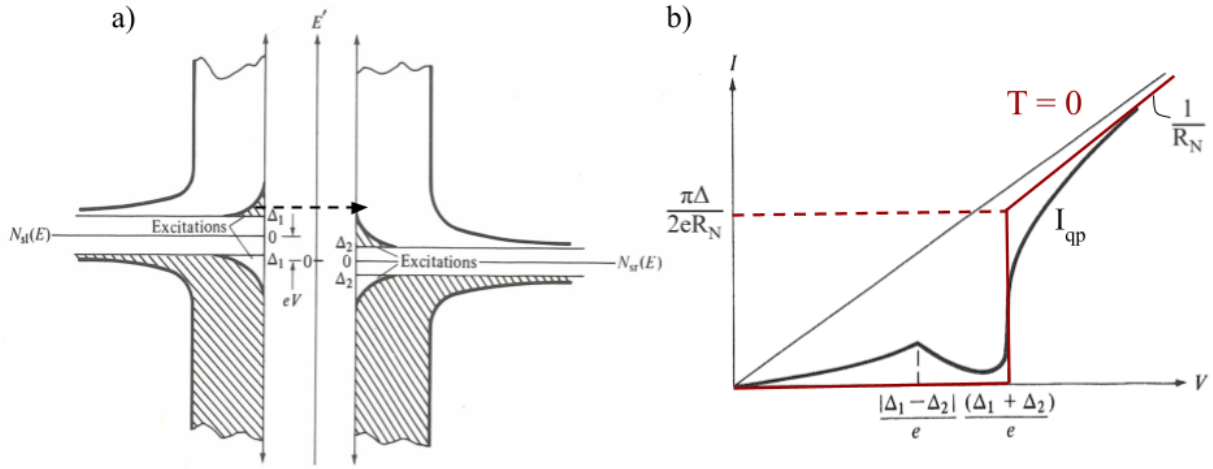

Figure 2.1: **Quasiparticle tunneling in a SIS junction at finite temperature.** (a) Semiconductor model description of quasiparticle tunneling. Superconducting DOS of the right ($N_{sr}(E)$) and left ($N_{sl}(E)$) electrodes plotted horizontally vs excitation energy. Applying V across the junction shifts the Fermi energies with respect to one another. Filled (unfilled) regions represent electron- (hole-) like quasiparticle states. Dotted arrow depicts tunneling of thermally excited quasiparticles. (b) IV curve depicting I_{qp} between two superconductors at finite (black) and zero (red) temperature. For all junctions studied in this thesis, $\Delta_1 = \Delta_2 = \Delta$. Figures adapted from Ref. [11].

at a higher effective temperature. The sharper the transition, the colder the electronic temperature.

The low-temperature IV allows one to determine with great accuracy the value of Δ from the abrupt onset of the quasiparticle branch and R_N from linear slope at high bias. These values may be plugged into Eq. (2.6) to calculate E_J without the need to make assumptions about the gap or tunneling resistance (which may be temperature-dependent).

2.3 RCSJ model — the semiclassical picture

To model both the quasiparticle *and* supercurrent contributions to the voltage response of a current-biased SIS JJ, the Resistively and Capacitively Shunted Junction (RCSJ) model has proven remarkably enduring. The model was introduced separately by Stewart [12] and McCumber [13] in 1968 as a purely classical description. An equivalent circuit representation illustrates that the time-evolution of the Josephson phase ϕ is mechanically similar to the motion of a damped driven pendulum.

Current across the JJ is separated into three distinct parallel channels. A two-fluid treatment distinguishes I_{qp} from I_s, and, given the parallel-plate capacitance of the device, a displacement current across the superconducting electrodes is also included. By equating the total bias current I to these three distinct current paths, the circuit is modeled

$$C\left(\frac{dV}{dt}\right) + \frac{V}{R} + I_c \sin(\phi) = I \tag{2.9}$$

with the first term describing the capacitive contribution, the second term associated with the "phenomenological conductance" [13] and the third term representing the phase-dependent supercurrent across the junction from Eq. (2.2). The externally supplied bias current I represents the driving force in this model. See Fig. 2.2 for a schematic of the RCSJ circuit.

It should be noted that a fourth term exists within the RCSJ model which describes phase-dependent dissipation related to the interference between super- and quasiparticle currents [1], [17]. However, for the small junctions concerning this thesis, the effects of this dissipation term are thought to be extremely subtle in IV measurements [8]. Therefore, we exclude it from further discussion.

One may clarify the analogy to a damped oscillator by rewriting Eq. (2.9) in terms of ϕ and its

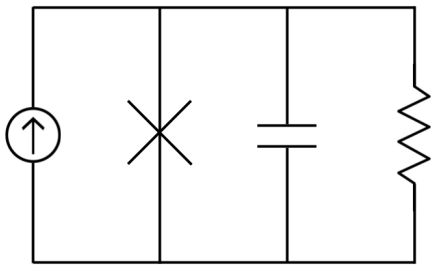

Figure 2.2: **RCSJ equivalent circuit model.** Supercurrent element symbolized by "X." Shunt resistance R incorporates frequency-dependent contributions from the driving electronics and measurement environment [14]–[16]. Resulting equation of motion for ϕ is identical to a particle of mass $m \propto C$ in a washboard potential tilted by I. Dissipation inversely proportional to R.

time derivatives as

$$\left(\frac{\hbar}{2e}\right)^2 C\,\frac{d^2\phi}{dt^2} + \left(\frac{\hbar}{2e}\right)^2 \frac{1}{R}\frac{d\phi}{dt} + \left(\frac{\hbar}{2e}\right) I_c \sin(\phi) = \left(\frac{\hbar}{2e}\right) I \tag{2.10}$$

This equation describes a phase "particle" with "mass" $m \propto C$ at "position" ϕ moving along a sinusoidal potential subject to a viscous drag coefficient $\propto 1/R$. A complete list of the mechanical analogs to the RCSJ model is shown in Table 2.1.

We may use the RCSJ potential $U(\phi)$ to qualitatively describe the IV fingerprint of a Josephson junction. Applying bias current across the junction tilts the 2π-periodic washboard potential. Initially, at zero bias, the particle is trapped in a local minimum. It oscillates at the angular frequency ω_0 but its average motion is zero and, by Eq. (2.3), no voltage is measured across the junction. We refer to this small bias regime in the IV curve as the *supercurrent branch*. Increasing the bias current tilts the potential as shown in Fig. 2.3(a). At a particular current $I = I_c$, the curvature of the potential becomes a monotonically decreasing slope, affecting the particle in such a way that it cannot be re-trapped and a terminal velocity is soon reached. The particle is said to have entered

mass	m	$(\hbar/2e)^2\,C$
drag coefficient	$m\gamma$	$(\hbar/2e)^2\,(1/R)$
potential	$U(\phi)$	$-(\hbar/2e)(I_c\cos(\phi)-I\phi)$
angular oscillator frequency	ω_0	$(2e/\hbar)^{1/2}(I_c/C)^{1/2}$
quality factor	Q	$\omega_0 RC$

Table 2.1: **Mechanical analogs to RCSJ circuit components**

a *running state* corresponding to a finite voltage. Here marks the onset of the quasiparticle branch of the IV curve. Further increasing the bias current completely destroys superconductivity leaving only quasiparticle tunneling and a linear slope corresponding to R_N.

Upon returning the bias current back to zero, the potential slowly regains its sinusoidal form. In the underdamped ($Q \gg 1$) junctions concerning this thesis, inertia will continue to carry the particle down the washboard until the energy lost in one 2π period re-traps the particle in a well at a "retrapping" current $I_r < I_c$. Here, the IV switches back to the supercurrent branch. Therefore, for underdamped junctions, the IV curve will be hysteretic. See Fig. 2.3(b).

What we have just described is an idealized situation ignoring the effect of thermal noise on both quasiparticle excitations and the phase particle itself. As we shall see, for small junctions with small intrinsic capacitances, the IV curve reveals distinct *variations* on the one illustrated in Fig. 2.3(b). The reason for this is broadly due to the uncertainty relation between charge number N and phase difference ϕ. With precise limitations on N, the subsequent large uncertainty in ϕ causes quantum fluctuations even as $T \to 0$. We discuss two important manifestations of these phase fluctuations in the IV curves of small Josephson junctions of typical size in today's superconducting qubits [3].

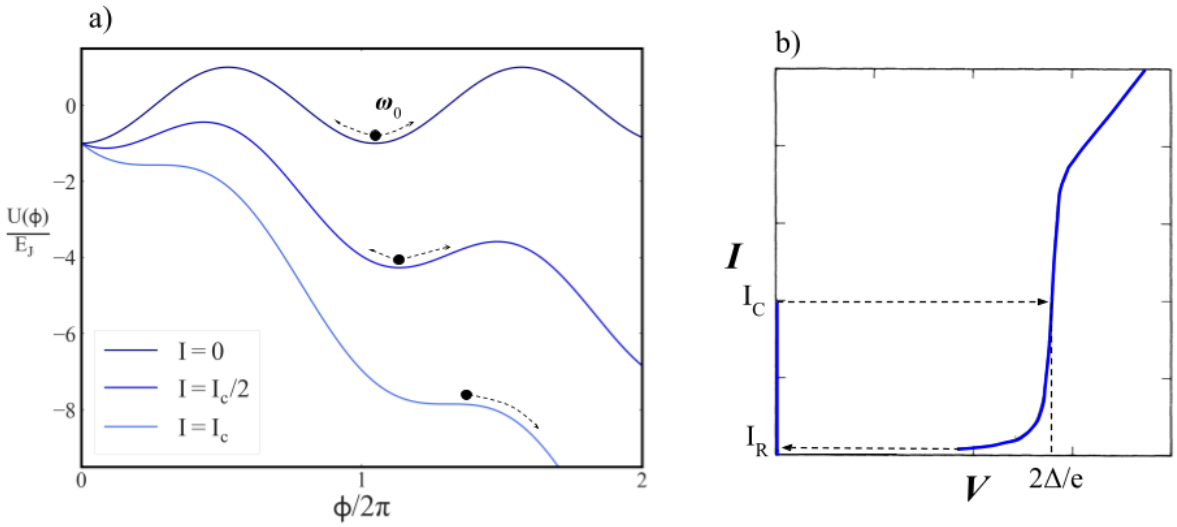

Figure 2.3: **RCSJ washboard potential and classical voltage response.** (a) Dynamics of the fictitious phase particle in a "tilted washboard" potential. Barrier height determined by E_J. Particle sloshes about local minimum at an angular frequency ω_0. Applying current I tilts the potential. Running state corresponding to finite voltage $V = 2\Delta/e$ at $I \geq I_c$. (b) Hysteretic IV response in lightly damped junction ($Q \gg 1$). Horizontal dotted lines show direction of current sweep.

2.3.1 Phase diffusion

Qualitatively speaking, if the phase particle is activated out of a local minimum but *lacks* the energy to continue into a running state, it will instead diffuse well-to-well in a random-walk-like fashion. Consequently, a low voltage corresponding to the average motion is measured in the supercurrent branch of the IV curve. This so-called *phase diffusion* process associated with measured resistance R_0 is exclusive to small junctions [8] and critical to our understanding of phase fluctuations at small bias.

Phase diffusion was originally thought impossible in underdamped junctions. The idea was that

after the particle escaped from a well, it would immediately enter the running state. The particle would never come to rest in a neighboring well because not enough energy would be lost in the system during one 2π slip. Therefore, the simultaneous presence of hysteresis and a low-voltage state near zero bias in an IV curve could not be explained by the traditional RCSJ model. To remedy this, Kautz and Martinis [14], [18] included a frequency-dependent damping component. In their adapted model, isolation resistors and lead capacitances of the external circuit play an essential role in damping *only* at high frequencies close to ω_0. Since ω_0 represents the escape attempt frequency when the particle is trapped, high damping in this regime allowed for slow diffusion of the phase particle at shallow tilt. Light damping in the high-voltage running state remained largely affected in this revised RCSJ model [14].

Here we see the first indication of how *environmental impedance* affects the phase dynamics of small junctions. The environment is a very important consideration not only in the context of measuring sensitive qubit states, but also in our analysis of IV curves. We consider the influence of environmental impedance in greater depth in the next section.

Kautz and Martinis analyzed small junctions at elevated temperatures where over-the-barrier excitations were the dominate cause of phase diffusion. Thermal activation is not the only process by which the particle may diffuse, however. At sufficiently low temperatures, quantum fluctuations of the phase particle *through* the barrier may become the dominant source of diffusion. This mode of dissipative quantum tunneling, theoretically proposed by Caldeira and Leggett [19] and Ivanchenko and Zil'berman [20], was reported in the work of Iansiti *et al.* [21]–[23] who measured small junctions at low temperatures in the regime $E_T \ll E_J$. Here, the authors proposed a simple model through which quantum tunneling formalism may be used to predict the measured phase diffusion resistance R_0. Assuming the particle tunnels only through one barrier at a time, accumulating 2π on each tunneling event, and that the tunneling rate Γ^+ to the right (downhill) is

independent from the tunneling rate Γ^- to the left (uphill), the phase diffusion resistance

$$R_0 \equiv \frac{V}{I} = \frac{1}{I}\frac{\hbar}{2e}\frac{d\phi}{dt} \approx \frac{1}{I}\frac{\hbar}{2e}2\pi(\Gamma^+ - \Gamma^-) \tag{2.11}$$

is obtained using Eq. (2.3) [22]. An average voltage is measured because the tilt of the washboard downhill makes the escape from a potential minimum more probable in one direction than the other. An equation for Γ is found using the Wentzel-Kramers-Brillouin (WKB) approximation [24] first used in this context by Ref. [19]. We have

$$\Gamma = \frac{\omega_0}{2\pi}\chi\sqrt{\Delta U/\hbar\omega_0}\exp\left(-s\Delta U/\hbar\omega_0\right) \tag{2.12}$$

where χ and s are numerical prefactors associated with the exact shape of the potential and damping magnitude. Note the temperature-*independence* which categorizes the diffusion process as a purely quantum phenomenon.

In the small-junction experiments of Iansiti *et al.*, the measured R_0 agreed with the theoretical value within the same order of magnitude [23]. For junctions with $E_J \approx E_C$, R_0 was found to be ~ 1 kΩ and increased for smaller ratios of E_J/E_C. The diffusion rate appeared to have an super-exponential dependence on the intrinsic capacitance of the phase particle which, classically speaking, follows from our prior argument. Light particles trapped by potential barriers of lower height, i.e., junctions with small E_J and large E_C, are highly susceptible to voltage-inducing thermal excitations or quantum fluctuations. Viewed in this context, it follows that shunting the junction with a large capacitor to lower E_C would reduce phase fluctuations and lead to better overall coherence times. Indeed, this idea was introduced as a "transmon" qubit in 2007 by Koch *et al.* who predicted longer qubit dephasing times compared to unshunted charge qubits [25]. Today, as the platform of choice for Google [26], IBM [27] and Rigetti Computing [28], the transmon is by

far the most popular superconducting qubit configuration implemented at scale.

Transmons are not typically current-biased during operation, and the dc impedance from the junction to the room temperature microwave readout electronics is theoretically infinite. Nonetheless, low-frequency stray fields around the qubit chip may cause superconducting screening currents that dissipate according to R_0 in JJs without dc leads attached.

2.3.2 Switching current

In practice, one never observes the (low-voltage) supercurrent branch up to $I = I_c$ in small junctions. The measured switching current out of the supercurrent branch is *always* $I_{\text{sw}} < I_c$. As the current bias is ramped, stochastic escape processes trigger a running state *before* the washboard is fully tilted. The result is a transition to the finite voltage state at a particular current value an order of magnitude less than I_c for $E_J \sim E_C$.

Data on suppressed I_{sw} below the expected value of I_c was recently cataloged by Lu *et al.* [29] for a variety of junctions with small E_J ($< 100\,\mu$eV). The authors found a *systematic* reduction in measured switching currents at $T < 50$ mK diverging from Eq. (2.5). The discrepancy grew as the E_J of the junctions decreased. Since E_J represents the height of the potential barrier, the strong dependence of I_{sw} on E_J was attributed to a greater likelihood of over-the-barrier thermal activation [29].

An explanation for this trend may be found in early theoretical work incorporating a stochastic emf term into Eq. (2.10) [20]. The resulting delta-correlated Johnson current noise I_n arising from thermal fluctuations in the external circuitry added another parallel component to the RCSJ circuit. The theory predicted a *quadratic* drop in the maximum supercurrent with decreasing barrier height — a good match to the trend seen in the literature [29]. To first order, therefore, reduced switching current $I_{\text{sw}} < I_c$ may be explained in the context of environmental noise impacting the junction.

Since particle escape is stochastic, one must measure the switching process many times to say something definitive about the *mode* of escape, classical or quantum-mechanical. The size and shape of switching current distributions (SCD) were scrutinized in experiments probing the quantized nature of the Josephson potential [5] and phase tunneling phenomena [4]. Despite the Nobel notoriety of these experiments, interpretations of the SCD measured therein continue to be a matter of debate [30].

To briefly summarize, the dc IV curve of small JJs reveal features that are not observed in larger junctions: reduced $I_{\rm sw}$ below the expected I_c calculated from the Ambegaokar-Baratoff relation and a resistance R_0 associated with diffusion of the phase particle in the small bias (shallow-tilt) regime. Both of these phenomena are due to the increased sensitivity to noise associated with the small capacitance of the junction. It is therefore fitting to develop a model by which environmental circuit noise may influence quantum and classical fluctuations of the phase particle.

2.4 Effects of the environmental impedance

When lithographic technology enabled the fabrication of small junctions in the 1980s, it was not at all common to observe phase diffusion *and* hysteresis in the same device. For bias currents $I_r < I < I_c$, there needed to exist two stable voltage states, one in the supercurrent branch, the other in the quasiparticle branch. Since the diffusion process requires high damping at the attempt frequency ω_0, and the running state requires low damping at low frequency, Kautz and Martinis [14], [18] investigated *frequency-dependent* damping effects from the environment.

In typical transport measurements, junctions are attached to leads with transmission-line impedance $Z_0 \approx 377\ \Omega$, the impedance of free space, meaning there is a strong electrical connection to the bias circuitry. In this case, the external shunting resistance of the current source, the internal tunneling resistance, and the parasitic capacitance of the leads to ground determine the cut-off frequencies

in the circuit. In an attempt to electrically isolate the junction from the environment in order to study its effects, Kautz and Martinis externally loaded the JJs with small on-chip NiCr wires with resistances $R_{\text{leads}} > 100$ kΩ. It was assumed that due to the high quasiparticle resistance of the junctions, damping at microwave frequencies would be determined by the external loading [31]. The authors used a Monte Carlo method to simulate the strong damping at microwave frequencies resulting from the resistor-embedded circuit. The measured phase diffusion R_0 agreed well with the simulations for their hysteretic junctions [14], [18].

It should be noted that this choice of lead resistance well exceeded the quantum resistance $R_Q = h/4e^2$. The particular value of R_{leads} is important in the context of Coulomb blockade experiments in small junctions [32]. In order to observe charging effects in these small junctions, E_C must exceed the quantum uncertainty $\Delta E > \hbar/\Delta t \approx \hbar/RC$ associated with the finite lifetime of the small capacitor charge. Upon equating E_C with ΔE, we find that $R > 2\hbar/e^2 \approx R_Q$ [8]. In experiments on small junctions coupled to tunable lead resistances, a blockade effect in the quasiparticle IV curve was observed *only* when $R_{\text{leads}} > R_Q$ [33], [34]. We return to the topic of environmental effects on the measured quasiparticle branch in Chapter 4.

Kautz and Martinis studied classical over-the-barrier phase diffusion in their environmental damping analysis. This assumption becomes somewhat less relevant in qubits where $E_T \ll E_J$ and the phase particle has an increased probability of tunneling rather than thermally activating. To capture both the frequency dependence of the system and the dissipative quantum tunneling processes thought to dominate at low temperature, we use the generalized quantum Langevin equation adapted for this context by Ford *et al.* [35] and Hu and O'Connell [15].

2.4.1 The quantum Langevin approach

The Langevin equation describes how a system evolves when subject to deterministic and random forces. For our purposes, we would like to adapt the RCSJ equation of motion Eq. (2.10), into an equation that includes noise contributions from the environment.

Initially, without including random noise forces, a particle of mass m subject to a potential U and dissipation parameter γ may be described by

$$m\frac{d^2x}{dt^2} + m\gamma\frac{dx}{dt} + U'(x) = 0 \tag{2.13}$$

where x represents the particle position. By inspection, one may simply compare Eq. (2.10) to Eq. (2.13) to write down the equivalent circuit components of the RCSJ model in terms of the prefactors in this equations (see Table 2.1).

In a real measurement where noise cannot be ignored, the dynamics of the phase resemble the fluctuating motion of a small particle in a fluid, classically referred to as Brownian motion [36]. In addition to the deterministic driving force contained in I, there is also a random force associated with current noise I_n introduced by the shunt resistor R and the measurement electronics. One way to model the stochastic motion of the phase particle is with the quantum Langevin equation [35]

$$m\frac{d^2\phi}{dt^2} + \int_0^\infty \mu(t-t')\phi(t')dt' + \frac{\partial U}{\partial \phi} = F(t) \tag{2.14}$$

describing a particle of mass $m = (\hbar/2e)^2C$ in a potential $U(\phi)$. In this treatment, noise is related to the autocorrelation of the random force $F(t)$ through the Fourier transform of the memory function $\mu(t) \rightarrow \tilde{\mu}(\omega)$ by

$$\frac{1}{2}\langle F(t)F(t') + F(t')F(t)\rangle = \frac{1}{\pi}\int_0^\infty d\omega\ \Re[\tilde{\mu}(\omega)]\hbar\omega\coth\left(\hbar\omega/2k_bT\right)\cos\left(\omega(t-t')\right) \tag{2.15}$$

Intuitively, the motion of a particle with small m ought to be more affected by random forces compared to more massive particles. As such, we expect small-capacitance junctions to be more susceptible to noise. Analytically, this may be seen by Fourier transforming Eq. (2.14) and solving for the poles of the response function

$$\alpha(\omega) = (-m\omega^2 + i\omega\tilde{\mu}(\omega) + m\omega_o^2)^{-1} \tag{2.16}$$

taken from $\tilde{\phi}(\omega) = \alpha(\omega)\tilde{F}(\omega)$ where the transform gives $\phi(t) \rightarrow \tilde{\phi}(\omega)$ and $F(t) \rightarrow \tilde{F}(\omega)$. The frequency-dependent memory function $\tilde{\mu}(\omega)$ appearing in Eq. (2.15) and Eq. (2.16) reduces to $m\gamma$, the drag coefficient in the RCSJ model, in the case of ohmic dissipation relevant to our situation [15]. In principle, however, $\tilde{\mu}(\omega)$ may contain information that depends on the past history of the system or on a more complicated environment impedance [37].

For now, we will now take a simple limiting case of the model relevant for superconducting qubits. If we ignore the dissipative resistive term by letting γ, $\tilde{\mu}(\omega) \rightarrow 0$ and consider only the case of an un-driven junction ($I = 0$) then Eq. (2.10) simplifies to

$$\left(\frac{\hbar}{2e}\right)^2 C\frac{d^2\phi}{dt^2} + \left(\frac{\hbar}{2e}\right) I_c\sin(\phi) = 0 \tag{2.17}$$

and the pole of $\alpha(\omega)$ yields $\omega = \omega_0$, the excitation energies of the system. Expanding the potential minimum about $\phi = 0$ and including only terms linear in ϕ in Eq. (2.17), we write

$$m\frac{d^2\phi}{dt^2} + m\omega_0^2\frac{d\phi}{dt} = 0 \tag{2.18}$$

where m and w_o are described in Table 2.1. Classically, w_0 represents the frequency at which the fictitious phase particle sloshes about the bottom of the well. In the context of qubits, $\hbar\omega_0$ represents the energy spacing between the ground state and first excited state of the harmonic oscillator potential.

If we consider the effect of some dissipative finite $\tilde{\mu}(\omega)$ on the qubit dynamics, the fundamental frequency ω_0 acquires a finite lifetime whose time constant depends on the specific form of $\tilde{\mu}(\omega)$. Joyez *et al.* [16] showed that, using Norton's theorem, the total environment admittance from filtering, bias and readout circuitry may be reduced to $Y(\omega) = (2e/\hbar)^2\tilde{\mu}(\omega)$ connected in parallel with the junction. In the case of an idealized transmon qubit concerning this thesis, there are no measurement leads directly attached to the sample and a large capacitor $C_s \gg C$ shunts the JJ. Subsequently, $Y(\omega) = i\omega C_s$ and the new excitation energies become $\omega_{\text{transmon}} = (2e/\hbar)^{1/2}(I_c/(C + C_s))^{1/2}$ after reevaluating the poles in Eq. (2.16) [38]. This is the result one expects using the qubit Hamiltonian approach to model a small junction shunted by a large capacitor [25].

In summary, we emphasize that the RCSJ model on which we base our analysis is a largely classical description of the macroscopic characteristics of the junction. Its power lies in the ability to map key junction parameters (I_c, C, R) to the physics captured in an IV curve. The model lacks any detail about the microscopic quantum behavior of the charge carriers within the device. In our discussion of superconductor-normal metal-superconductor (SNS) junctions in the next chapter, we adopt a microscopic approach in lieu of the phenomenological one.

CHAPTER 3
THEORY: SNS JUNCTION

The term "weak link" describes *any* kind of barrier between two coupled superconductors. In a normal metal weak link, the Josephson effect is dictated by the superconducting *proximity effect*, a phenomenon in which the superconductor imparts its characteristics into the normal metal. Unlike in SIS junctions, supercurrent in SNS junctions is carried by conducting quasiparticles which retain coherent properties over long distances in a clean metal. While the barriers of SIS junctions are measured in Angstroms, the length of SNS junctions are measured in microns.

This fact allows experimentalists to probe *inside* the Josephson junction by attaching additional leads directly to the weak link. These leads themselves may be superconducting, transforming a single Josephson junction into a *multiterminal* Josephson junction (MTJJ) defined here as three or more superconductors coupled to continuous normal metal film. In this case, the phase of every superconducting terminal contributes to the dissipationless current and quasiparticle DOS within the device. MTJJs are a test bed for probing fundamental mesoscopic superconductivity with potential applications in superconducting circuits.

This chapter contains the relevant theory for SNS JJs made of *diffusive* normal metal where the elastic mean free path of normal electrons l is much shorter than the length of the junction L. The quasiclassical Green's function technique commonly used to calculate measurable quantities in diffusive proximity-coupled systems is described in some detail. We end this chapter with an account of previous experimental work in the field of MTJJs.

3.1 Superconducting proximity effect

When a normal metal (N) is in good electrical contact with a superconductor (S), it acquires superconducting properties. More tangibly, this means that the normal metal develops (a) an ability to sustain dissipationless supercurrent and (b) an energy *gap* in the quasiparticle DOS. This former point enables the Josephson effect in proximity-coupled normal metal devices.

In addition to the superconducting gap Δ, an important energy scale in the proximity effect is the so-called *Thouless energy*

$$E_{\text{Th}} = \frac{\hbar D}{L^2} \tag{3.1}$$

Sometimes referred to as the "correlation" energy, E_{Th} characterizes the time $\tau = L^2/D$ it takes for a single particle to traverse a sample of length L [39]. Since the generic quantum phase $e^{iEt/\hbar}$ determines the dephasing time for a particle with energy E, E_{Th} may be viewed as the maximum energy difference between two in-phase particles over a distance L. The diffusion coefficient D depends on the amount of disorder in the metal. It will appear again in our discussion of quasiclassical theory.

A natural mesoscopic length falls out of the Thouless energy when set equal to the thermal energy $E_T = k_b T$. The resulting *Thouless length*

$$L_{\text{Th}} = \sqrt{\frac{\hbar D}{k_b T}} \tag{3.2}$$

establishes a length scale for which the proximity-induced superconducting correlations extend into the normal metal [40]. At finite temperatures, the proximity effect is strongest in the region enclosed by L_{Th} near the superconductor. Therefore, for a normal metal wire of length L bounded

on either side by a superconductor, $L_{\text{Th}} > L$ in order for the SNS structure to be fully Josephson coupled. For a sense of scale, with $D \approx 200$ cm^2/s, $L_{\text{Th}} \approx 1.2$ μm at $T = 100$ mK and a SNS junction over a micron long may support supercurrent.

As we will see, superconducting correlations leaking into the normal metal cause an energy gap to open in the quasiparticle DOS. The size of this "minigap" $\delta < \Delta$ is on the order of E_{Th}. Why the diffusion time of a single quasiparticle should set the energy scale at which no available quasiparticle states may be found in the normal metal is a result of the microscopic processes at the NS interfaces [41]. Such *Andreev reflections* are thus central to the proximity effect since they provide the elementary mechanism for converting single electron states into supercurrent-carrying electron correlations in the superconducting condensate. The interplay of long-range coherence in the normal metal and Andreev processes at the NS interfaces makes the Josephson effect possible in diffusive SNS junctions.

At this point we introduce the single electron phase coherence length L_ϕ from the theory of weak localization in disordered metals [42]. L_ϕ sets the length scale for electron interference and represents the ultimate cutoff for the proximity-induced superconducting correlations. The length of the normal metal wire must be less than L_ϕ in order to observe the full Josephson effect. We discuss L_ϕ in greater depth in Chapter 4.

3.1.1 Andreev reflection

Due to the energy gap Δ in the DOS around the Fermi energy of a superconductor, the transfer of a single quasiparticle with energy $E < \Delta$ into the superconductor is forbidden. In the early tunneling experiments by Giaever [43], it was found that the size of Δ could be measured from the IV curve of a low-transparency NS junction. Normal metal electrons impinging on the superconductor cannot enter the condensate due to a lack of available states. A finite current appears across the

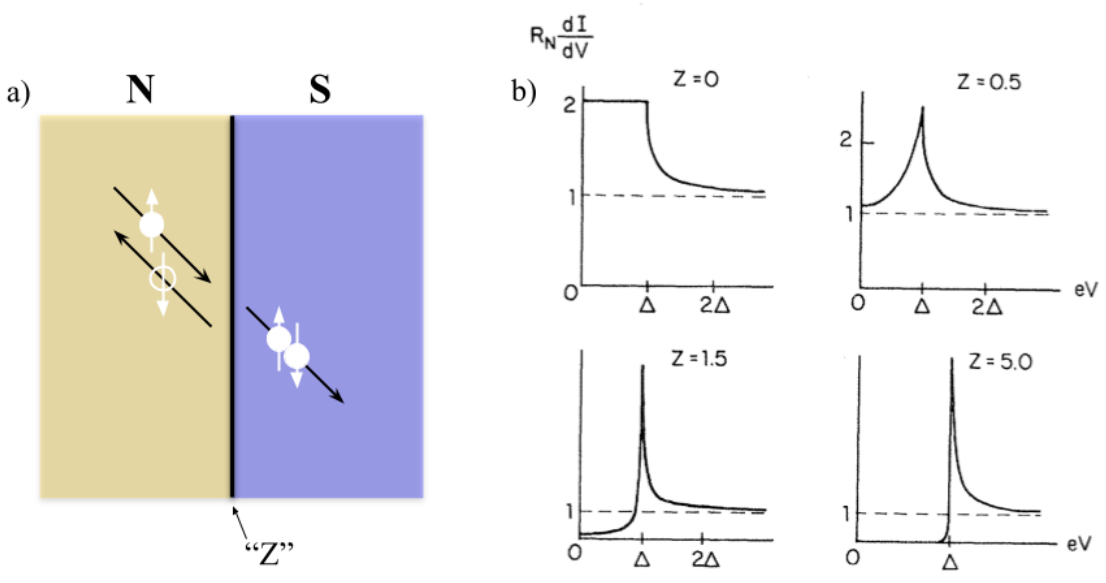

Figure 3.1: **Andreev reflection for arbitrary interface transparency.** (a) Andreev reflection at an NS interface. Black arrows denote velocity, white arrows the spin. Electron (hole) represented with full (empty) circle. The barrier strength Z determines the probability of Andreev reflection relative to ordinary reflection. (b) Normalized IV curves at $T = 0$ of NS junctions as a function of barrier strength Z. $Z = 0$ corresponds to perfect transparency. High Z corresponds to poor transparency. At high voltages, all junction resistances tend towards R_N. Figure from Ref [44].

junction only when electrons are driven with energy $eV \gtrsim \Delta$.

For highly transparent NS interfaces for which we say the superconductor has "good" electrical contact with the normal metal, another type of charge-transfer process is allowed. This process, Andreev reflection [45], depicted in Fig. 3.1(a), describes how a single normal electron incident on a clean NS interface is converted into a correlated *Cooper pair*, the charge carrier in the superconducting condensate. An incoming electron with energy $E < \Delta$ combines with a hole of opposite spin and velocity to generate a $2e$ charge in the superconductor. For electrons incident at the Fermi energy, the hole is perfectly retro-reflected and phase-shifted by $\pi/2 + \phi$ where ϕ is the

usual phase of the order parameter in the superconductor [41]. Because every electron charge e creates a $2e$ Cooper pair in the superconductor, the subgap conductance of an ideal NS interface is twice the normal state conductance.

In real experiments involving separately deposited metals, NS interfaces are rarely ideal. A small amount of oxide may form at the boundary, for example, affecting the various outcomes of electrons incident on the interface. In the case of a finite barrier, the probability of *ordinary* electron reflection may be greater than the probability of Andreev reflection. Blonder, Tinkham, and Klapwijk (BTK) [44] worked out various types of transmission and reflection probabilities for normal electrons at NS interfaces of arbitrary transparency. The resulting BTK theory characterizes the interface transparency $t = 1/(1 + Z^2)$ by a barrier strength parameter Z between N and S. Mathematically, Z represents a kind of $\delta-$function potential where $Z = 0$ is associated with no barrier and $Z > 1$ is a strong barrier. Figure 3.1(b) shows how the IV curve of a NS junction depends on the value of Z. Conductance doubling is observed at high transparency and Giaever tunneling IV is recovered at low-transparency.

One of the most important properties of Andreev reflection, and indeed of the proximity effect as a whole, is the fact that Andreev quasiparticles carry information about the *phase* of the superconductor from which they reflect. If the superconducting order parameter is fixed at $|\Delta|e^{i\phi}$, for example, an incident quasiparticle with energy E acquires a phase shift $\delta\phi = \phi + \arccos(E/\Delta)$ after reflecting from the NS interface. The second term is due to the partial penetration of the quasiparticle wave function into the condensate. For energies $E \ll \Delta$ at zero temperature, quasiparticle phase interference may result in high contact resistance of low-transparency NS barrier [46].

In the case of a normal metal sandwiched between *two* superconductors, the dc Josephson effect may be understood from the time-reversed Andreev process: a retro-reflected hole is converted

back into an electron at the other interface, leading to a transfer of a Cooper pair from one superconductor to another. Since interference between Andreev quasiparticles depends on the phases ϕ_1 and ϕ_2 of the superconducting terminals, supercurrent depends on the phase difference ϕ across the junction, resulting in a current-phase relation. Although CPRs of SNS junctions are phase-periodic similar to SIS junctions, we shall see that they may be non-sinusoidal depending on geometry and current distributions inside the normal metal [47].

If l of an electron inside the normal metal is much greater than the length of the junction, as in the case of a *ballistic* SNS junction, then interference of the time-reversed quasiparticles result in discrete bound states inside the normal metal. Such Andreev bound states (ABS) are responsible for the subgap conductance in *clean* SNS junctions. The trajectory of electrons in *diffusive* metal, however, are not well-defined and ABSs are no longer the natural concept to refer to charge transport in SNS junctions. Instead, the energy spectrum of correlations inside the normal metal is characterized by the quasiparticle DOS calculated directly using the quasiclassical Green's function theory of superconductivity, the subject of the next section.

3.2 Quasiclassical techniques

The starting point for mesoscopic problems in superconductivity is the Green's function in Nambu representation, which combines particles and holes into a single subspace [48]. We may express the time-ordered Green's function with position and time coordinates $(\mathbf{r}_i, t_i)$ as

$$G_{\uparrow\downarrow}(\mathbf{r}_1, t_1; \mathbf{r}_2, t_2) = \frac{-i}{\hbar}\langle \hat{T}\hat{\Psi}_{\uparrow}(\mathbf{r}_1, t_1)\hat{\Psi}^{\dagger}_{\downarrow}(\mathbf{r}_2, t_2)\rangle \tag{3.3}$$

using the pseudo-spinor compact notation $\hat{\Psi}^{\dagger} = (\Psi^{\dagger}_{\uparrow}, \Psi_{\downarrow})$ for fermionic field operators [49]. Here, $\hat{T}$ is the time-ordering operator included for causality, effectively reversing the order of operators

for negative time. The brackets refer to a weighted expectation value. Viewed this way, the Green's function is a correlation function relating the destruction of a particle at $(\mathbf{r}_1, t_1)$ to its creation at $(\mathbf{r}_2, t_2)$. In the equations to follow, $\hbar = 1$ and the "†" represents the Hermitian conjugate.

The many-body Green's function approach to superconductivity allows one to study mesoscopic superconducting devices in non-equilibrium situations at temperatures much less than the critical temperature T_c of the superconductor. This contrasts to the phenomenological order parameter theory of Ginzburg and Landau, which is most accurate at temperatures near T_c [8]. Since we are concerned with long-range phase coherent phenomena measured at low temperatures, the many-body Green's function approach is better suited to handle numerical simulations of long SNS junctions. In the following section, we will provide the relevant background quasiclassical theory and outline an approach for numerically solving measurable quantities in arbitrary geometries of 1D normal wires coupled to normal and superconducting reservoirs.

The Green's function Eq. (3.3) oscillates rapidly with an amplitude inverse to the Fermi wavevector k_F as a function of the spatial difference $\mathbf{r}_2 - \mathbf{r}_1$. The length $1/k_F$ is much shorter than the superconducting coherence length ξ_s which, for our purposes, represents the average distance between correlated pairs in the superconductor. Therefore, we may simplify our equations by transforming to the center-of-mass coordinates $(\mathbf{R}, T)$ of the two-particle correlation [40], and we may ignore information contained in the fast oscillations of the full Green's function by considering only the excitations near the Fermi energy. The idea is to average over particle energy associated with the magnitude of momentum p_F in anticipation of the sharply-peaked nature of the Fourier transform of oscillations at $|\mathbf{p}| = p_F$. We preserve the dependence of the direction of momentum through the direction of the Fermi velocity $\mathbf{v}_F$. The quasiclassical Green's function is then [49]

$$g(\mathbf{R}, \mathbf{v}_F, E) \equiv \frac{i}{\pi} \int d\epsilon_p \, G(\epsilon_p, \mathbf{v}_F, \mathbf{R}, E) \tag{3.4}$$

where the integral is taken over $\epsilon_p = p_F^2/2m - \mu$ with particle mass m and chemical potential μ. Applying this approximation to the gradient expansion of the Gor'kov equation of motion gives the Eilenberger equation [50]

$$-[\mathbf{v}_F \partial_{\mathbf{R}}, g(\mathbf{R}, \mathbf{v}_F, E)] = [-iE\tau^3 + \tilde{\Delta} + \frac{1}{2\tau}\langle g(\mathbf{R}, \mathbf{v}_F, E)\rangle_{\mathbf{v}_F}, g(\mathbf{R}, \mathbf{v}_F, E)] \tag{3.5}$$

where the expectation value is the angular average at the Fermi surface,

$$\tau^3 = \begin{pmatrix} 1 & 0 \\ 0 & 1 \end{pmatrix} \tag{3.6}$$

is the usual Pauli spin matrix, and

$$\tilde{\Delta} = \begin{pmatrix} 0 & \Delta \\ -\Delta^* & 0 \end{pmatrix} \tag{3.7}$$

represents the pair amplitudes in the normal metal. In the Eilenberger equation, τ is the elastic scattering time inversely proportional to the impurity self energy. Equation (3.5) is a generalized equation of motion for the superconducting Green's function described with arbitrary disorder. Notice that evaluating the Eilenberger equation does not involve integration, only matrix multiplication, and numerical techniques often utilize convenient parameterizations to facilitate the convergence of solutions.

3.2.1 The Keldysh-Usadel equation

We are concerned with the "dirty limit" where the self energy $1/\tau$ term dominates Eq. (3.5) and the motion of quasiparticles is diffusive. In this case, the strong impurity scattering has the effect of randomizing the momentum of the quasiparticles such that the Green's functions are independent

of the direction of **p**. We may therefore expand the quasiclassical Green's function to first order in momentum as

$$\hat{g}(\mathbf{R}, \mathbf{v}_F, E) \approx \hat{g}_s(\mathbf{R}, E) + \hat{p}\,\hat{g}_p(\mathbf{R}, E) \tag{3.8}$$

which, in the limit $1/\tau \gg E, \Delta$ gives the Usadel equation [51]

$$[\tau^3 E + \tilde{\Delta}, \tilde{g}_s] = iD\partial_{\mathbf{R}}(\tilde{g}_s \partial_{\mathbf{R}} \tilde{g}_s) \tag{3.9}$$

with diffusion coefficient $D = v_F^2 \tau$. This equation is the starting point for many calculations on disordered mesoscopic superconducting systems. The remainder of this chapter will outline methods in which the Usadel equation may be used to solve for the quasiparticles DOS in proximity-coupled normal metal, specifically in SNS JJs.

To this end, we require a theoretical description of the quantum analog of the classical Boltzmann transport equations. This comes from the Keldysh Green's function technique which allows us to describe the real-time evolution of a many-body system outside of equilibrium [52]. In the Keldysh approach, the time evolution of the system is described by a forward and backward propagator. Keldysh showed that these propagators may be combined along a single contour in the complex time plane to account for thermal averaging at finite temperature. The Green's functions are defined on this Keldysh contour, and, depending on which side of the contour the time arguments reside, they reduce to different analytic components. In this Keldysh space (after dropping the "s" subscript for clarity) we obtain the Green's function

$$\hat{g} = \begin{pmatrix} \tilde{g}^R & \tilde{g}^K \\ 0 & \tilde{g}^A \end{pmatrix} \tag{3.10}$$

where the "$\sim$" denotes matrices in Nambu-Gor'kov space such that each element is itself a 2×2 matrix. The resulting Keldysh matrices are 4×4 supermatrices symbolized by the "$\wedge$".

The retarded $\tilde{g}^R$ and advanced $\tilde{g}^A$ Green's functions determine the energy-dependent or *spectral* properties of the system and are related to the Keldysh Green's function $\tilde{g}^K$ through

$$\tilde{g}^R\tilde{g}^K = -\tilde{g}^K\tilde{g}^A \tag{3.11}$$

and to one another by

$$\tilde{g}^A = -\tau^3(\tilde{g}^R)^\dagger\tau^3 \tag{3.12}$$

where $\tilde{g}^K$ is needed to account for the non-equilibrium properties of the system, including the flow of current. The normalization condition

$$\tilde{g}^R\tilde{g}^R = \tilde{g}^A\tilde{g}^A = \tau^0 \tag{3.13}$$

where τ^0 is the identity matrix, and the fact that the distribution function $\tilde{h}$ is related to $\tilde{g}^K$ through the energy integral

$$\tilde{h}(\mathbf{R}, T, \mathbf{p}) = \frac{i}{2\pi}\int dE\ \tilde{g}^K(\mathbf{R}, T; \mathbf{p}, E) \tag{3.14}$$

means that $\tilde{g}^K$ may be parameterized by the ansatz

$$\tilde{g}^K = \tilde{g}^R\tilde{h} - \tilde{h}\tilde{g}^A \tag{3.15}$$

where $\tilde{h}$ is typically represented in a form diagonal in Nambu-Gor'kov space as [53]

$$\tilde{h} = h_T\tau^0 + h_L\tau^3 \tag{3.16}$$

The equilibrium forms of h_T and h_L will be useful later in our parameterization of the Usadel equation. The diagonal components of Eq. (3.9) expressed in the Keldysh space involve only the equilibrium properties of the system, $\tilde{g}^R$ and $\tilde{g}^A$, while the off-diagonal components describe the non-equilibrium properties captured by $\tilde{g}^K$ and $\tilde{h}$.

The advantage of the Keldysh formulation is that the expectation values of physical quantities may be related to the Green's functions defined in Keldysh space. For instance, the quasiparticle electrical current, which is calculated by integrating the distribution function with energy, becomes [49]

$$\mathbf{j}(\mathbf{R}, T) = -eN_0 \int_{-\infty}^{\infty} dE \ \mathrm{Tr}\langle \mathbf{v}_F \tau^3 \tilde{g}^K(\mathbf{v}_F, \mathbf{R}, T, E)\rangle \tag{3.17}$$

after making use of Eq. (3.14). Since $\tilde{h}$ was designed to be a diagonal matrix in particle-hole space, taking the trace of $\tilde{g}^K$ incorporates current contributions from both electrons and holes.

3.2.2 Kinetic equations

The off-diagonal Keldysh component of the Usadel equation

$$[\tau^3 E + \tilde{\Delta}, \tilde{g}^R] = iD\partial_{\mathbf{R}}[(\tilde{g}^R\partial_{\mathbf{R}}\tilde{g}^K) + (\tilde{g}^K\partial_{\mathbf{R}}\tilde{g}^R)] \tag{3.18}$$

represents the *kinetic equation* for the distribution function describing the transport properties of NS heterostructures. Using Eq. (3.15) and (3.16), we may rewrite this equation solely in terms of the distribution functions and the equilibrium Green's functions $\tilde{g}_s^R$ and $\tilde{g}_s^A$ as

$$D\partial_{\mathbf{R}}[(\partial_{\mathbf{R}}h_L)\mathrm{Tr}\{1-\tilde{g}^R\tilde{g}^A\}+h_T\mathrm{Tr}\{\tau^3(\tilde{g}^R(\partial_{\mathbf{R}}\tilde{g}^R)-\tilde{g}^A(\partial_{\mathbf{R}}\tilde{g}^A))\} - (\partial_{\mathbf{R}}h_T)\mathrm{Tr}\{\tilde{g}^R\tau^3\tilde{g}^A\}]=0 \quad (3.19)$$

and

$$D\partial_{\mathbf{R}}[(\partial_{\mathbf{R}}h_T)\mathrm{Tr}\{1-\tilde{g}^R\tau^3\tilde{g}^A\tau^3\}+h_L\mathrm{Tr}\{\tau^3(\tilde{g}^R(\partial_{\mathbf{R}}\tilde{g}^R)-\tilde{g}^A(\partial_{\mathbf{R}}\tilde{g}^A))\} - (\partial_{\mathbf{R}}h_L)\mathrm{Tr}\{\tilde{g}^R\tilde{g}^A\tau^3\}]=i[h_L\mathrm{Tr}\{\tau^3[\tilde{g}^R-\tilde{g}^A,\tilde{\Delta}]\}-2h_T\mathrm{Tr}\{\tau^3[\tilde{\Delta}(\tilde{g}^R+\tilde{g}^A)\}] \quad (3.20)$$

which together form a set of coupled differential equations for the distribution functions h_L and h_T (see Ref. [40] for the full derivation). From these equations, it is convenient to define the *spectral supercurrent*

$$Q=\frac{1}{4}\mathrm{Tr}\{\tau^3(\tilde{g}^R(\partial_{\mathbf{R}}\tilde{g}^R)-\tilde{g}^A(\partial_{\mathbf{R}}\tilde{g}^A)\} \quad (3.21)$$

and the normalized energy- and position-dependent *diffusion coefficients*

$$M_{ij}=\frac{1}{4}\mathrm{Tr}\{\delta_{ij}\tau^0-\tilde{g}^R\tau^i\tilde{g}^A\tau^j\} \quad (3.22)$$

such that Eq. (3.19) and Eq. (3.20), respectively, become

$$\partial_{\mathbf{R}}[M_{00}(\partial_{\mathbf{R}}h_L)+Qh_T+M_{30}(\partial_{\mathbf{R}}h_T)]=0 \quad (3.23)$$

and

$$\partial_{\mathbf{R}}[M_{33}(\partial_{\mathbf{R}}h_T) + Qh_L + M_{03}(\partial_{\mathbf{R}}h_L)] \\ = \frac{i}{4D}[h_L \mathrm{Tr}\{\tau^3[\tilde{g}^R - \tilde{g}^A, \tilde{\Delta}]\} - 2h_T \mathrm{Tr}\{[\tilde{\Delta}(\tilde{g}^R + \tilde{g}^A)\}] \quad (3.24)$$

These equations are generalized forms of the Boltzmann *diffusion equations* for quasiparticle distribution functions h_L and h_T. They may be used to calculate the electrical current and DOS in a system with defined boundary conditions. The current may be represented

$$\mathbf{j}(\mathbf{R}, T) = eN_0 D \int dE\ (M_{33}(\partial_{\mathbf{R}}h_T) + Qh_L + M_{03}(\partial_{\mathbf{R}}h_L) \quad (3.25)$$

where the first term corresponds to quasiparticle current, the second term to supercurrent, and the third term to charge imbalance between electrons and holes The superconducting DOS is defined

$$N(E) = \frac{1}{2}\mathrm{Tr}\{\tau^3(\tilde{g}^R - \tilde{g}^A)\} \quad (3.26)$$

which in the equilibrium case for a pure superconductor reduces to the familiar DOS with energy gap Δ [40] (see Eq. (2.7)). We will now apply the diffusion equations to real-world problems involving NS structures using numerical techniques to solve Eq. (3.25) and Eq. (3.26).

3.2.3 Boundary conditions

The Usadel equation in proximity-coupled normal metal wires must be solved subject to a set specified of boundary conditions. To facilitate numerical solutions, several assumptions are usually made about the physical properties of a real device. First, we define a *reservoir* for both normal and superconducting electrodes where the Green's function and distribution function have well-

defined values. The basic principle is that for whatever non-equilibrium dynamics occur inside the wire, the reservoir values are left unchanged.

The retarded Green's function in a normal reservoir is simply $\tilde{g}^R_{N0} = \tau^3$ and for the superconducting reservoir [40]

$$\tilde{g}^R_{S0} = \begin{pmatrix} \frac{E}{\sqrt{E^2-|\Delta|^2}} & \frac{\Delta}{\sqrt{E^2-|\Delta|^2}} \\ \frac{-\Delta^*}{\sqrt{E^2-|\Delta|^2}} & \frac{-E}{\sqrt{E^2-|\Delta|^2}} \end{pmatrix} \tag{3.27}$$

For numerical simulations shown in this thesis, all superconducting electrodes are treated as reservoirs since the size of the superconducting measurement leads are much larger than the normal metal wires connecting them.

In anticipation of real measurements where a small voltage is applied across a set of reservoirs at finite temperatures, the distribution matrix, which is diagonal in particle-hole space, may be defined

$$\tilde{h}_0 = \begin{pmatrix} \tanh\left(\frac{E}{2k_bT}\right) & 0 \\ 0 & \tanh\left(\frac{E}{2k_bT}\right) \end{pmatrix} \tag{3.28}$$

in a reservoir, which, after using Eq. (3.16), gives

$$h_{L,T} = \frac{1}{2}\left(\tanh\left(\frac{E+eV}{2k_bT}\right) \pm \tanh\left(\frac{E-eV}{2k_bT}\right)\right) \tag{3.29}$$

Note that $(\tanh(x/2)+1)/2 = f(x)$, our usual Fermi distribution function. The non-equilibrium distribution functions vary with position along points in the device and must be determined by solving the non-equilibrium kinetic equations in Keldysh space.

Fortunately, we may make another simplification. If we consider the normal metal wires only, where the superconducting order parameter $\Delta = 0$, Eq. (3.24) reduces to

$$\partial_{\mathbf{R}}[M_{33}(\partial_{\mathbf{R}}h_T) + Qh_L + M_{03}(\partial_{\mathbf{R}}h_L)] = 0 \tag{3.30}$$

and, since we are not applying voltage across the superconductors on either side of the normal metal, $V = 0$ in the superconducting reservoirs. Therefore, by Eq. (3.29), the spatial derivatives of the distribution functions vanish, and the charge current Eq. (3.25) becomes

$$j(\mathbf{R}, T) = eN_0D \int dE\ Q(E)h_L(E) \tag{3.31}$$

with $h_L(E) = \tanh(E/2k_bT)$. In the low temperature limit, $h_L \approx 1$ and simply integrating over the spectral supercurrent gives the physical (and measurable) charge current in the device.

The second set of boundary conditions, which is essentially Kirchhoff's law, is more relevant for multiterminal geometries. It requires the net charge current entering from various points in the device to sum to zero. If, for instance, multiple leads intersect at a common node, then the total current entering the node equals the total current leaving the node. Quantitatively, this means $\sum_i \tilde{g}^R(\partial_{\mathbf{R}}\tilde{g}^R) = 0$ at the node, and a similar condition holds for the charge currents [54].

For the last boundary condition, the interfaces between superconductor and normal metal are idealized to be perfectly transparent. This means that the value of the Green's function in the normal metal exactly at the interface is given by the equilibrium value of the Green's function for the superconducting reservoir, Eq. (3.27) [54]. For interfaces of finite transparency in the dirty limit, the Green's function dependence on barrier resistance R_b was worked out by Kuprianov and Lukichev [55]. In the following scenarios in which we apply the quasiclassical techniques, however, we assume negligible R_b for all NS interfaces.

3.2.4 Parameterization

To facilitate numerical solutions, one may leverage the normalization conditions Eq. (3.12) and Eq. (3.13) to express $\tilde{g}^R$ in terms of a convenient parameter. Two of the more common choices are the so-called θ *parameterization* [40], [49], [56] and *Riccati parameterization* [57]–[59] described with the coherent functions γ and $\tilde{\gamma}$. Let us first consider the θ parameterization in which the equilibrium Green's functions are expressed

$$\tilde{g}^R = \begin{pmatrix} \cosh\theta & \sinh\theta e^{i\chi} \\ -\sinh\theta e^{-i\chi} & -\cosh\theta \end{pmatrix} \tag{3.32}$$

$$\tilde{g}^A = \begin{pmatrix} -\cosh\theta^* & -\sinh\theta^* e^{i\chi^*} \\ \sinh\theta^* e^{-i\chi^*} & \cosh\theta^* \end{pmatrix} \tag{3.33}$$

Here, $\theta(E, \mathbf{R})$ and $\chi(E, \mathbf{R})$ are complex functions that roughly describe the strength and phase of the pair correlations, respectively [56]. Note that it is also possible to parameterize $\tilde{g}^{R,A}$ in terms of sine and cosine functions for a different choice of gauge for the field operators in Eq. (3.3) [60].

If Eq. (3.32) is inserted into the Usadel equation for the retarded Green's function, the resulting $(1,1)$ and $(1,2)$ components of the 2×2 matrix equation are, respectively,

$$D\sinh^2(\theta)\,\partial_{\mathbf{R}}^2\chi + D\sinh(2\theta)\,\partial_{\mathbf{R}}\chi\,\partial_{\mathbf{R}}\theta = 2i\mathrm{Im}(\Delta)\sinh(\theta) \tag{3.34}$$

and

$$D\partial_{\mathbf{R}}^2\theta - \frac{D}{2}\sinh 2\theta(\partial_{\mathbf{R}}\chi)^2 + 2Ei\sinh\theta - 2i\mathrm{Re}(\Delta)\cosh\theta = 0 \tag{3.35}$$

which together form a pair of coupled equations which may be solved for θ and χ given a set of specified boundary conditions. To derive the transport properties of the device, we may write the

expressions for physical quantities M_{ij} and Q as

$$M_{00,33} = \frac{1}{2}\left[1 + \left(\cosh\theta\cosh\theta^* \mp \sinh\theta\sinh\theta^* e^{i(\chi-\chi^*)}\right)\right], \tag{3.36}$$

$$M_{03,30} = \mp\frac{i}{2}\left[\sinh\theta\sinh\theta^*\sin\left(\chi-\chi^*\right)\right] \tag{3.37}$$

and

$$Q = -\mathrm{Im}(j_s(E,\mathbf{R})) \tag{3.38}$$

where the spectral supercurrent j_s is proportional to the phase gradient through

$$j_s(E,\mathbf{R}) = \sinh^2\theta(E,\mathbf{R})\partial_{\mathbf{R}}\chi(E,\mathbf{R}) \tag{3.39}$$

This system of equations is nonlinear in the diffusive limit and requires numerical techniques to find a solution. The kinetic equations must be solved iteratively until the entire system converges [40].

As an example problem, consider a normal 1D wire of length L attached to superconducting reservoirs at either end shown in Fig. 3.2(a). The θ-parameterized Green's function is used to calculate the quasiparticle DOS in the SNS junction. From Eq. (3.26), the normalized DOS may be expressed in terms of θ as

$$N(E) = \cos(\mathrm{Re}(\theta))\cosh\left(\mathrm{Im}(\theta)\right) \tag{3.40}$$

and the energy minigap 2δ which corresponds to the maximum value of E, is found in two limiting cases to be [61]

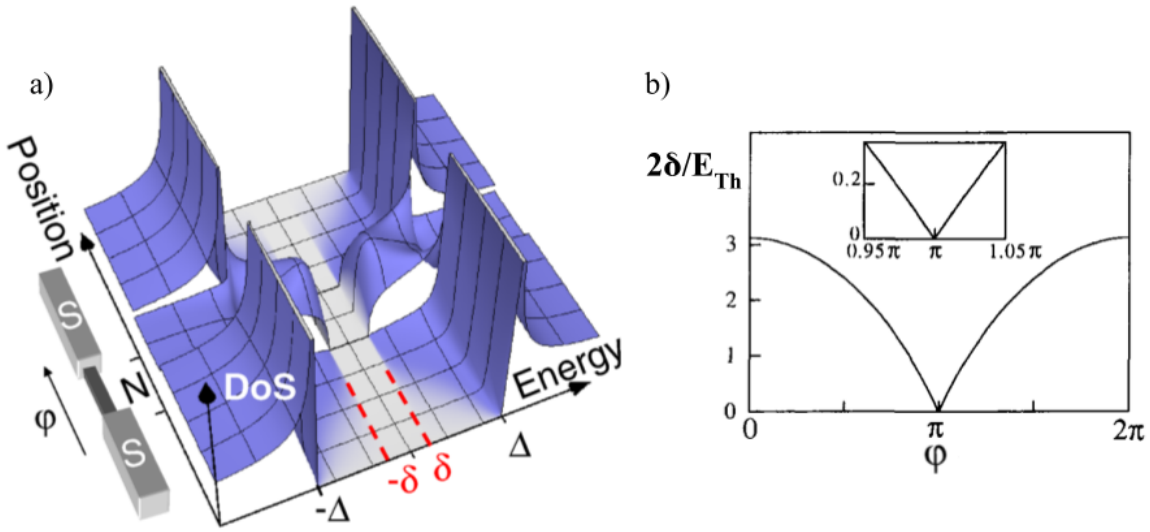

Figure 3.2: **Quasiparticle DOS in a long SNS junction.** (a) Simulated DOS showing a divergence at the gap edge and position-independent minigap in the normal metal. Figure from Ref. [63]. (b) Minigap as a function of ϕ. Inset: linear dependence of δ near $\phi = \pi$ where the gap closes. For $\phi = 0$ and 2π, $\delta \approx 1.5\, E_{\text{Th}}$. Figure adapted from Ref. [61].

$$2\delta/E_{\text{Th}} = \begin{cases} C_2(1 - C_1\phi^2) & \phi \ll \pi \\ C_3(\pi - \phi) & \pi - \phi \ll \pi \end{cases} \tag{3.41}$$

as shown in Fig. 3.2(a) where C_i are constants of integration. The most important results from the simulation are the following. The width of the minigap δ in the normal metal is constant along the entire length of the wire, and, as shown more clearly in Fig. 3.2(b), its magnitude is modulated by the phase difference ϕ between the superconducting electrodes. The phase-sensitivity of the minigap magnitude is a characteristic feature of a *long* SNS junction where $E_{\text{Th}} \ll \Delta$ [62]. We will use the fact that the DOS is tunable by phase in our experiments on long SNS junctions.

We now examine the supercurrent j_s resulting from the phase difference ϕ: the CPR of an SNS junction. Theoretically, this is done by applying a boundary condition for the gauge-invariant phase χ at the superconducting reservoirs anti-symmetrically. That is, for the left NS interface at position $x = 0$, we set $\chi_L = -\pi\Phi/\Phi_0$ and at $x = L$, we set $\chi_R = \pi\Phi/\Phi_0$. Then, the coupled equations Eq. (3.34) and Eq. (3.35) are solved for θ and χ with the constraint that $\Delta = 0$ inside the normal metal wire [64]. For perfectly transparent interfaces, θ in the wire at $x = 0, L$ is

$$\theta = \theta_{S0} = \begin{cases} -i\frac{\pi}{2} + \frac{1}{2}\ln\frac{|\Delta|+E}{|\Delta|-E} & E < |\Delta| \\ \frac{1}{2}\ln\frac{|\Delta|+E}{|\Delta|-E} & E > |\Delta| \end{cases} \tag{3.42}$$

using the equilibrium value of the Green's function in the superconducting reservoir [40].

Recall that we are assuming zero voltage difference between superconductors. How, then, would we experimentally phase-bias an SNS junction to match our simulations? One solution is to form a loop with the two superconducting electrodes. Due to the single-valuedness of the superconducting wave function, the phase must return to its original value modulus 2π upon circling the loop. If a magnetic flux Φ penetrates the loop, a screening supercurrent I_s will be induced, and in the segment where the critical current I_c is smallest — the part with the normal metal — the largest change in phase will occur. Effectively, this means that a phase difference $2\pi\Phi/\Phi_0$ where $\Phi_0 = h/2e$ is the superconducting flux quantum will result across the SNS junction [8]. We will take advantage of this particular SNS JJ configuration to phase-tune the DOS in the Chapter 6.

For now, we consider the spectral supercurrent given by Eq. (3.38). Figure 3.3(a) shows the numerically calculated $Q(E)$ using Eq. (3.39) for various phase differences across the junction. As seen from the plot, the greatest contributions to the supercurrent come from energies $E \sim E_{\text{Th}}$. These quasiparticles have the greatest impact on the CPR. Quasiparticles with energies greater than Δ have little effect on the supercurrent, since, as previously discussed, they participate less in

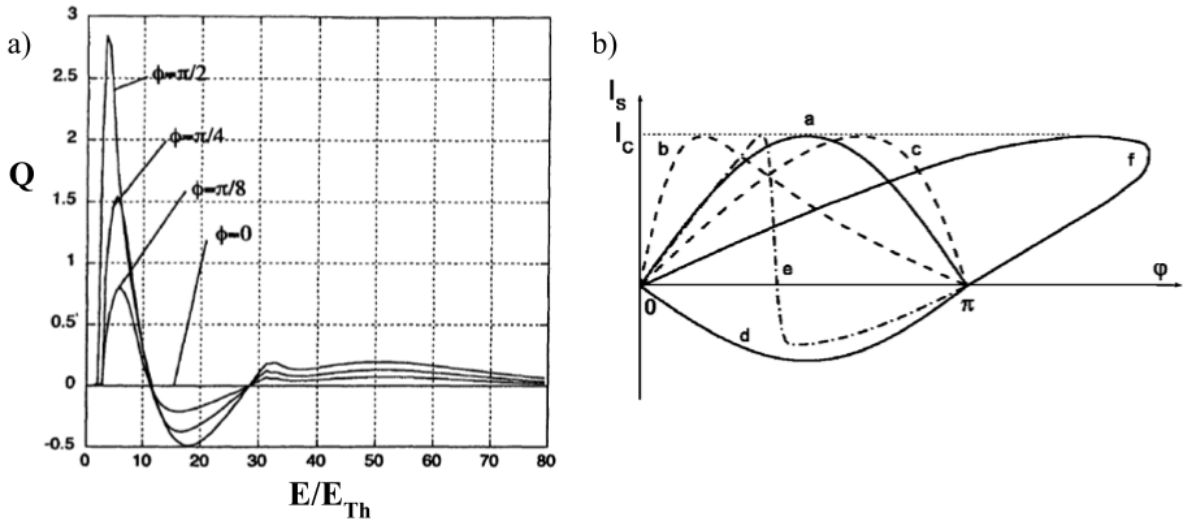

Figure 3.3: **Spectral supercurrent and CPRs of an SNS junction.** (a) Q numerically calculated using Eq. (3.38) in the long-junction limit where $\Delta = 32\,E_{\text{Th}}$. Integrating $Q(E)$ gives the total supercurrent across the junction. Figure adapted from Ref. [40]. (b) Various CPRs resulting from $Q(\phi)$. (a) standard sinusoidal form, (b) and (c) slight deviations from the sinusoidal form, (d) phase-shifted CPR from a "π"-junction, (e) I_c minima doubling, and (f) multi-valued CPR arising from mechanisms other than the Josephson effect. Figure from Ref. [47].

Andreev processes. As ϕ approaches zero, the amplitude of Q decreases. At $\phi = 0$, $Q = 0$ and no supercurrent flows across the junction as one expects from the phase-periodicity of the CPR. Depending on the exact form of the kinetic equations, the CPR may be non-sinusoidal as shown in Fig. 3.3(b).

Lastly, we consider an alternative parameterization of the quasiclassical Green's function which may assist simulating devices with more complicated geometries [54], [59]. In particular, we consider the case where *normal reservoirs* are added to the multiterminal device for *conductance* measurements. Here, the Riccati parameterization [57] offers advantages over the θ parameteri-

zation in terms of convergence in numerical simulations [59]. In this case, the retarded Green's function is expressed

$$\tilde{g}^R = \frac{1}{1+\gamma\tilde{\gamma}} \begin{pmatrix} 1-\gamma\tilde{\gamma} & 2\gamma \\ 2\tilde{\gamma} & \gamma\tilde{\gamma}-1 \end{pmatrix} \tag{3.43}$$

and we proceed similarly to the θ parameterization, obtaining from the $(1,2)$ and $(2,1)$ components of the Usadel equation a pair of differential equations for γ and $\tilde{\gamma}$,

$$D\left[\partial_{\mathbf{R}}^2\gamma - \frac{2\tilde{\gamma}}{1+\gamma\tilde{\gamma}}(\partial_{\mathbf{R}}\gamma)^2\right] + 2iE\gamma = 0 \tag{3.44}$$

and

$$D\left[\partial_{\mathbf{R}}^2\tilde{\gamma} - \frac{2\gamma}{1+\gamma\tilde{\gamma}}(\partial_{\mathbf{R}}\tilde{\gamma})^2\right] + 2iE\tilde{\gamma} = 0 \tag{3.45}$$

The spectral supercurrent is

$$Q = 2\mathrm{Re}\left[\frac{1}{(1+\gamma\tilde{\gamma})^2}(\gamma\partial_{\mathbf{R}}\tilde{\gamma} - \tilde{\gamma}\partial_{\mathbf{R}}\gamma)\right] \tag{3.46}$$

and the modified diffusion coefficients M_{ij} are

$$M_{00,33} = \frac{1}{|1+\gamma\tilde{\gamma}|^2}[(|\gamma|^2 \mp 1)(|\tilde{\gamma}|^2 \mp 1)] \tag{3.47}$$

and

$$M_{30,03} = \mp\frac{1}{|1+\gamma\tilde{\gamma}|^2}(|\gamma|^2 - |\tilde{\gamma}|^2) \tag{3.48}$$

At this point, device-specific boundary conditions are specified and we proceed to solve for charge current $\mathbf{j}$ and the DOS in terms of $\gamma(E,\mathbf{R})$ and $\tilde{\gamma}(E,\mathbf{R})$.

Let us summarize the steps used to simulate these measurable quantities using the Ricatti pa-

rameterization in MTJJs. Supercurrent in the device is created from a phase difference across a pair of superconducting contacts. The phases $\phi_1, \phi_2 ... \phi_N$ are assigned to superconducting reservoirs 1 to N. Without loss of generality, we usually set $\phi_1 = 0$ to simplify the calculation. In the simulations, these phases are accounted for through the gap $\Delta = |\Delta| e^{i\phi}$ found in the equilibrium form of our Riccati parameters after applying boundary conditions. Since we are phase-biasing the superconducting reservoirs, we set voltage V to be zero in every superconducting reservoir. This means the gradient of equilibrium distribution functions $\partial_{\mathbf{R}} h_T$ and $\partial_{\mathbf{R}} h_L$ vanish and the only term contributing to the charge current in Eq. (3.25) is the spectral supercurrent Q. The NS interfaces are assumed to be perfectly transparent, and the superconducting Green's function resulting from our choice of phase is attributed to the normal metal at the interface. Solving the Usadel equation with these Green's functions allows one to calculate the quasiparticle DOS at any point inside the normal metal wires.

In a conductance measurement, additional normal metal leads may be attached to the MTJJ. In this case, a small voltage bias V is set symmetrically across two normal reservoirs attached to the normal metal weak link. The addition of normal metal reservoirs modifies the DOS such that the minigap is *not* uniform across the entire wire. Re-solving the kinetic equations enables one to calculate the resulting quasiparticle current entering the normal contact and thus the resistance between the normal reservoirs. At other points along the device, $h_{L,T}$ are functions of position and must be determined by solving the kinetic equations satisfied by the Keldysh component of the Green's function. We deploy such numerical simulations on devices shown in Chapter 6.

With an overview of the quasiclassical theory completed, we transition into a discussion of prior work on MTJJ most relevant to our experiments.

3.3 Multiterminal Josephson junctions — prior work

The first category of MTJJ proposals involves junctions made from topological superconductors. Majorana zero modes residing in these devices may help realize topologically protected quantum computers [65]–[68]. Pending its discovery, a device containing Majoranas is considered the holy grail of solid state physics. For our interest, however, the attractiveness of the multiterminal platform is the ability to probe interesting physics *without* the need for exotic materials. The MTJJ discussed in this thesis are fabricated from conventional s-wave superconductors and normal conductors.

A major thrust of theoretical work on MTJJs explores the "band structure" formed from the discrete energies of the ABSs contained within a ballistic weak link. The basic idea, initially proposed by Riwar *et al.* [69], is the following. The energy levels of Andreev quasiparticles disperse with the phase difference ϕ much the same way the energies of electrons in a 1D crystal lattice disperse with quasi-momentum k. In both cases, the energy levels are periodic functions, returning to zero with respect to E_F at particular values of ϕ or k. In a normal metal connected to *three* superconductors with two independent phase differences $\phi_{1,2}$, the energy dispersion maps onto a *2D* crystal with distinct quasi-momenta $k_{1,2}$. In multiterminal junctions with N superconducting terminals, the possibility exists of creating a $(N-1)$-dimensional "artificial crystal" whose band structure may be directly probed by experiments. Whereas crystal quasi-momentum is difficult to control experimentally, the phase difference in SNS junctions may be accessed via the CPR or, better yet, with a phase-biased loop discussed in the previous section. Ultimately, it is the *tunability* of MTJJs that makes them an attractive platform for investigating novel effects, such as the topological character of the Andreev band structure [69]–[73].

Riwar *et al.* model the normal metal in their MTJJ as a scattering matrix in the clean limit.

As such, quasiparticles only scatter at the boundaries of the device. In this case, one may apply the Bohr-Sommerfeld quantization condition to the interference of the twice-reflected electron and original electron to find ABS energies $E_{\mathrm{ABS}} = \pm\Delta\cos(\phi/2)$ [74]. At a phase difference $\phi = \pi$, the energy gap in the MTJJ closes as shown in Fig. 3.4(a). The prediction is that the regions in phase space on either side of this gap closing are topologically distinct, identified by different Chern numbers, and that traversing from one topologically distinct region to another *requires* a closing of the gap. Through the bulk-boundary correspondence, one may be able to measure quantized edge modes depending on the topological index of the gapped non-trivial topological phase [75].

Outside of the clean limit, theoretical proposals from Amundsen *et al.* [71] and Vischi *et al.* [72] discuss the topological properties of *diffusive* normal metal coupled to three or more superconductors. ABSs in diffusive junctions are not well-defined, yet the minigap in the quasiparticle DOS still forms a periodic function of phase (see Fig. 3.2(b)). Riccati-parameterizing the Usadel equation, Amundsen *et al.* analytically calculate the phase-dependent DOS at the intersection of a three-terminal junction. See Fig. 3.4(b) for an example of their quasiclassical simulation results.

To see *why* these gap closings may be topological, we consider the work by Strambini *et al.* [70] which is the only prior experimental study probing the topological nature of diffusive MTJJs. For their phase-biased multiterminal device pictured in Fig. 3.5(a), Strambini *et al.* define a pair of topological integer indices related to different gapped regions in phase space. The device contains two loops, one connecting the bottom and left superconducting terminals and the other connecting the bottom and right terminals. The first integer represents the winding number of the phase around left loop and the second integer represents the same for the right loop. See Fig. 3.5(b). By applying an external magnetic field through the loops, the two phases are *simultaneously* wound such that the minigap in the normal metal is opened, closed and opened again. Due to the topological protection of the Green's function, diagrammatically depicted on a Bloch sphere in Fig. 3.5(c)), the first gap

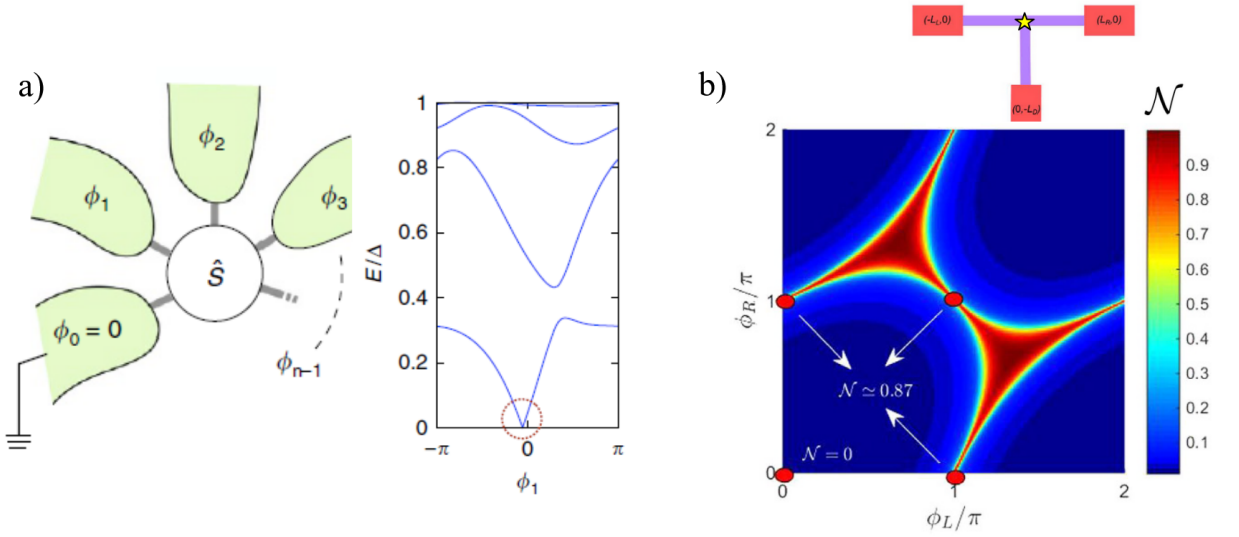

Figure 3.4: **Topological gap closing in MTJJs.** (a) N superconducting contacts with distinct phases ϕ_{N-1} connected to a ballistic scattering matrix $\hat{S}$. Generalized ABS spectrum with a gap closing circled in red analogous to topological Weyl point. Figure from Ref. [69]. (b) Quasiparticle DOS at the intersection of the three-terminal device denoted with a yellow star as a function of the phase difference between the left and middle (ϕ_L) and right and middle (ϕ_R) superconductors. Dark blue region corresponds to a minigap in the normal metal. Figure from Ref. [71].

opening is denoted with indices (00) and the second with (11).

Experimentally, the minigaps are probed with tunneling conductance spectroscopy. A normal metal-insulator-normal metal (NIN) junction is formed between the normal metal weak link and a voltage probe. The conductance between the probe and the weak link is a direct function of the available electronic states at the contact point. Conductance increases with a higher density of states (similar to thermally excited quasiparticles across an SIS junction from Chapter 2). As a function of applied field, clear modulations in the tunneling conductance were observed in the device corresponding to phase-induced gap closings in the DOS. An example of this data is shown in Fig. 3.5(d). It is a goal of this thesis to further our understanding of the topological proximity-induced gap in diffusive MTJJs. In doing so, we opt for several experimental techniques that differ

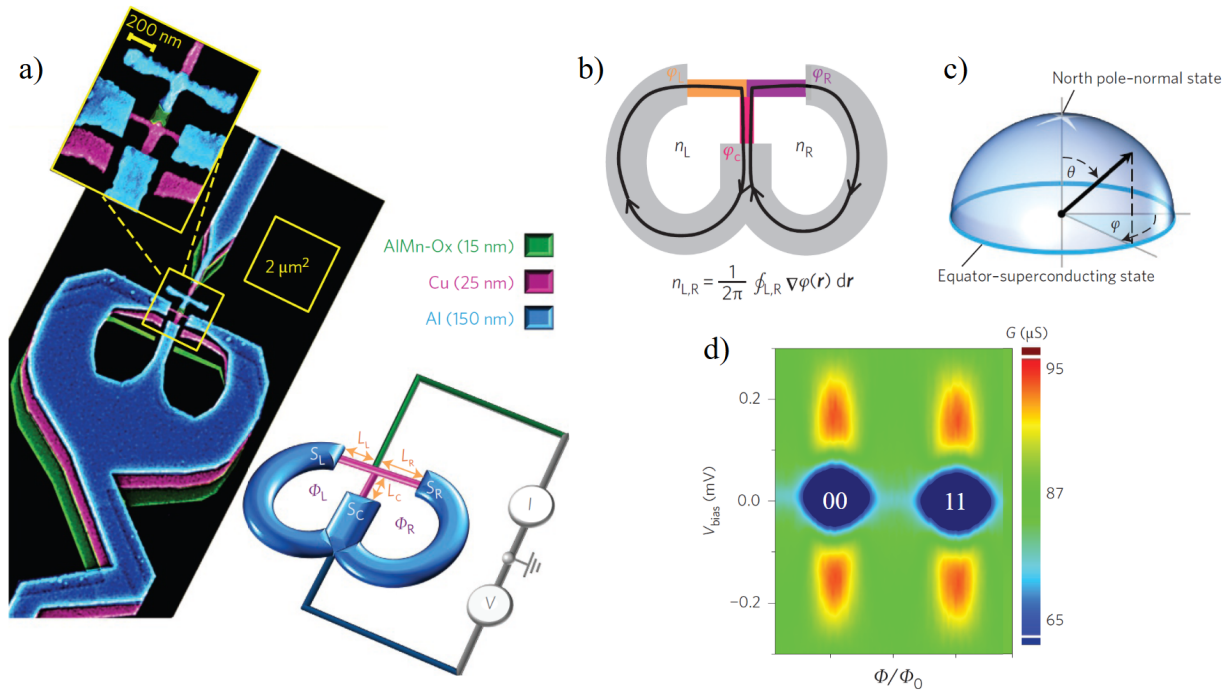

Figure 3.5: **Tunneling conductance spectroscopy on a phase-biased diffusive three-terminal junction.** (a) Colorized SEM image of a double-loop device fabricated via shadow evaporation. (b) Device schematic showing how the topological indices are defined by the winding number of the phases around the loops. (c) Bloch sphere representation of the θ-parameterized Green's function. Polar angle θ represents the strength of superconductivity in the normal metal, azimuthal angle ψ represents the superconducting phase. $\theta = 0$ and $\theta = \pi/2$ correspond to the pure normal and superconducting states, respectively. (d) Tunneling conductance data reflecting topologically distinct gaps in the quasiparticle DOS. Figure adapted from Ref. [70].

from those used by Strambini *et al.*. We discuss these techniques and our results in Chapter 6.

Excluding Strambini *et al.*, most previous experiments on MTJJ deploy a current-biasing measurement scheme. Found frequently in the literature is the *differential resistance heat map* plotted as a function of bias current through various terminals in the MTJJ. Essentially, in a three-terminal device, one superconducting terminal is grounded to drain supercurrent injected from the other two terminals. As a function of these two supercurrents, the local differential resistance dV/dI is measured across one pair of leads. The resulting heat map shows the critical current contour

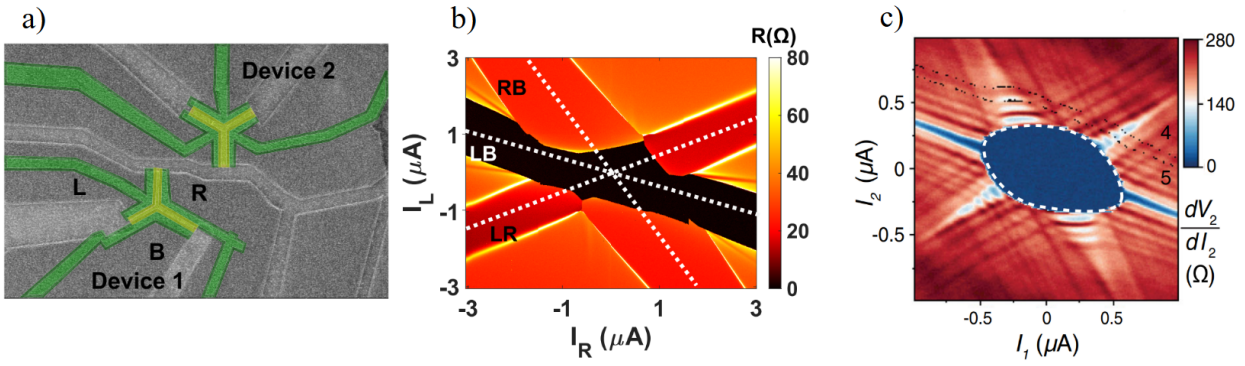

Figure 3.6: **Differential resistance heat maps of ballistic MTJJs.** (a) Graphene-based three-terminal junction from Finkelstein group with MoRe superconducting terminals. (b) Resistive heat maps as a function of current bias for "Device 1." Bottom electrode is grounded. Dotted lines mark the currents between bottom (B), left (L) and right (R) leads. Figures from Ref. [77]. (c) Resistive heat map from a three-terminal proximity-coupled InAs device from Ref. [76]. CCC outlined in a white dotted line. Radial features attributed to "quartet" transport. Black dotted lines mark equipotential lines corresponding to multiple Andreev reflection resonances.

(CCC) [76] — the 2D perimeter outlining the zero-voltage region — from which many different transport phenomena are inferred. The basic purpose of the CCC is to track supercurrent across one junction as a function of supercurrent across the other.

MTJJ current-biased heat maps have garnered attention for their correlated Josephson effects. In particular, experiments from the Finkelstein group have explored the supercurrent flow [78], [79] and ac Josephson effect in the presence of microwave radiation [77] in ballistic MTJJs made from graphene. See Fig. 3.6(a) for an image of their sample and Fig. 3.6(b) for an example heat map. Notable "streaking" features are explained using a three-junction RCSJ model in which the Josephson phase traverses a 2D washboard potential [77]. The RCSJ model has also been applied to MTJJ fabricated from proximity-coupled InAs [80] where the Josephson diode effect is predicted [81].

Supercurrent-enhanced streaking in heat maps also suggest the existence of so-called Cooper "quartets" carried in ballistic [82], [83] and diffusive [84] MTJJs. Cooper quartets represent the

non-local $4e$ charge transfer across the normal metal weak link due to the entangled state of Cooper pairs between a pair of superconducting leads. Evidence of a π-shifted Josephson effect from the transport of quartets was recently observed in a three-terminal junction fabricated from PbTe nanowires [85].

In prior work on three-terminal junctions, limitations of the device design prevented most of the 2D phase space from being probed. In the case of Strambini *et al.*, a double-loop geometry allowed access to the DOS only along the line $\phi_1 = \phi_1$, severely restricting control over the topological Green's function. In Chapter 6, we show that with particular choices in device design, one may tune each phase independently to probe the entirety of the topological phase space. Additionally, while the resistive heat maps of MTJJ have been studied extensively for indications of correlated quasiparticles, little attention has been paid to how one may utilize these devices in superconducting circuits. In Chapter 6, we offer a potential application for current-biased MTJJ in the field of superconducting qubits.

CHAPTER 4
EXPERIMENTAL METHODS

In this thesis, SIS junctions are made from Al and AlO_x, and SNS junctions are made from Al and Au. Historically, this lab has maintained a "farm-to-table" work ethic, starting and completing projects entirely in-house. In the case of Al/AlO_x/Al junctions, however, low-temperature measurements were performed on a variety of samples fabricated inside *and* outside the lab. We contrast the lithographic technique used in this lab, the "Dolan bridge" method, with the alternative "bridgeless" technique of externally fabricated devices. Details of the measurement environment are given special consideration since, as discussed in Chapter 2, the impedance of the environment plays a role in IV characteristics.

The fabrication procedure for SNS structures has been covered extensively by previous members of this group, most recently in Refs. [86] and [87]. The process was recovered somewhat from scratch, including through the rehabilitation of an ultra-high-purity thermal evaporator. We delve into specific lithography, metalization and wirebonding details, all of which were rediscovered by the author. Since the methods involved in the fabrication of SNS junctions are distinct from those used to fabricate SIS junctions, we treat them in separate sections.

All measurements were performed in one of two cryogenic systems with base temperatures of 20 and 270 mK using low-noise dc transport techniques. Our lab employs a variety of tools and strategies to maximize the signal-to-noise ratio measured from low- and high-impedance samples alike. Oftentimes, the differential resistance dV/dI is measured as a function of other variables such as temperature T, bias supercurrent I, and magnetic field B. The measurement strategies for superconducting mesoscopic devices are tried and true, and covered extensively in previous theses,

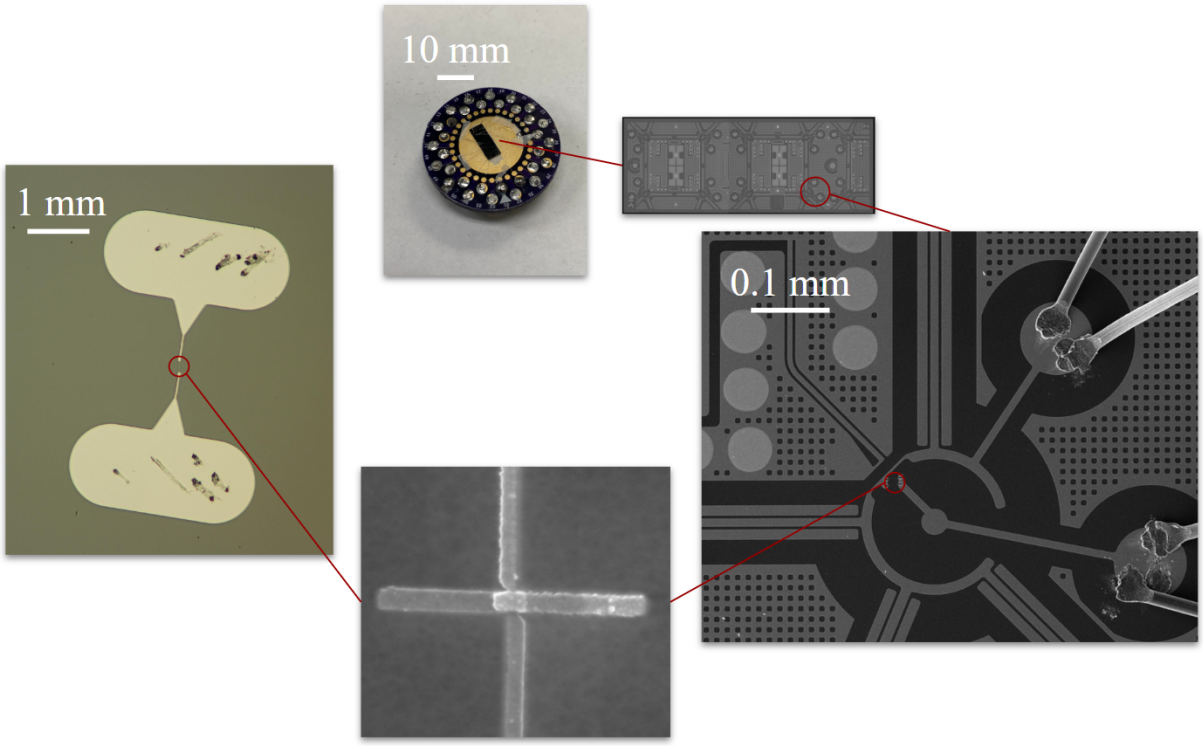

Figure 4.1: **Standalone vs transmon junction geometry.** (Top) PCB header holding a wirebonded transmon chip. (Right) A low-magnification SEM image of the transmon chip. The Si substrates are first patterned with a Nb circuitry layer before being electrically connected to the Al JJs with an Al "patch" deposited in a subsequent lithographic step [38]. (Left) Optical image of a standalone junction with minimal capacitance between large area leads. (Bottom) A high-magnification SEM image of an Al/AlO_x/Al junction.

most relevantly in Refs. [86]–[91]. We provide an overview of these techniques here.

4.1 Fabrication methods — SIS junctions

Two varieties of SIS junctions were studied: those intended for use in superconducting qubits fabricated outside our lab, and those fabricated as controls inside the lab. All junctions were made using variations on the double-angle evaporation technique. In total, a couple dozen SIS junctions were cooled down and measured for this thesis. A few were fabricated at NIST, a few at Fermilab,

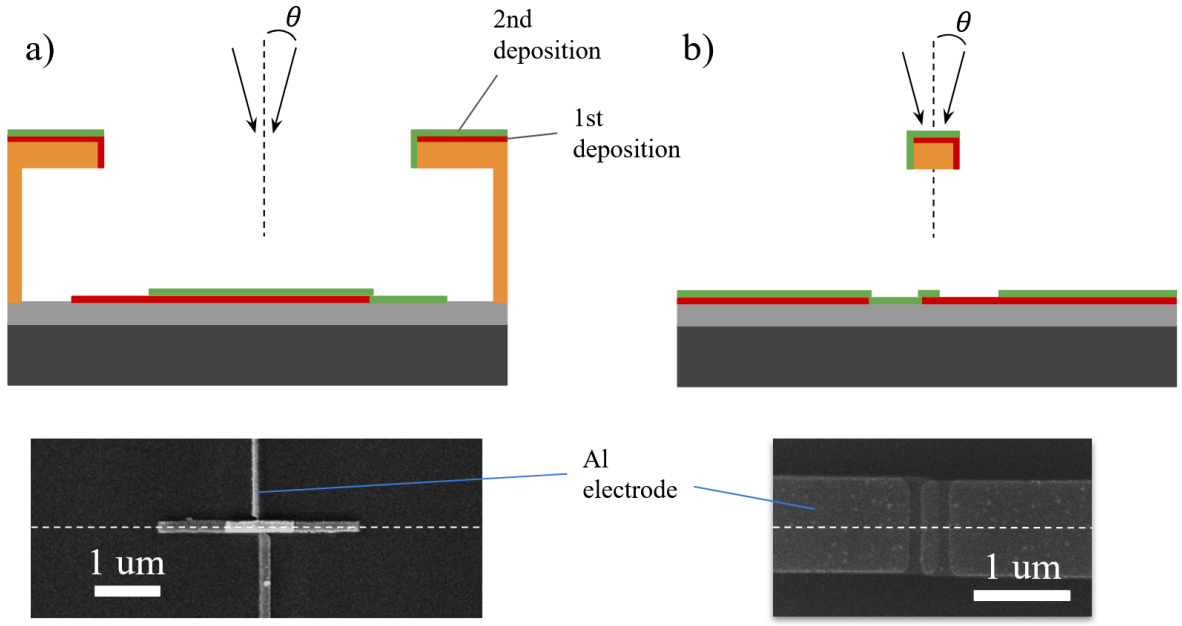

Figure 4.2: **Variations on the double-angle (θ) evaporation technique.** (a) Junction fabrication by shadow evaporation *without* a suspended bridge, dubbed "bridgeless" in the text, first published by Ref. [92]. SEM image shows a Al/AlO_x/Al JJ fabricated by Rigetti Computing. (b) Traditional shadow evaporation technique pioneered by Dolan [93]. SEM image shows Al/AlO_x/Al JJ fabricated by the author. White dotted lines indicate the cross section of the evaporation schematics.

several from Mesogroup and the plurality from Rigetti Computing.

The Rigetti junctions, which are our focus here, were configured in two ways. The junctions were either implemented in a "standalone" configuration or "transmon" configuration. In the former, leads extend in opposite directions by several *millimeters* before terminating in large area wirebonding pads. In the transmon, lithographically defined metallic edges of each superconducting electrodes form a shunt capacitance $C_s \sim 100$ fF estimated via electrostatic simulations prior to fabrication [38]. See Fig. 4.1 for images of these two JJ layouts.

The Rigetti junctions were lithographically fabricated without a suspended resist bridge. According to the purveyors of this "bridgeless" technique, the absence of bridges increases both the

mechanical robustness of the resist mask and the accessible range of junction areas in a double-angle deposition [92]. During fabrication, the width of the overlap area was fixed at 240 nm, and the length varied from 260 to 1510 nm yielding an effective junction area $A \approx 0.06 - 0.36\ \mu\text{m}^2$ depending on the resist mask. A diagram of the bridgeless lithography method is shown in Fig. 4.2(a).

The author opted to fabricate SIS junctions using the traditional suspended resist bridge technique [93] shown in Fig. 4.2(b). A lab-standard methyl methacrylate/poly methyl methacrylate (MMA/PMMA) resist bilayer was used as a mask to shadow-evaporate a $\pm 15^\circ$ double angle of Al in an electron-beam (e-beam) deposition system. An oxide layer was created between Al depositions by steadily streaming O_2 into the chamber while lightly pumping on one side. A pressure of ~ 100 mTorr was maintained for 10 min. Several junctions were deposited at once and the leads patterned parallel to one another with bridge widths between 50 and 200 nm. After metalization, junctions with similar area to the Rigetti junctions were selected for measurement. The Rigetti junction tunneling contacts had an average specific resistivity $\rho_c \sim 4.0 \times 10^{-5}\ \Omega\,\text{cm}^2$ compared to $\rho_c \sim 2.7 \times 10^{-5}\ \Omega\,\text{cm}^2$ for the home-made junctions. The difference was likely due to variation in tunnel barrier thickness.

4.2 Fabrication methods — SNS junctions

While there are many reports from this lab documenting the fabrication of proximity effect devices [86]–[91], given the passage of a generation of graduate students and the influx of new equipment, we detail an updated step-by-step procedure for the sake of posterity.

4.2.1 Substrates

Josephson junctions made from metal films are born on SiO_x substrate wafers. The wafers are cleaved into ~ 1 cm^2 squares, ultrasonically cleaned in distilled H_2O for 3 min, acetone for 3 min and isopropyl alcohol (IPA) for at least 1 min, and blow-dried with N_2 gas.

The bonding pads of each device must be sufficiently spaced to avoid cluttering the wirebonds yet sufficiently packed to reduce electron-beam lithography (EBL) writing time. The sweet spot for a device with 32 leads spans an area $\sim 2 \times 2$ mm^2. To maximize yield, devices are prepared in batches of 9 and diced into individual dies at the end of fabrication. Si wafers[1] with (100) crystal orientation and a relatively thick 1-μm oxide are chosen to mitigate the risk of punching through the SiO_x during wirebonding.

4.2.2 Die preparation

Photolithography is a common method for patterning large area leads (LAL). The author, however, prefers EBL to write all shapes, big and small, because EBL does not require out-of-house equipment and allows for on-the-fly changes to the pattern. Additionally, since the resist recipe is identical for all feature sizes, consistency reigns supreme. Instructions for exposing, developing and metalizing LAL are laid out thus.

1. Spin coat 6% copolymer MMA (8.5) MAA in ethyl lactate solution[2] on the sample for 60 s at 3,000 rpm for a thickness of $\sim$150 nm. The comparably high susceptibility of the MMA copolymer to scissioning creates an undercut that facilitates resist removal after metalization.

[1] From University Wafer, for instance

[2] This resist is purchased from Kayaku (along with PMMA) as a "copolymer" since the monomer methacrylic acid (MAA) is combined with MMA to form poly(methyl methacrylate-co-methacrylic acid). Despite this lab's DIY ethos, copolymerization is best left to the chemists.

2. Bake the sample(s) on a hot plate for 3 min at 130° C to evaporate the solvent or "soft-bake" the layer. Cover the sample(s) with an inverted glass Petri dish to promote convective heating. Uncovered samples will be under-baked.

3. Spin coat 4% PMMA in anisole solution on the sample for 60 s at 4,000 rpm for a thickness of ∼200 nm.

4. Bake the sample(s) on a hot plate for 3 min at 170° C covered with a Petri dish.

5. Expose large area patterns in a scanning electron microscope (SEM)[3]. EBL for large features with linewidths > 1 μm requires less precision than lithography for finer features. A guide for best results exposing large-scale features is enumerated below.

   (a) Clip the spin-coated substrate to an SEM stub mount. The mount surface must be as flush as possible against the substrate backing to minimize variability in the working distance (WD) across the entirety of the substrate surface.

   (b) Configure SEM parameter settings shown in Table 4.1. Standard column alignment procedure should be performed at a magnification of at least 50 kx on the Au-on-C test specimen.

   (c) With the beam set to single scan, scan speed minimized to 1 μs per pixel and field of view maximized on "Wide Field" mode, traverse the stage carousel to the sample and square the substrate corner using the "Alignment Tool." Squaring the chip will align the Si crystal axis along the row of devices, which will make the post-fabrication cleave feasible. Fast single scans on resist-coated SiO_x at low magnification will not significantly overdose the pattern.[4]

[3] Specifically, a 4th generation TESCAN MIRA Schottky-type field emission scanning electron microscope

[4] A scan at a speed of 1 μs/pixel with 1024×1024 pixel resolution completes in 1048576 μs. At the max field of

(d) Focus the beam on a dust particle towards the middle of the substrate. WD adjustment sensitivity is tied to the magnification; a scan window magnified at 500x allows finer control over the focus. If no dust particle is present, focus on the substrate edge.

(e) Center the LAL pattern at the squared corner of the substrate leaving about half a millimeter margin between what will be the edge of the LAL and the substrate edge. The square "Measurement Tool" may assist in mapping the area of the pattern to the corner without exposing. Draw a square with equal dimensions to the pattern. Center the square on the scan window. This is where the pattern will write.

(f) Expose the pattern. The author highly recommends writing a large shape at one corner which allows one to orient the pattern by eye after metalization. The write time for a typical LAL pattern containing 22 to 32 leads is 5-7 min. Include four 1-μm^2 alignment squares within about hundred microns of the center of the die. After exposing the pattern, one may single scan to ensure the pattern wrote as expected.

(g) Translate the stage a distance equal to the length of the pattern plus 1 mm using the stage movement controllers. Write the LAL pattern in a snaking fashion left to right at the top row, right to left in the middle row, and finally left to right at the the bottom for a total of 9 patterns.

6. Develop the exposed samples for 60 s in 3:1 methyl isobuthyl ketone (MIBK) to IPA warmed to 24-25° C. Place a mercury thermometer in beaker containing $\sim$ 20 mL of MIBK/IPA solution on a hotplate set to 40° C. When the thermometer reading exceeds 24° C, remove the beaker from the hotplate and randomly stir the samples in the solvent before spraying

view, the beam dwells on any 1 μm^2 area for roughly 1/8$^{\text{th}}$ of a microsecond. At a beam current of 10 nA, this dwell time translates to about 0.1 μC/cm^2 for 1 micron linewidths. Even considering backscattered electrons, there is little risk to overdosing LAL on single scan mode.

thoroughly with IPA and drying with N_2 gas.

7. Metalize the LAL with 5 nm of 99.99% Ti followed by 45 nm of 99.95% Au in Mesogroup's e-beam deposition system[5]. Before the Ti deposition, introduce ~ 40 mTorr of O_2 into the chamber and plasma etch the substrate surface for 25 s to remove residue left by resist processing.

8. Lift off metalized resist by soaking the sample in acetone for 5 min. Apply gentle ultrasonication as needed.

After liftoff, the author recommends immediately spinning a new MMA/PMMA bilayer on the sample. Resist acts as a protective coating from minor scratches that could cause discontinuities in the leads. Examine the completed LAL pattern for quality assurance before proceeding to fine-feature EBL.

4.2.3 Fine lead lithography

The following procedure details step-by-step how to reliably and efficiently write fine features between 60 and 1000 nm in linewidth. We assume SEM users have general knowledge of standard SEM alignment procedures. Calibrate coils from the top of the column downward by centering the gun, objective lens and stigmators, in that order. If major stigmation centering is required, objective centering must be performed again. Finely adjust stigmator coils last before writing.

1. Clip the substrate to an SEM stub mount. The more level the chip, the better. Use two clips if available.

2. Run the "Auto Gun centering" protocol which centers the electron gun automatically at the selected landing energy for all beam currents at once. Perform this protocol at minimum

[5]For a thorough discussion of e-beam deposition recipes and best practices for running the JoeTek, see Ref. [10]

Feature size	> 1 μm	< 1 μm
SiO_x thickness	1 μm	1 μm
Landing energy	30 keV	30 keV
Working distance	9.6 mm	< 5 mm
Magnification	95x	$2 - 10$kx
Field of view	~ 10 mm^2	~ 0.05 mm^2
Dosage	230 μC/cm^2	≥ 230 μC/cm^2
Nominal beam current	10 nA	10 pA
Write time	$5 - 7$ min	$3 - 120$ s

Table 4.1: EBL parameters for LAL (left column) and fine features (right column) written in the Tescan SEM with ElectronScribe software.

magnification on a large, flat surface, such as the stage carousel itself. Once completed, magnify the beam in a nearby Faraday cup where minimal electrons are deflected. Record the absorption current.[6]

3. Align the beam. Move to the Au-on-C test specimen and align the beam as well as possible at a beam current of 10 pA. The Au spheres should appear round and defined with no noticeable directional stretching.

4. Traverse to the sample on single scan, speed 3, Wide View mode. Center an LAL pattern directly under the column while minimizing the exposure to electrons. This is done by single scanning at low magnification, identifying the orientation of the pattern,[7] squaring the pattern

[6]This number may change by 10% depending on the day.
[7]Using the large lithographically defined shape in the corner as a landmark

using the alignment tool, and increasing magnification on one particular large area lead at a point far away from the sample center. Use this lead edge to focus the beam. A single scan at a time, trace the lead towards one of the four alignment rectangles.

5. Fine focus on the alignment rectangle. The "Analysis and Measurement" tool may be used as a single line scanner to focus the beam. Draw a line across the Ti/Au-metalized alignment rectangle and adjust the WD for the sharpest transition over the shape edge. After focusing, move the center of the sample directly under the beam with the stage controller while the beam is blanked. Wait 5 min for any directional drift associated with the stage stepper motors to settle.

6. Align the pattern using the ElectronScribe ("Escribe") program.[8] Center the LAL alignment rectangles under their corresponding shapes in Escribe. The pattern will already be roughly aligned after using the Tescan's alignment tool and stage controller. Escribe's built-in alignment tools allow fine pattern alignment without exposing critical areas of the sample to electrons. We will use this feature again aligning the Al layer to the Au layer.

7. Expose the Au pattern. There are a few principles to remember when designing patterns with fine features. First, to account for charging effects on the substrate,[9] the narrowest lines should be written first. This typically means ordering the shape list to prioritize the innermost shapes including the 4 fine *alignment markers* clustered around the smallest features. It is critical that these markers and the finest features are contained within the small field of view at 5-10kx magnification. Otherwise, it may be difficult to identify the alignment markers inside the exposure windows during Al alignment. Secondly, linewidths narrower than 150

[8] Written by Venkat Chandrasekhar
[9] Which may slightly deflect the beam, warping or underdosing the shapes

nm should be written at a higher dosage.[10] This prevents slight underdosing which, for very narrow linewidths, results in wire breaks. At 10 pA and a base dosage of 230 μC/cm^2, Escribe will complete a typical Au layer in $3 - 120$ s. See Table 4.1.

The pattern may be developed identically to the large area leads: 60 s in 3:1 MIBK:IPA warmed to 24° C, quickly rinsed in IPA and blow-dried with N_2. The purpose of the Au layer is to (a) couple the superconducting reservoirs and (b) electrically connect the LAL to fine normal leads needed to inject and drain quasiparticle current at particular points in the device. Exposure of the Al layer, which contains the superconducting leads, flux loops and field coils used to phase-bias the device, directly follows metalization of the Au layer. The Al layer procedure follows exactly steps (1-6). Step (7) is replaced by the following alignment procedure.

Align the Al layer to the Au pattern using the four Au alignment markers. Closely clustered markers enables alignment at high magnification which provides better resolution and ultimately more accurate alignment. Once the alignment markers are aligned within the exposure window, immediately expose the Al layer. In the case where Al shapes extend beyond the field of view, a separate Al layer is required. Align and write one layer whose shapes are all contained within the field of view, then write the other layer after lowering the magnification.[11]

On-chip superconducting field coils used to phase-bias the junctions are as large as the LAL. They must be written using parameters from the left column of Table 4.1 directly after writing the fine Al layer features.[12] To avoid self-heating effects when biasing the coils during measurement, these leads should be made of superconducting Al all the way to the wirebonding pads.

[10] Made possible by increasing the individual shape "rate" in Escribe

[11] Design extra overlap between shapes of different Al layers to account for any beam drift from switching magnification

[12] Changing the beam current between 10 nA and 10 pA seems not to adversely affect focus or stigmation at 10 pA

4.2.4 Metalization

The SNS junctions studied in this thesis are fabricated from 99.999% (5N) Au and 5N Al. One may pay a price to purchase such high-quality source materials from online vendors[13], though it is far from guaranteed that the metalized film will be of equal purity. Contaminants in the evaporation vacuum chamber, especially magnetic ones, tend to greatly reduce L_ϕ in mesoscopic Au wire. Therefore, to reliably deposit high-quality normal metal films required for micron-long SNS junctions, a dedicated thermal evaporation chamber whose sole purpose was to deposit 5N Au and Al was rebuilt by the author.[14] We include a detailed description of the electrical circuitry needed to operate the thermal evaporator and recipes for high-quality Au and Al depositions.

There are two distinct circuits that feed off building power: the low-voltage circuit responsible for controlling the evaporation rate and a high-voltage circuit designed to stabilize an etching plasma in the chamber. See Fig. 4.3 for a schematic.

For the low-voltage side, a 2-kVA power supply capable of driving 200 A ac is attached to a step-down transformer. The transformer output is connected to high-power magnet cables and the circuit is closed by the evaporation boat[15] whose resistance is typically several ohms. During an evaporation, the boat is Joule-heated by more than a hundred amps which melts any non-refectory metal placed inside. The current through the boat, and indirectly the temperature of the boat, is monitored with an inductive loop coupled to the power supply.

For the high-voltage circuit, building power enters a variable autotransformer (variac) whose winding ratio may be manually adjusted on the evaporator control panel. The output of the variac enters a step-up transformer whose ground is connected to the evaporator chassis. The live end of the step-up transformer routes through a high-power 300-kΩ resistor in series with the sample

[13] Such as ESPI Metals, where 5N Au shot will run $\$298.13$ per gram at the time of writing
[14] This was not the first rebuild by this group — original documentation is dated April, 1970
[15] Purchased from RD Mathis

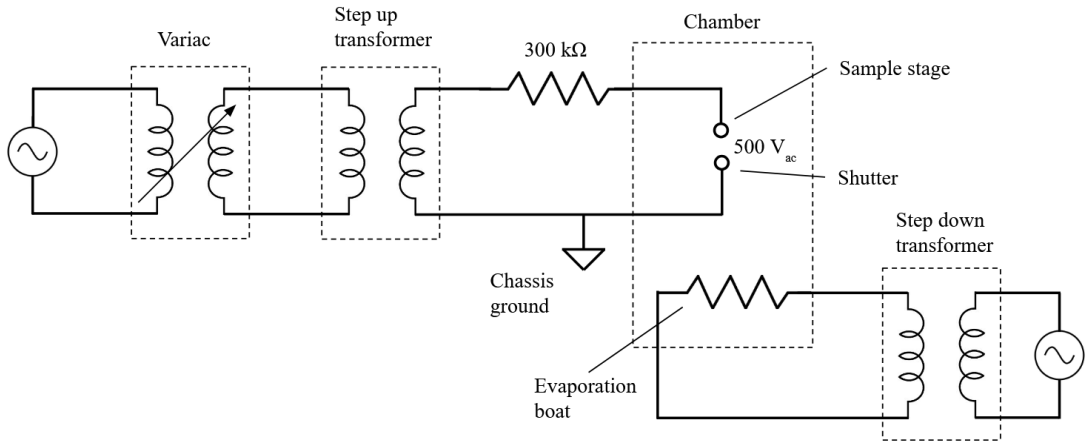

Figure 4.3: **Thermal evaporator electrical circuit.** Separate low-voltage and high-voltage circuits are explained in the text. Variac fixed at a particular winding ratio to apply 500 V_{ac} from sample stage to ground.

stage. During operation, a small amount of etch gas, typically O_2 or Ar, is introduced to the chamber. The etch gas is ionized by a potential difference of 500 V ac between the ground and the isolated sample stage. Positively charge ions are accelerate towards the sample, directionally etching the substrate in the case of Ar^+ or chemically reacting with the surface in the case of O^+. AC power is required to clean SiO_x since the wafer acts as capacitor in the plasma circuit. The purpose of the high-power resistor is to steady the current drawn from the plasma. Without the resistor, the current carried by the plasma may become unstable, resulting in inconsistent etch times.

4.2.4 Recipes — 5N Au

Au readily wets and alloys to refractory metals. Alumina-coated boats, which prevent wetting, are often recommended when evaporating Au. However, the author has found that using alumina-coated boats gives inconsistent deposition rates measured by a quartz crystal monitor. Evaporating Au from uncoated "dimple type" isolated hot zone Mo boats[16] yields more reliable results. The boat may be reused dozens of times if the temperature is ramped slowly — 5 min from room temperature to the melting point of Au.

A steady deposition rate at low pressure is desirable. With frequent use, after an overnight pumpdown and cold trap refill, the chamber pressure typically sits at $\sim 5 \times 10^{-7}$ Torr. For a standard film thickness of 50 nm, a rate of approximately 3.0 Å/s completes the deposition in under 3 min. It is important to avoid excess pressure buildup associated with outgassing caused by heat radiating from the boat.[17] Perform a 40-mTorr O^+ reactive ion etch for 30 s immediately prior to the deposition to clean the surface of the substrate.[18] "Predeposit" 5 nm of Au to ensure stability of the deposition rate. During the deposition, the pressure will ideally remain $< 2 \times 10^{-6}$ Torr.

Each evaporation uses about a tenth of a gram of source material, and the Mo boat must be refilled with Au after every use. Dedicated non-magnetic (austenitic) stainless steel tweezers should be the only tools used to handle objects introduced into the chamber. After removing the Au-coated sample from the chamber, soak the sample in slightly warmed acetone at 40° C to remove the resist. Spray the sample with acetone to encourage removal. All the resist and unwanted metal must be completely removed before allowing the sample to dry. Image the sample in the SEM to

[16] RD Mathis Part No. S8A-.010Mo

[17] The boat may be preheated for up to 30 min below the melting point of Au to encourage outgassing before the deposition

[18] Without an O^+ etch, fine Au wires will fail to adhere to the substrate

verify the quality of the metalized lithography.

4.2.4 Recipes — 5N Al

Molten Al is highly corrosive and will eat any metal it contacts. For this reason, we use relatively inexpensive W boats[19] to evaporate Al. Discard the boat along with any unevaporated Al after use.

We are relatively unconcerned by impurities affecting the critical temperature of our Al film, and we may evaporate Al films at any pressure $< 1 \times 10^{-5}$ Torr. While Al is amenable to a "rough and dirty" evaporation, caution should be taken to avoid high deposition rates > 6 Å/s which result in large grain sizes and difficulty during the liftoff process. We recommend a slow ramp and 10-nm predeposition for a stable rate. Clean the surface of the sample, including exposed Au interfaces, with a non-oxidizing Ar plasma for 80 s at 40 mTorr immediately prior to the Al deposition. Since an intermetallic alloy of Au and Al begins to form at ambient conditions, the completed device must be cooled within several hours to avoid degradation of the Au/Al interface. Upon opening the shutter, start a timer. Remove the sample, soak it in warmed acetone, rinse in IPA, blow-dry, and image in the SEM. Select the best-aligned device for cooldown. After cleaving the substrate to isolate the desired sample,[20] wirebonding may begin.

4.2.5 Wirebonding

Wirebonding involves welding metal wire[21] to a metal substrate[22] at room temperature. During operation, the bonding tool[23] is lowered to make contact with the bond surface; the downward force is ramped up to ensure intimate coupling between the bonding tool, the wire and the substrate;

[19] RD Mathis Part No. S3-.005W

[20] Spin a protective layer of unbaked resist on the sample to prevent scratching during this process. Lift off in a 1-min soak in acetone.

[21] Typically 0.001" diameter 1% Si/Al alloy superconducting wire from Ametek

[22] Either the Au/Ti large area leads or Au-plated header pins

[23] Deweyl Tool Co. Part No. CCSVE-1/16-750-45-C-2020-M

60-kHz ultrasonic power is applied for a specified amount of time to scrub surface contaminants and cause solid state diffusion. Upon retracting the tool, ultrasonic power ceases, force is relieved, and the tool returns to its rest position. Users control the ultrasonication power, duration of power and amount of downward force applied by the tool. These parameters must be adjusted for optimal performance depending on the material of the bonding substrate and exact height difference between the two substrate surfaces to be joined by the wire bonds.

Wirebonding is performed on a Hybond Model 572 wedge bonder. Calibrated to the right settings, and with adequate patience and precision from the user, the wirebonder may be used to bond a 32-pin sample in 5-10 min. Given the short time window imposes by the degrading interface of the Au/Al samples, efficient bonding sessions are highly desirable. Comprehensive sample preparation and clean room hygiene is paramount. We provide a wirebonder checklist to complete *before* depositing the Al film.[24]

1. Prepare the room. At the time of writing, the wirebonder is sequestered in back corner of FG39. Blackout curtains allow for a semi-private wirebonding experience. Close the curtains and turn on humidifiers to increase the moisture content in the room and mitigate electrostatic buildup that may discharge through the sample. Avoid wearing clothing items such as fleece or wool which tend to collect charge.[25]

2. Prepare the wirebonder. Turn the wirebonder on 10 min before bonding to warm the machine. Avoid building a potential difference between the bonding tool and the substrate by grounding (with a metal braid) the working stage to the wirebonder chassis and the chassis directly to building ground. To maximize control over the ultrasonic power applied to the substrate, the total length and height of the transducer arm are very important. The tip of

[24]One despairs no quicker than while struggling with the wirebonder during the final step of a week-long fabrication process

[25]The author wears 100% cotton on wirebonding and cooldown days

the bonding tool must extend exactly 0.59" from the set screw on the transducer arm and the lowest position of the tool tip must reach $0.02 - 0.03$" below the substrate surface.

3. Prepare the sample holder. Ultrasonicate the PCB header in IPA and blow dry with N_2 to remove dust from the metallic bonding pads. Mount the header in a metallic, thermally massive "puck"[26] to ground all pins. Ensure the surface of the header is level.

Once completing the checklist, adhere the sample to the PCB header with conductive silver paint[27] and leave to dry for 10 min.

Anecdotally, wires will bond successfully about 95% of the time within the appropriate parameter space. If the success rate is substantially lower, a systematic error may require troubleshooting. Common issues include: (1) debris buildup in the wedge tip[28], (2) insufficient ultrasonicate power delivered to substrate[29], and (3) wire breaking after bonding.[30]

Occasionally, the wire will break and must be rethreaded. Remove the tool from the transducer arm to rethread the wire through the tool shaft. Secure the tool back on the transducer arm to thread the wire through the tool pinhole. The pinhole opens at a $\sim 45^\circ$ angle. If one encounters much difficulty rethreading through the pinhole, the tool requires cleaning.

4.3 Measurement techniques

The measurement techniques used by this group have been refined over nearly three decades. Most of tools used here are discussed in detail in Ref. [88]. We emphasize certain techniques as they relate our experiments.

[26] A thin solid piece of copper wetted to the brass pins of a female PCB header with low-temperature solder

[27] Ted Pella, Inc. PELCO Prod. NO. 16062

[28] Ultrasonicate tools in five parts H_2O to one part NaOH and rinse with IPA to clean

[29] Check that the substrate surface is level and that the tool tip is positioned at the correct height

[30] Friction along the wire feedthrough must be reduced by adjusting the clamp or introducing some slack by slightly unraveling the spool

4.3.1 Cryogenics

The IV curves of SIS Josephson junctions were measured in an Oxford MX100 dilution refrigerator cryostat (the "MX100") with a base temperature of ~ 20 mK. The temperature of the fridge is inferred from a calibrated RuO_2 thermometer affixed to the mixing chamber base plate. The resistance of the thermometer is monitored by a "Femtopower" system installed by Oxford Instruments. A heat shield secured at the cold plate flange prevents 4-K blackbody photons from the vacuum can from radiating onto the mixing chamber. The MX100 is equipped with a solenoidal superconducting magnet capable of producing a 3-T field perpendicular to the sample plane and a split coil magnet capable of a 1-T in-plane field.

The cost of running a dilution refrigerator is tied to the cost of liquid He. To avoid transferring liquid He every other day[31], a He reliquifier installed by the author returns dewar boiloff and exhaust from the He-4 pump back to the He bath. Properly maintained, the reliquifer enables continuous measurement on the MX100 for months with no new additions of liquid He.

SNS devices were measured in the MX100 and a Janis He-3 cryostat (the "Janis"). The base temperature of the Janis is approximately 270 mK verified by a RuO_2 thermometer and an AVS bridge. Compared to the MX100, the He-3 system allows for more rapid cooldowns at the cost of a higher base temperature. Since, thanks to the reliqufiers, a He bath level could be maintained in both systems for months, the cryostats were frequently "hot swapped" by cooling a sample at room temperature to 4 K by lowering the inserts directly into the He bath. Hot swapping the Janis results in minimal He loss if lowered over the course of several hours, whereas losses are inevitable when hot swapping the considerably larger MX100.[32]

[31] The price of which exceeds $\$30$ per liter at the time of writing

[32] He losses may be mitigated by allowing He boiloff vapor to cool the inserts as much as possible

4.3.2 Measurement environment — SIS junctions

Low-frequency transport measurements on SIS junctions were performed using standard four-probe lock-in amplifier (LIA) techniques. Pairs of wires were bonded to either side of the junction, and the voltage V across the junction was measured as function of current I_{dc} biased across it. Current was applied using a custom current source with output impedance $Z_{\text{out}} \sim 10^{13}\ \Omega$. The high output impedance ensures the current source behaves as an ideal source even as the resistance of the JJ varies greatly from supercurrent to quasiparticle tunneling regimes. Alternative approaches to current biasing schemes often include simply biasing a large resistor in series with the sample. We avoid using such a psuedo-current source since this technique tends to draw a variable amount of current depending on the load from the junction. See Fig. 4.4 for an illustrative example of IV curves measured with different circuits.

The voltages across the junctions were measured using a custom voltage preamp with an input impedance $Z_{\text{in}} \sim 10^9\ \Omega$ or higher. The differential resistance dV/dI, which requires a small ac "tickle" or excitation current I_{ac}, was measured simultaneously with the voltage. Taylor expanding the voltage across the sample and considering only the first three terms we write

$$V(I_{\text{dc}} + I_{\text{ac}} \sin(2\pi f_{\text{LIA}} t)) \approx V(I_{\text{dc}}) + \left[\frac{dV}{dI}\right]_{I_{\text{dc}}} I_{\text{ac}} \sin(2\pi f_{\text{LIA}} t) + \frac{1}{2}\left[\frac{d^2V}{dI^2}\right]_{I_{\text{dc}}} (I_{\text{ac}} \sin(2\pi f_{\text{LIA}} t))^2 \tag{4.1}$$

where f_{LIA} is the output frequency of the LIA. We see that an ac current is required to pick out the dV/dI signal. Since I_{ac} is small, the third term is typically (but not always) ignored in standard lock-in measurements. We return to it, however, in our discussion of the feedback circuit at the end of this chapter.

A schematic of the measurement setup for SIS junction IV curves is shown in Fig. 4.5. Before

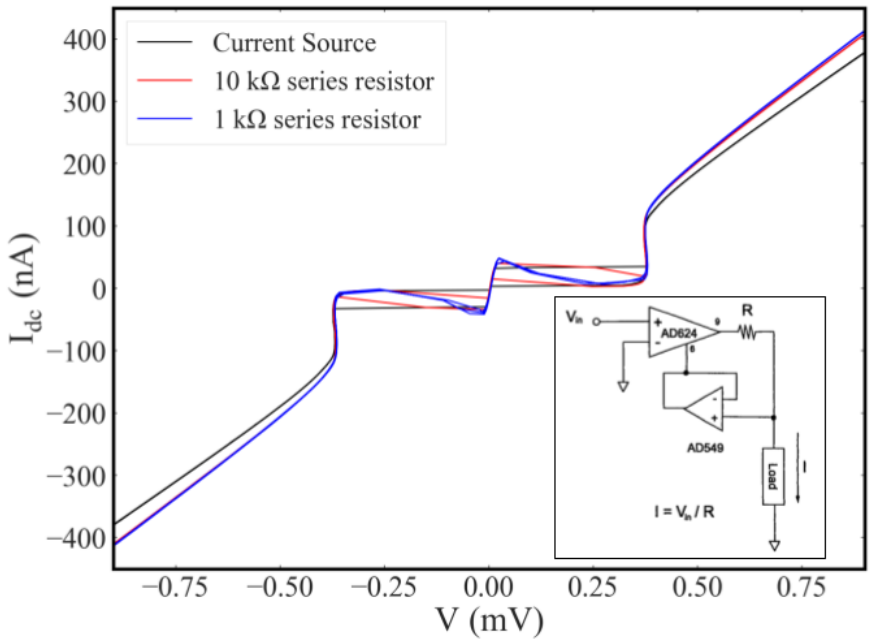

Figure 4.4: **IV curves measured with psuedo- vs ideal current source.** Non-ideal current sources cause distortions in the IV curve most prominent in the high-resistance subgap leakage current between the supercurrent and quasiparticle branches. Inset: circuit diagram from Ref. [88] of the current source incorporating an ultralow input bias current operational amplifier (AD549) used in this work.

entering the current source and sample, the LIA ac signal is combined with the dc signal in a unity-gain voltage summer. Very small excitation currents of about 25 pA were used to avoid washing out IV curve switching currents on the order of 1 nA. For the smallest junctions, this required implementing voltage dividers to reduce the output of the LIA below its lowest threshold.

The measurement leads on the MX100 are twisted pairs of superconducting NbTi wire in a CuNi matrix wrapped around a series of copper heat sinks at every stage in the dilution refrigerator. At the mixing chamber, the superconducting leads are swapped out for plain Cu wire to better thermalize the sample. No on-chip or low-temperature resistors were used to isolate the junctions from the measurement setup. This means that the impedance of all leads connected to junctions

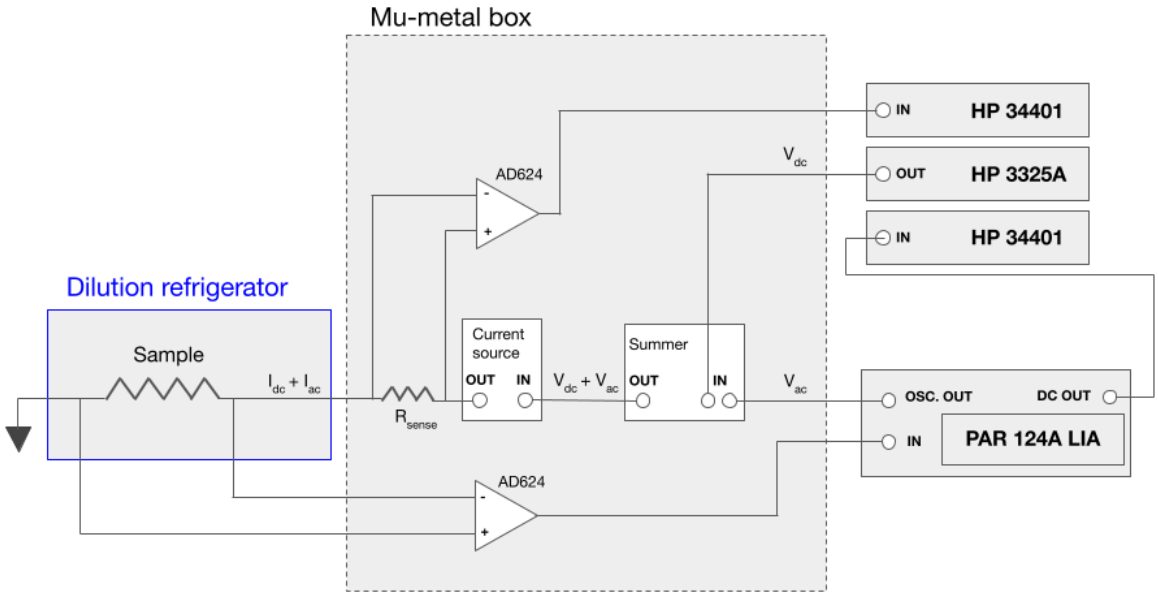

Figure 4.5: **Measurement setup for IV curves.** Custom-built summer, current source and AD624 voltage amplifiers housed in a μ-metal shield at room temperature. I_{dc} driven into the junction is measured by a sense resistor R_{sense}. Not pictured: voltage divider at the LIA output, measurement line filtering, and a room temperature 5-kΩ resistor placed between the sample and ground.

were less than $Z_0 = 377\ \Omega$ and no offset voltages due to the Coulomb blockade effect were expected in the IV curves.

Unlike for superconducting qubit readout, great care is taken in dc transport to filter out rf and microwave frequencies from coupling to the device. In addition to the native LC low-pass filter created from the distributed capacitance and discrete inductances of the wiring inside the fridge, the measurement lines were also low-pass filtered at room temperature with commercial Pi filters with cutoff frequencies at 800 kHz.

Unwanted noise is always a concern in sensitive transport measurements. If sufficient line frequency noise couples to a resistive sample, for instance, fluctuating currents may increase the

electronic temperature of the device, resulting in spurious temperature readings from the mixing chamber thermometer. As discussed in Chapter 2, elevated electronic temperature manifests most clearly in the quasiparticle branch of a SIS junction IV curve. Figure 4.6 shows two such IV curves: one measured in the presence of ground loops which act as inductive pick up coils for noise coming from the lab space, and one measured without ground loops.

Great effort was put forth to mitigate excess noise and minimize the thermal energy $E_T = k_b T$ contribution to junction phase dynamics. Prior to every measurement, an FFT spectrum analyzer was used to verify a flat background of < 6 $\text{nV}_{\text{rms}}/\sqrt{\text{Hz}}$ as guaranteed from the output of the first stage amplifiers. While not every curve displayed negative differential resistance, data suspected of noise contamination were excluded from analysis, including any IV curve with a visually rounded quasiparticle branch. Occasionally this meant discarding IV curves measured on busy weekdays where high-power machines elsewhere in the building dumped noise into our measurement rack. Persistent 60-Hz line frequency peaks on the spectrum analyzer indicated risk of elevated electronic temperature. In the temperature-sensitive experiments to come, we first confirm an adequate noise floor with our spectrum analyzer, and, when available, we use the quasiparticle branch as a electronic temperature indicator.

4.3.3 Measurement techniques — SNS junctions

Differential resistance dV/dI is the primary type data collected on SNS junctions. Without a tunneling resistance, R_N of SNS JJs are small — on the order of a few ohms. With such low-impedance samples, an audio transformer is used to enhance the signal-to-noise ratio of the measurement. These particular transformers act as step-ups to amplify the signal from the sample by a factor of about 10.[33] Transformers are fully ac-coupled and cannot be used to measure the dc

[33] See Ref. [87] for more information on measurement transformers

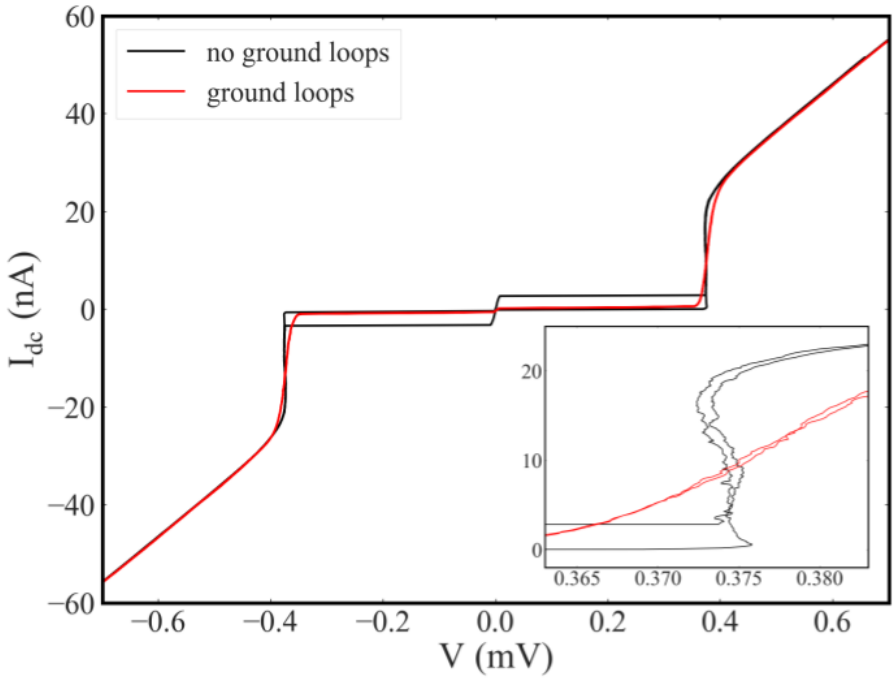

Figure 4.6: **Rounded IV curve from elevated electronic temperature.** Ground loops in the measurement setup couple to environmental noise which may increase the electronic temperature of the sample. Retraceable negative differential resistance (black curves) in the quasiparticle branch of width ~ 2 μeV corresponds to a thermal energy of 23 mK. These IV features are washed out in the presence of ground loops which elevate temperature (red curves).

voltage across the junction. Therefore, the "IV curves" of SNS junctions are typically shown as dV/dI vs I_{dc}.

To supplement the current source, a home-built Adler-Jackson bridge is occasionally used to measure the resistances of SNS junctions. The bridge offers the advantage of convenience, since it does not require external power to operate. The decade balance resistors on the bridge afford rapid diagnostic measurements at room temperature, allowing someone tight on time to quickly verify the viability of a particular device. Four 1-MΩ resistors in the bridge convert the LIA ac voltage signal into a current to drive the sample. With proper phasing,[34] the bridge may be used to measure

[34]Ensuring the out-of-phase component of the signal does not change with balance resistance

mΩ changes in resistance thanks to the stability of the source resistors and isolation transformer on the input.

In some cases, a feedback circuit is used to lock the measurement to a particular transition in the IV curve. The idea is to track the dependence of this transition as a function of external parameters, such as magnetic field or current bias. A home-built analog PID controller [88], [94] is deployed for such a purpose on a four-terminal JJ discussed in Chapter 6. In brief, the second derivative of voltage d^2V/dI^2 is measured by sending the $2f_{\text{LIA}}$ signal to the input of the PID.[35] With PID settings appropriately tuned, the PID output is fed back into the current source to compensate for small shifts in the IV transition due to external parameters. The PID output is plotted as a function of these parameters.

4.3.4 SNS junction characterization

To observe a Josephson effect in long SNS junctions, the junction length L must be much shorter than the Thouless length L_{Th} and normal electron coherence length L_ϕ. L_{Th} may be estimated at room temperature while L_ϕ is found by fitting to the magnetoresistance of a long Au wire. We discuss these methods below.

From Eq. (3.2), the diffusion coefficient D is needed to calculate L_{Th}. D is determined by l through $D = v_F\, l/d$ where d is the dimension of the sample with respect to $1/k_F$. Therefore, in wires ~ 50 nm thick and at most ~ 100 nm wide studied here, $d = 3$, and we require only an estimate for l to calculate L_{Th} at any particular temperature. l is inversely proportional to the resistivity ρ of an ideal metal. For Au, the proportionality constant is $\rho\, l = 8.45\times10^{-12}\ \Omega\,\text{cm}^2$ [95]. The resistivity of a wire with known dimensions may be accurately measured at room temperature through

[35] Utilizing trig identities to expand the 3rd term in Eq. (4.1), one needs the $2f_{\text{LIA}}$ amplitude to measure d^2V/dI^2

$$\rho = R_s t = R\frac{w}{L}t \tag{4.2}$$

where the width w of the Au wire is found through SEM-imaging or, more precisely, by fitting low-temperature magnetoresistance data. The wire thickness t is determined in the metalization step by a quartz crystal monitor. For a precise estimate of the sheet resistance R_s, it is best practice to measure the resistance R of a long 1D Au wire. This is achieved by co-evaporating an Au *meandering line* with $L > 200$ μm alongside the SNS junction. See an example of such a wire in Fig. 4.7. Here, the resistance of a meandering wire 220 μm long, 90 nm wide and 50 nm thick is measured to be 875 Ω resulting in a sheet resistance $R_s = 0.36$ Ω. Therefore, $l = 47$ nm, $D = 219$ cm^2/s, and $L_{\text{Th}} = 0.41/\sqrt{T}$ μm$\sqrt{\text{K}}$ which evaluates to $L_{\text{Th}} = 2.90$ μm at $T = 20$ mK.

The meandering line is also used to estimate L_ϕ. The processes that contribute to a finite value of the phase coherence length l_ϕ include electron-electron scattering, electron-phonon scattering, spin-orbit scattering and scattering by magnetic impurities in the metal. Self-interference of quasiparticles scattering off impurities in the normal metal results in weak localization corrections to the resistance [42]. One may destroy the coherent properties of these quasiparticles with an applied magnetic field. Therefore, the low-field magnetoresistance of a pure Au wire of known dimensions provides insight into the strength of weak-localization and by extension the phase coherence length of the wire. Figure 4.7 shows magnetoresistance data of a Au meandering line fitted to weak localization theory provided in Ref. [94]. From the fitting, both L_ϕ and the wire width w may be estimated.

The introduction of magnetic impurities destroys the coherence effects and severely limits L_ϕ. This was the main reason for rebuilding a dedicated thermal evaporator for high-purity Au. However, as seen from the figure, reasonably high-L_ϕ Au is also possible through e-beam deposition — as long as the system has not been recently used to deposit magnetic material.

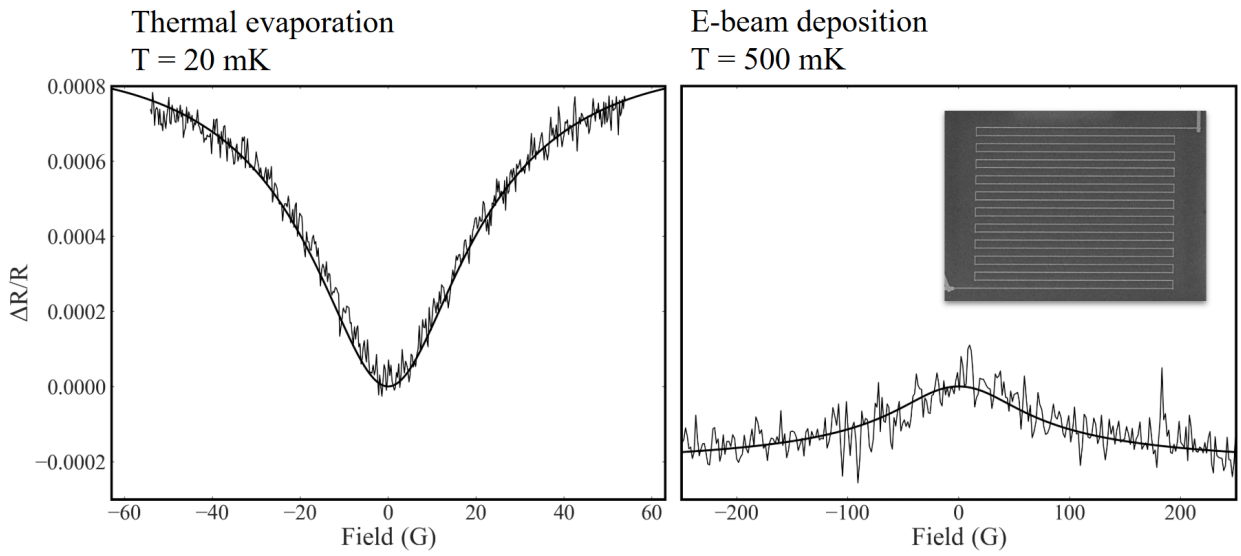

Figure 4.7: **Weak (anti-)localization fit to magnetoresistance of Au wire.** Change in resistance $R(B)$ normalized to the zero-field resistance $R(B = 0)$ of a long meandering wire (inset). Resistive corrections due to phase-coherent weak localization broken with an external field B. Side-by-side plots show Au deposited using thermal evaporator vs *freshly cleaned* e-beam deposition system. Fitting parameters include l_ϕ, l_{so} and w of the meandering wire. At 20 mK, $l_{\text{so}} \ll l_\phi$ and $R(B = 0) < R(B)$. At 500 mK, $l_{\text{so}} > l_\phi$ and $R(B = 0) > R(B)$. Best fit lines yield $l_\phi = 7.5$ μm for Au deposited in the thermal evaporator and $l_\phi = 2.0$ μm for Au deposited in the e-beam deposition system at their respective measurement temperatures.

In the experiments on SNS devices to follow, the length of normal metal between Al superconductors is $L < L_{\text{Th}} < L_\phi$. All devices were cooled down to cryogenic temperatures within 4-5 hours of depositing Al onto Au. This ensured SNS junctions remained fully Josephson-coupled at a range of temperatures and magnetic fields. Similarly to the case of SIS junctions, measurement-contaminating noise was mitigated before every experiment. In this chapter, we hope to have conveyed the importance of *preparation* before running an experiment. Liquid He is an expensive resource, and it is our responsibility to give ourselves the best chance to take useful data during a cooldown.

CHAPTER 5
EXPERIMENTAL RESULTS: SIS JUNCTIONS

Over the course of three years, from 2021 to 2024, the MX100 was cooled down a dozen times loaded with SIS JJs from a variety of institutions. Among the several dozen devices wirebonded, mounted and cooled, 25 junctions survived handling long enough to display low-noise IV curves worth analyzing. We select a handful of these curves to discuss in this chapter.

We present data pedagogically beginning with the important features of a small junction IV curve at 20 mK. We then show what happens to the IV curve when one experimentally modifies the thermal energy E_T and Josephson energy E_J of the junction. Next, we analyze junction defects by appending the device with a lithographically defined gate electrode. We end our discussion with our main finding: the surprising presence of small-junction IV features, namely the zero-bias resistance R_0 and reduced switching current I_{sw}, in junctions shunted by a large capacitor. To support our findings, we introduce numerical simulations using the WKB method in a tilted washboard model performed by V. Chandrasekhar.

5.1 Standalone junction IV curves

Let us review what we expect to observe in an IV curve of a small junction. Given the small intrinsic junction capacitance, fluctuations of the phase particle will result in (a) a switching process out of the supercurrent branch at a current $I_{\text{sw}} \ll I_c$ and (b) a voltage in the supercurrent branch associated with diffusion of the phase over time. We report both of these features in the following transport data.

Figure 5.1 shows an IV curve of an SIS junction at 20 mK measured by the author. The junction

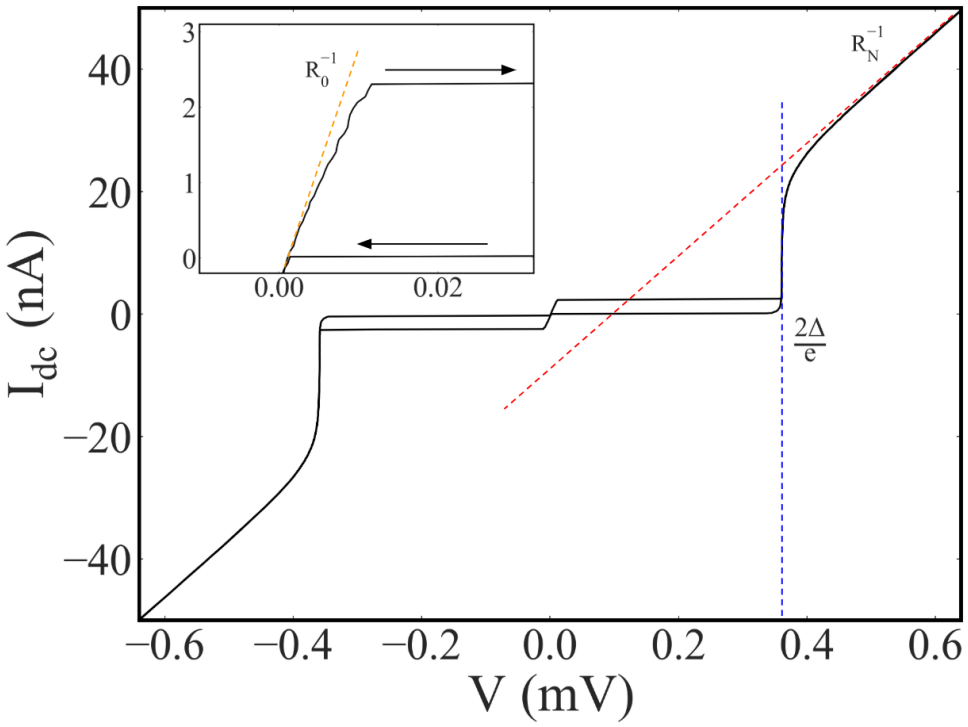

Figure 5.1: **IV curve of Rigetti Josephson junction.** Red dotted line marks $R_N = 11.40$ kΩ at high bias. Blue dotted line indicates $\Delta = 180$ μeV from the onset of the quasiparticle tunneling branch. The predicted critical current is $I_c = 24.8$ nA. The switching current is $I_{\text{sw}} \approx 3$ nA magnified in the inset. Yellow dotted line tangent to the IV slope at $I_{\text{dc}} = 0$ represents low-voltage phase diffusion. Arrows indicate direction of current sweep showing clear hysteresis. Figure adapted from Ref. [38].

was fabricated by Rigetti Computing using the bridgeless lithography technique discussed in §4.1. Since $E_J \sim E_C$, the junction is considered small as defined in Chapter 2. E_C is approximated from the parallel-plate capacitance model assuming $d \sim 1.5$ nm between Al electrodes. Using the formula $C = \epsilon A/d$, an overlap area $A = 240 \times 1,400$ nm^2, and an absolute dielectric constant $\epsilon \sim 90 \times 10^{-12}$ F/m for AlO_x, the intrinsic capacitance for the junction measured in Fig. 5.1 is $\sim$ 20 fF. Therefore, roughly, $E_C = e^2/2C \approx 4$ μeV, or, in terms of temperature (frequency), $E_C \approx 50$ mK ($\sim$1 GHz).

The Josephson energy E_J is calculated from the gap Δ and normal state resistance R_N measured directly from the IV curve. The dotted red line in Fig. 5.1 denotes the quasiparticle tunneling resistance. Since in this case the sample leads are superconducting and their resistances negligible, R_N measured with four probes at low temperatures provides a more accurate value of the tunneling resistance compared to a similar measurement at room temperature. Upon extrapolating the high bias slope downward, one notices a curious voltage offset where the red dotted line intersects zero current at ~ 0.1 mV. While one may naively attribute this offset to a capacitive charging voltage $V_{\text{offset}} = e/2C$, we now understand this feature to be a vestige of superconducting correlations in the quasiparticle branch. This fact is verified by applying a magnetic field discussed in the next section.

The onset of the quasiparticle branch occurs at the superconducting gap 2Δ marked by the dotted blue line in Fig. 5.1. In this Al junction, the quasiparticle branch becomes purely vertical at 0.360 mV resulting in an experimentally measured $\Delta = 180$ μeV. With R_N and Δ, one calculates the expected critical current to be $I_c = 24.8$ nA using the Amegoakar-Baratoff relation assuming $\Delta \gg k_b T$. From the figure inset, one immediately notices the measured switching current I_{sw} is much smaller than I_c. The order of magnitude discrepancy between I_c and I_{sw} agrees with trends reported in §2.3.2 where, for junctions with small capacitance C, the corresponding small mass of the phase particle is susceptible to fluctuations within the washboard potential. In underdamped junctions, if after fluctuating by 2π the particle retains enough energy to continue into a running state, a premature switch at $I_{\text{sw}} < I_c$ into the finite voltage is reported. Since the switching process is stochastic, for a given current bias, the switch will occur more frequently as the thermal energy approaches E_J, the barrier height. In this particular junction, $E_J = \hbar I_c/2e \approx 51$ μeV or 593 mK (12.3 GHz) and at 20 mK, $E_T = 1.7$ μeV. We examine the full temperature dependence of the IV curve in the next section.

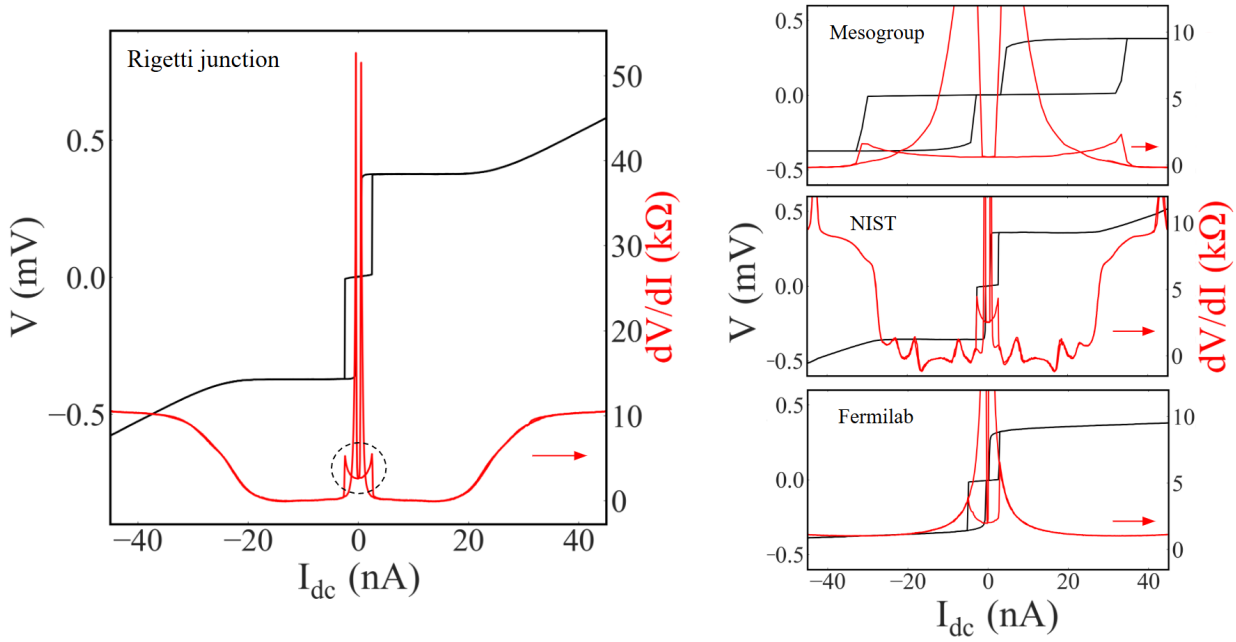

Figure 5.2: **Medley of standalone junction IV curves.** dV/dI peaks correspond to subgap leakage current. Peak magnitude is highly dependent on data sampling rate and averaging times. Dotted black circle denotes phase diffusion resistance. Rigetti junction has $R_N = 11.62$ kΩ, $R_0 = 2.23$ kΩ and $I_{\rm sw}/I_c \approx 0.1$. Mesogroup junction fabricated by the author has $R_N = 6.11$ kΩ, $R_0 = 0.60$ kΩ and $I_{\rm sw}/I_c \approx 0.5$. NIST junction has $R_N = 9.56$ kΩ, $R_0 = 2.53$ kΩ and $I_{\rm sw}/I_c \approx 0.1$. Fermilab junction has $R_N = 4.52$ kΩ, $R_0 = 1.98$ kΩ and $I_{\rm sw}/I_c < 0.1$ and was likely unintentionally measured in the presence of an small magnetic field.

Low-voltage phase diffusion associated with resistance R_0 in the supercurrent branch is also evident from Fig. 5.1. A yellow dotted line representing R_0^{-1}, the slope of the IV curve at the origin, is drawn in the figure inset. As the current bias $I_{\rm dc}$ increases, the slope decreases slightly, suggesting a nonlinear relationship between current and the phase diffusion resistance. As discussed in §2.4, the coexistence of the low-voltage state in the supercurrent branch and the high-voltage state in the quasiparticle branch implies the presence of frequency-dependent damping. Using the quantum Langevin equation, the environmental admittance $Y(\omega)$ may be used to model the exact nonlinear dependence of the phase diffusion on current, as we shall see momentarily.

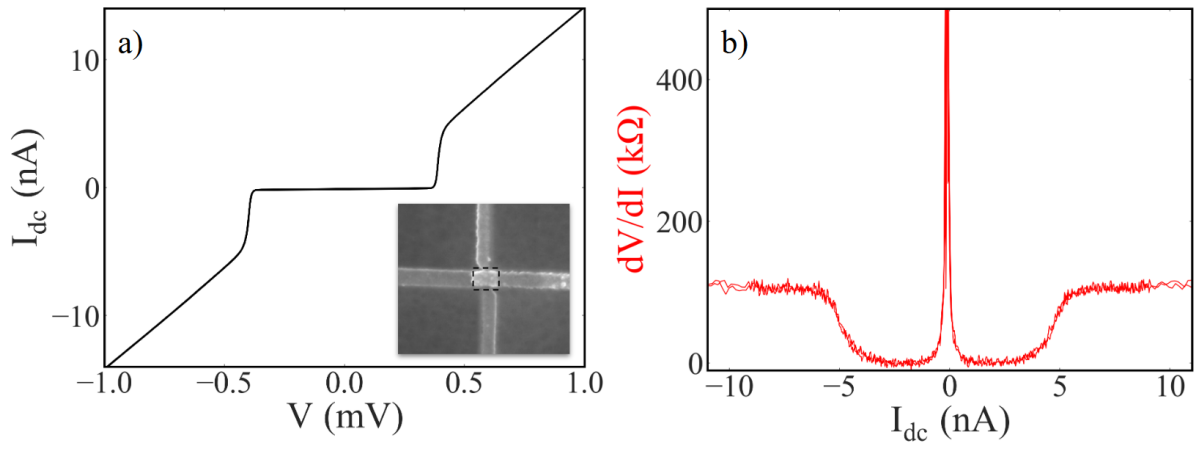

Figure 5.3: **Transport data of a very small junction.** (a) IV curve of a Rigetti junction with $R_N \sim 100$ kΩ at 20 mK. Note the absence of a supercurrent branch. Slight rounding in the quasiparticle branch indicates elevated electron temperature. Inset: SEM image with junction area marked by black dotted box with dimensions 270×240 nm^2. (b) Simultaneously measured dV/dI with $I_{ac} \approx 2$ pA. E_J is 6 μeV (14 mK) and I_c is 2.9 nA.

To emphasize the ubiquity of suppressed switching current and phase diffusion, we present IV curves measured on a medley of small junctions in Fig. 5.2. Here, the voltage and current axes have been swapped, and the differential resistance dV/dI measured simultaneously with the voltage V is plotted on the common current x-axis. The key feature of dV/dI is the nonlinearity in the phase diffusion regime where $I_{dc} < I_{sw}$, circled by a dotted black line in the left panel of Fig. 5.2. The local minimum at $I = 0$, which we define as R_0, is an appreciable fraction of R_N in every junction measured. Additionally, while $I_{sw} < I_c$ in every junction, the difference between I_{sw} and I_c is smaller in junctions with smaller R_N. This trend is expected since a small R_N corresponds to a large potential barrier height which decreases the probability of switching event.

For completeness, we include an IV curve of a *very* small junction in Fig. 5.3. Here, the junction area is $A \sim 0.06$ μm^2 and $R_N = 101.0$ kΩ. With high sample impedance, self-heating becomes an issue even with sub-nA excitation currents. In the measurement, one must strike a

balance between a large enough I_{ac} to observe subtle features in the dV/dI, yet small enough to avoid heating the sample, which would round the quasiparticle branch and wash out the switching current. Since I_{sw} has a power law dependence on E_J, one is unlikely to observe a well-defined supercurrent branch in very small junctions with very small E_J [29]. Large fluctuations of the phase particle prevent it from trapping, and a low-voltage diffusion state is not stable. In the very small junctions with $R_N \sim 100$ kΩ measured for this thesis, no supercurrent branch was observed in the IV curve.

5.2 IV curve dependence on temperature and magnetic field

Let us now intentionally modify the characteristics of small-junction IV curves. Consider first the effect of elevated electronic temperature. Figure 5.4(a) shows a series of IV curves at increments of power applied to the mixing chamber heater. Broadening of the quasiparticle tunneling current becomes obvious at around 500 mK. Here, quasiparticles are readily excited into available states in the superconducting counter-electrode before eV exceeds Δ. For temperatures in which the thermal energy $E_T > E_J = 65$ μeV (or 756 mK) in this particular junction, a distinct switching current is no longer observed. Instead, as seen in the figure inset for $T = 800$ mK and 912 mK, the phase diffusion resistance gradually transitions to a higher voltage state, effectively washing out I_{sw}.

More interesting is the saturation of R_0 at low temperatures shown in Fig. 5.4(b). The data suggest a temperature-independent mechanism for phase diffusion at $T < 100$ mK, although we note that log plots may overemphasize trends at low temperature [30]. Nonetheless, the temperature trend in R_0 serves to motivate upcoming WKB analysis in which the phase diffuses predominately via tunneling [96].

Another way to alter the features of an IV curve is with a magnetic field B. The critical

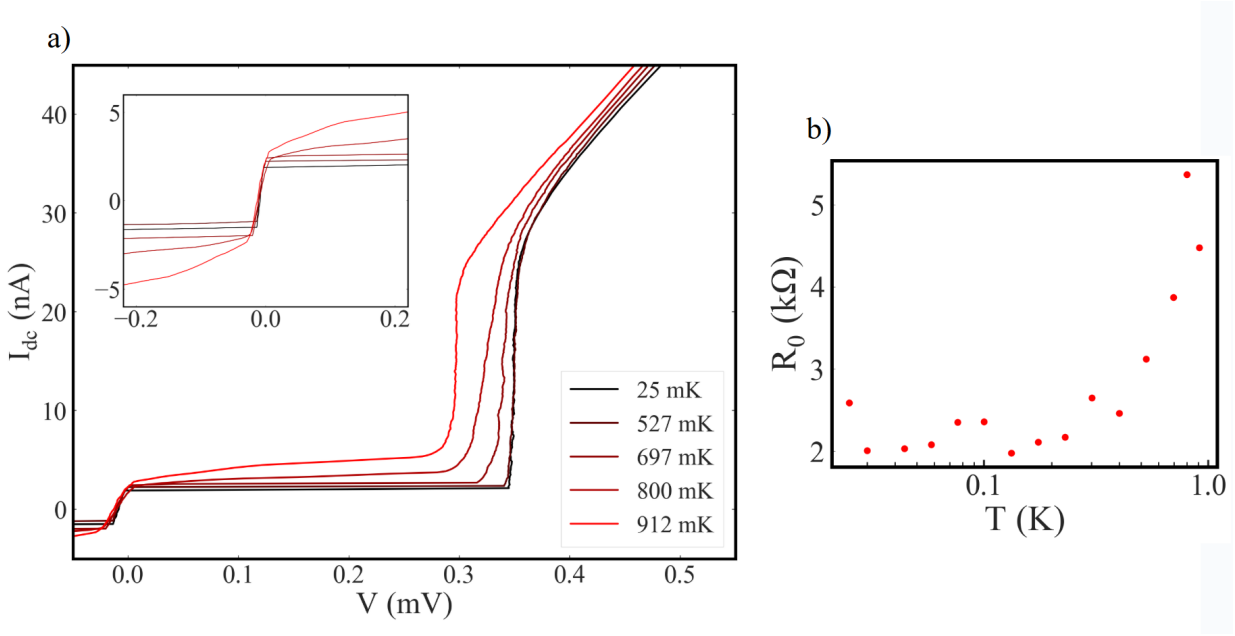

Figure 5.4: **Temperature dependence of an IV curve.** (a) Quasiparticle branch measured at $E_T \sim E_J$. Inset: Supercurrent branch and lack of switching current at $E_T > E_J$. (b) R_0 vs T plotted on a log temperature axis.

current I_c depends on the strength of correlations in the superconducting condensate. A sufficiently strong magnetic field acts as a Cooper-pair-breaking mechanism, reducing the superconducting charge density and lowering I_c. Figure 5.5 shows a series of IV curves in the presence of external fields of various strengths. With a completely suppressed gap, the SIS junction becomes a normal tunnel junction with an associated voltage-independent resistance R_N, shown with the black line at $B = 500$ G in the figure inset.

From the uniform linearity of this slope through zero bias, we may remark on the electromagnetic environment in which this junction is measured. It is well-known that in small-capacitance tunnel junctions, a charge tunneling from one electrode must overcome the repulsion force created by the voltage "build-up" on the other electrode. This Coulomb blockade effect (CBE) occurs only in small junctions connected to high-impedance bias circuitry. The lead resistance R_{leads} slows

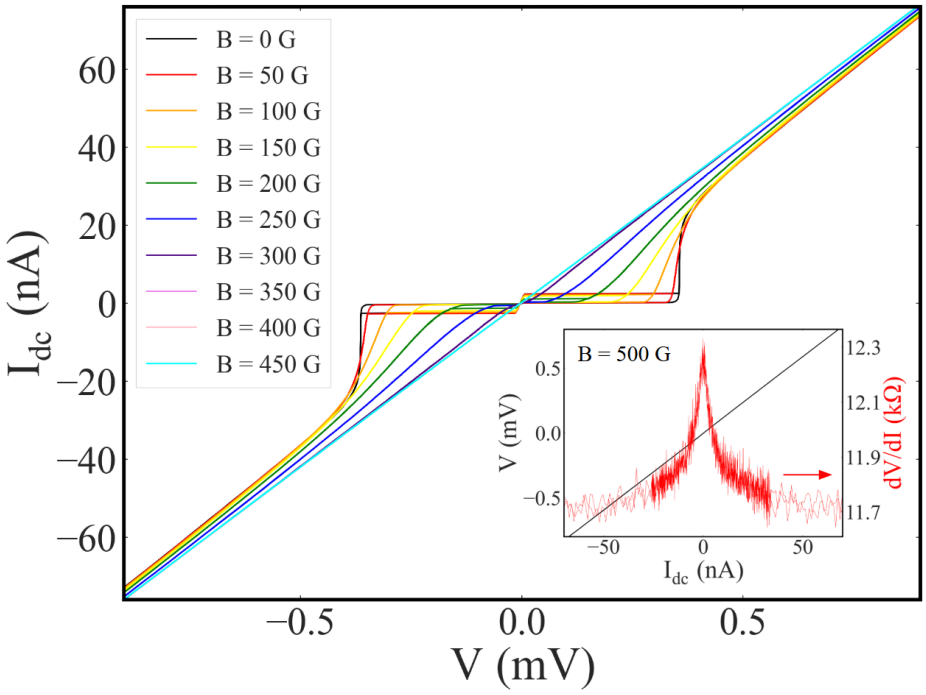

Figure 5.5: **Field dependence of an IV curve.** Onset of quasiparticle branch occurs at smaller voltages highlighting $\Delta(B)$ and thus $E_J(B)$. Inset: Zero-bias dV/dI peak at high field demonstrating the dynamic CBE.

electron escape long enough to impede the transport of other electrons via Coulomb repulsion. Here, since $R_{\text{leads}} \sim Z_0 \ll R_Q$, a Coulomb blockade offset voltage, known as the "Coulomb gap," is *not* observed in the IV curve. The application of a strong magnetic field removes the *apparent* Coulomb gap in the zero field data (Fig. 5.1). This suggests the voltage offset is due not to environmental impedance but to lingering superconducting correlations which slightly modify the IV slope angle at $I_{\text{dc}} \gg I_c$.

While the conventional CBE is absent in our measurement at high field, one may still detect a *dynamic* CBE in the dV/dI as shown in the inset of Fig. 5.5. Generally speaking, a dynamic blockade results from the RC time constant and ratio R_{leads}/R_Q of the circuit in which the junction is embedded [97]. The slower the electron escapes after tunneling, the larger the effect this "elec-

tron traffic" will have on the tunneling conductance. Here, one observes a roughly 5% reduction in the conductance as $I \to 0$. One would expect a more exaggerated dV/dI peak for junctions attached to measurement lines with higher R_{leads}, such as the cold isolation resistors used in previous experiments [14].

5.3 Junction defects

SIS junction cooldowns were performed for the Superconducting Quantum Materials and Sensing (SQMS) Center whose stated mission is to "bring dramatic performance improvement" to superconducting qubit coherence times. Among the various ways to decrease the impact of quantum decoherence, understanding limitations of the qubit hardware is this lab's focus. The goal is to eliminate materials-level sources of energy loss due to quasiparticle pair-breaking mechanisms or two-level systems residing in the junction oxide. At the Center's disposal is an arsenal of various measurement tools including scanning/transmission electron microscopy (S/TEM), atomic force microscopy (AFM), time-of-flight secondary ion mass spectrometry (ToF-SIMS), and non-destructive terahertz spectroscopy [98]. For members of SQMS utilizing dc transport techniques, we investigate fabrication defects of qubit JJs by analyzing specific features of the IV curve.

To this end, Rigetti junctions destined for use in operational transmons underwent additional levels of scrutiny with post-fabrication lithographic modifications. A normal metal Au electrode, shown in Fig. 5.6(a), was deposited within 100 nm of the junction to probe the charging response of potential defects. By oscillating the lateral gate voltage V_g at a frequency much less than the slew rate dI_{dc}/dt, the IV curve developed certain characteristics attributed to isolated superconducting *islands* in the device. Figure 5.6(a) shows the quasiparticle branch measured at increasing gate voltage amplitudes. Informed by TEM imaging performed on similar Rigetti junctions, we interpret our findings in the context of an array of small-capacitance tunnel junctions following

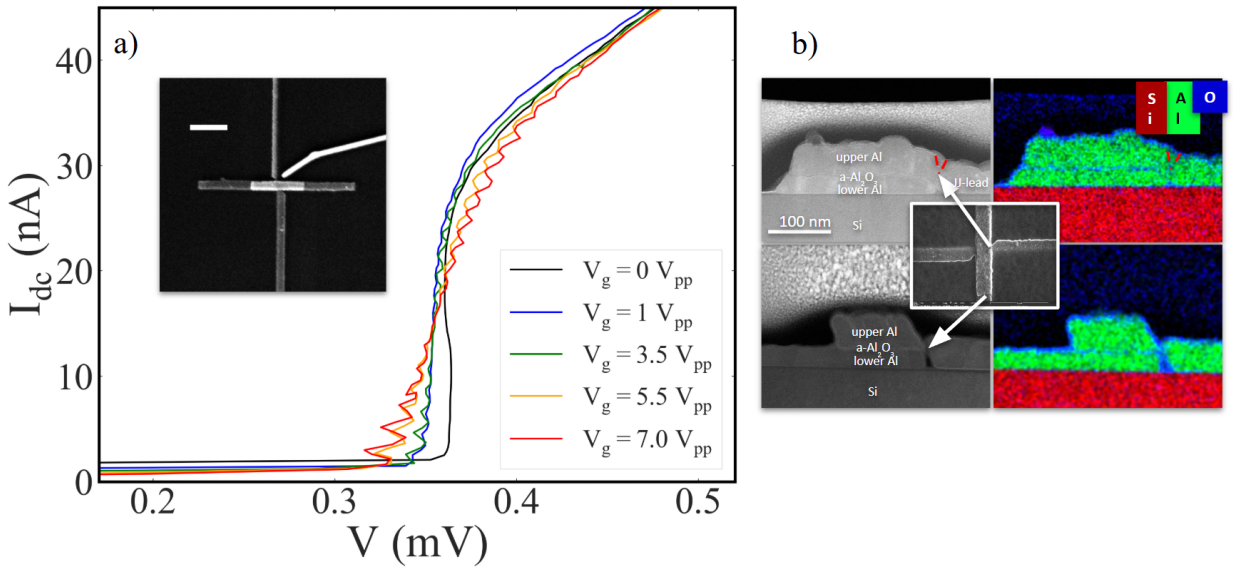

Figure 5.6: **IV curve of laterally gated *bridgeless* SIS junction.** (a) Quasiparticle branch biased at $dI_{\rm dc}/dt = 0.04$ nA/s in the presence of 12-mHz V_g. Inset: SEM image of the lateral Au gate electrode fabricated after the junction. Scale bar is 1 μm. (b) TEM images of Rigetti junction fabricated without a resist bridge. Upper row shows cross-section in the plane of the junction along the path of bias current. Lower row shows cross-section perpendicular to the junction. Colorized material compositions suggest the presence of an oxide barrier isolating a segment of the top Al electrode. TEM images credit to Lin Zhou at Ames Laboratory.

Ref. [99].

The assumption is that Cooper pairs traverse the junction by "hopping" to available states in superconducting segments of the junction isolated from one another by tunnel barriers. For the junction shown in Fig. 5.6, the particular segment in question dangles off to the side of the junction. See Fig. 5.6(b). The applied V_g induces an oscillating charge on the island. Depending on the sign of the charge, electrons transported across the junction require more or less energy to overcome Coulomb forces. This response manifests as periodic modulations of quasiparticle tunneling voltage shown in Fig. 5.6(a). One notices a thermal broadening effect at large V_g due to ac currents heating the sample.

The impact of this superconducting island on qubit coherence times is unclear. For one, oxides are believed to host TLS that could inadvertently couple to readout microwaves. Any unnecessary oxide barrier around the junction is therefore undesirable. Second, given the sensitivity of the transport characteristics to charge, one questions whether charge noise would play a role in coherence times as with the Cooper pair box [7]. Since the local DOS on the superconducting island may differ from that on the electrodes, we surmise that the additional phase could modify the overall qubit Hamiltonian. Importantly, a defect of this sort is unlikely to occur in junctions fabricated using the Dolan technique from §4.1. Angled depositions in the plane of the junction will not produce islands of the variety shown in Fig. 5.6(b).

5.4 Transmon IV curves

We arrive at the main finding of this chapter which is the surprising similarity between the transport characteristics of standalone junctions and junctions shunted with a large on-chip capacitor, henceforth referred to as transmons. To our knowledge, IV curves of transmons have not been previously published, perhaps because conventional wisdom dictates that, given the greatly reduced charging energy E_C from the shunt, the phase fluctuations born out of dc measurements behave as if for large junctions. Given our dc transport experience and the availability of industry-grade transmons fabricated by Rigetti, we are in the unique position to test this assumption first by modeling the IV characteristics, then by measuring them.

In real experiments, the transmon is coupled to an environment with finite impedance. The goal therefore is to model phase fluctuations in the presence of *dissipation* by calculating the tunneling rates Γ^+ and Γ^- in Eq. (2.12). We approach this problem following V. Chandrasekhar [96]. First, the WKB approximation is used to calculate the tunneling probability $P = Ae^{-2/\hbar^2 \int_a^b \sqrt{2m(U(\phi)-E)}dx}$ of the phase particle in the washboard potential $U(\phi)$. Here, $A \approx 1$ is a wavefunction normalization

constant and a and b are the positions in phase space where the particle energy $E = U(\phi)$. Because we are concerned with current-biased junctions in which the washboard is slightly tilted, the attempt frequency ω_0 is modified to $\omega_{I0} = \omega_0(1-(I/I_c)^2)^{1/4}$ [8], and $E = \hbar\omega_{I0}/2$ is the new ground state energy from which the particle tunnels. Since the maximum amplitude of $U(\phi) \approx 2E_J$, the probability of *over-the-barrier* escape $\sim e^{-(2E_J-E)/k_bT}$ is assumed negligible compared to escape *through* the barrier at low temperature [96]. The tunneling rate is then simply $\Gamma^{\pm} = \omega_{I0}P^{\pm}/2$ where $P^{\pm}$ is the probability of tunneling to the right $(+)$ or left $(-)$.

At this point, we introduce the dissipation term in the form of the environmental admittance $Y(\omega)$. In Chapter 2, we modeled the transmon total environmental admittance without dissipation as $Y(\omega) = i\omega C_s$. This allowed us to calculate the excitation energies $\hbar\omega_{\text{transmon}} = \frac{1}{8}\sqrt{E_J E_C}$ from the poles of the response function, Eq. (2.16), where the charging energy $e^2/2(C + C_s)$ included the junction intrinsic capacitance C and the shunt C_s. If we now include the ohmic dissipation term R, which incorporates quasiparticle resistance and contributions from the driving electronics in parallel with the junction, the admittance becomes $Y(\omega) = (1/R) + i\omega C_s$. The addition of the $1/R$ term modifies the excitation energy to $\hbar\omega_R = \hbar\sqrt{\omega_{I0}^2 - \tau^{-2}}$ where $\tau = 2R(C + C_s)$ represents the decay time of the tunneling attempt frequency. The presence of dissipation means that the particle loses the excess energy gained after tunneling, and, instead of transitioning into the running state, the particle retraps in a neighboring local minimum, ready to tunnel again. It is this repeated process of trapping and tunneling that results in phase diffusion and an average measurable voltage in the superconducting branch of the IV curve.

From this perspective, the ratio E_C/E_J ought to have large impact on the tunneling rate, and thus the measured phase diffusion resistance R_0. Classically speaking, for fixed E_J, a large E_C corresponds to a small particle susceptible to fluctuations from current noise I_n in the shunt resistance R. Quantum mechanically, a large E_C translates to high tunneling probability since the

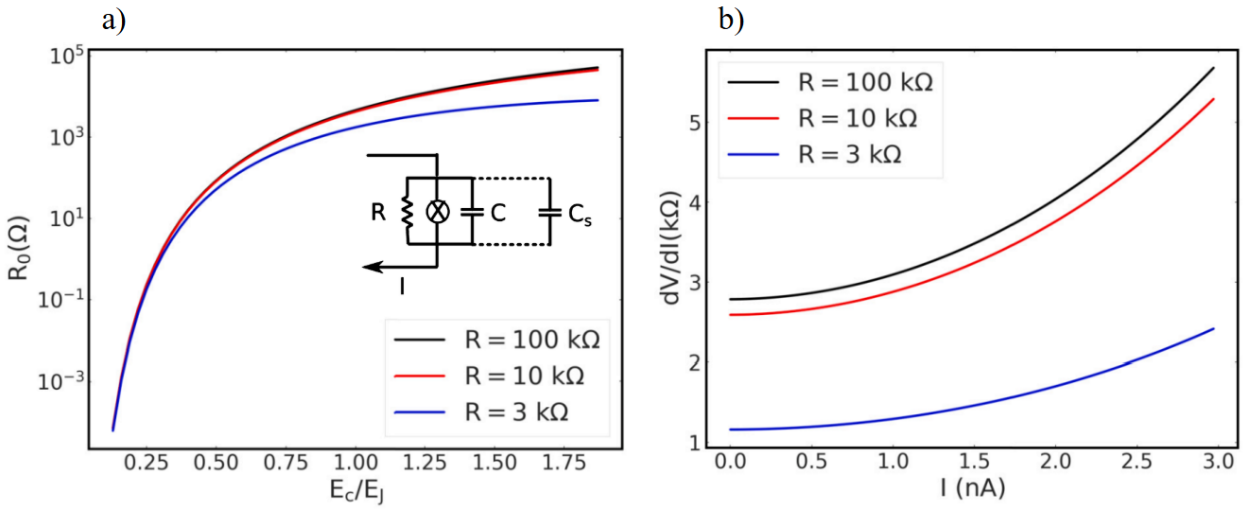

Figure 5.7: **WKB simulations of tunneling phase diffusion.** (a) Phase diffusion resistance as function of E_C/E_J for three values of R, the RCSJ shunt resistance shown in the inset. E_J fixed at 62 μeV, similar to the small junctions measured previously. (b) dV/dI vs $I_{\rm dc}$ for three values of R. E_C/E_J fixed at 0.9. Figures adapted from [96].

ground state energy $E(\omega_{I0})$ increases compared to the barrier height $2E_J$. Therefore, we expect the phase diffusion voltage to increase with E_C/E_J. Figure 5.7(a) shows the simulated R_0 due to quantum tunneling as a function of E_C/E_J for various value of R. The figure emphasizes the super-exponential growth of R_0 for $E_C/E_J < 1$, the transmon regime. According to these curves, we expect to measure $R_0 < 1$ mΩ in transmons regardless of the exact value of R.

To compare to measurements, V. Chandrasekhar also simulated the dependence of dV/dI on bias current $I \equiv I_{\rm dc}$ as shown in Fig. 5.7(b). The nonlinearity of dV/dI, which resembles our previous data, is due to two competing factors. First, ramping I lowers the height of the barrier relative to the ground state energy, increasing the probability of tunneling and the diffusion voltage. However, the ground state energy $E(\omega_{I0})$ itself decreases with I, counteracting somewhat the tunneling rate. Combined, these factors lead to an overall gradual increase in the differential resistance for $I < I_{\rm sw}$.

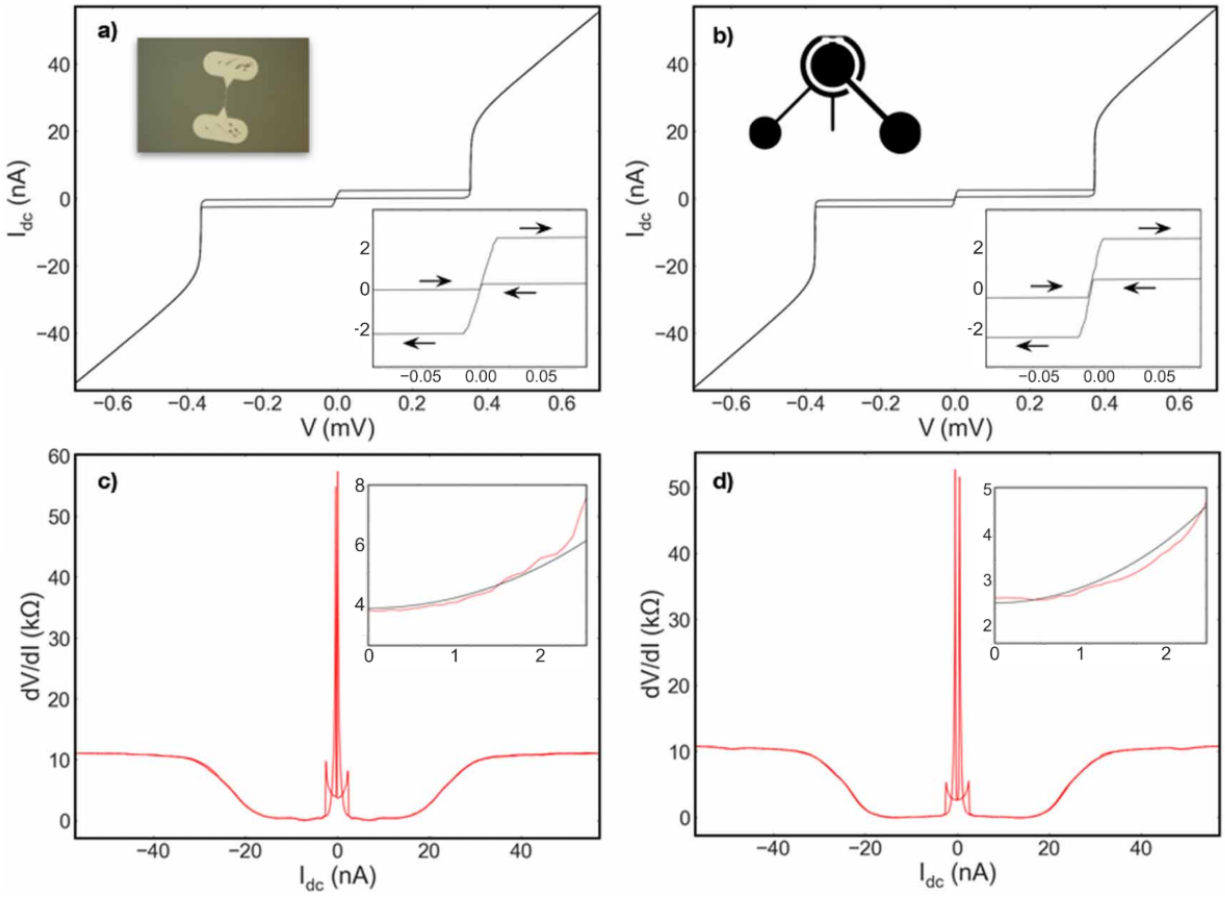

Figure 5.8: **Side-by-side transport data of standalone junctions and transmons.** (a) IV curve of a standalone junction with $R_N = 11.42$ kΩ. Insets: Optical image of the junction and enhanced view of $I_{\text{sw}} \sim 3$ nA. (b) IV curve for transmon with $R_N = 11.06$ kΩ. Inset: Schematic showing circular shunt capacitance ~ 100 fF and $I_{\text{sw}} \sim 3$ nA. Black arrows indicate direction of current sweep. (c) ((d)) dV/dI vs I_{dc} for the standalone (transmon) junction. Insets: Nonlinearity of the phase diffusion resistance around zero bias. WKB simulations in black using $E_C/E_J = 0.9$. Figure adapted from [38].

We now proceed to the data. Figure 5.8 shows side-by-side IV curves of a standalone junction and transmon. While $E_J \approx 50$ μeV in both junctions, E_C varies by a factor of 5 such that $E_C/E_J \sim 1/10$ for the standalone junction and $E_C/E_J \sim 1/50$ for the transmon. From the insets in Figs. 5.8(a) and (b), I_{sw} in *both* devices are suppressed by an order of magnitude from I_c. This is the first unexpected result. The larger phase inertia from the transmon shunt capacitance is expected to decrease the sensitivity of the particle to perturbations that would prematurely kick it into the running state. It appears, however, that the shunt has no effect on I_{sw}, implying that the *intrinsic capacitance* of the junction dictates phase dynamics.

This finding is further supported by the measured value of R_0 in the transmon. Figures 5.8(c) and (d) show dV/dI vs I_{dc} for the standalone junction and transmon, respectively. As $I_{\text{dc}} \to 0$, $R_0 = 3.63$ kΩ in the standalone junction and $R_0 = 2.78$ kΩ in the transmon. The fact that R_0 does not completely vanish in the presence of a large shunt capacitance is again surprising. According to simulations presented in Fig. 5.7(a), R_0 scales exponentially with the ratio E_C/E_J in small junctions and we expect R_0 in the transmon to be much smaller than R_0 in the standalone junction. The data contradict this assumption. It seems that from the point of view of phase diffusion, the ratio E_C/E_J in a capacitively-shunted junction is commensurate with that of an unshunted junction.

While interesting, we emphasize this finding is not a referendum on superconducting circuit QED writ large. The implied E_C/E_J from phase diffusion measurements does not impact the qubit resonance frequency $\omega_{\text{transmon}} \propto \sqrt{E_C E_J}$. In fact, the average T1 time measured for 24 transmon qubits fabricated identically to the one shown in Figs. 5.8(b) and (d) was $\bar{T}_1 = 76 \pm 13$ μs in the range $\omega_{\text{transmon}} = 3.8 - 4.2$ GHz [100]. We do not contest the effect of C_s on qubit coherence. Rather, our data suggest that noise-induced phase fluctuations ignore the shunt capacitor and may limit the coherence times of Josephson junction-based superconducting qubits overall.

We note the magnitude $R_0 \sim 10^3$ kΩ corresponds to $E_C/E_J \sim 1$ according to simulations using the quantum Langevin approach [15], [96] (see Fig. 5.7(a)). We have estimated, however, $E_C/E_J \sim 1/10$ in the standalone junction based on very rough "back-of-the-envelope" calculations of the intrinsic capacitance. While E_J is precisely calculated from the IV, there is large uncertainty tied to E_C. This may explain why, for instance, simulations assuming $E_C/E_J = 0.9$ provides the best fit to the data in Figs. 5.8(b) and (d). What *is* precisely known, however, is $E_C/E_J \sim 1/50$ in the transmon since these devices were resonant in the corresponding microwave frequency range [100].

Finally, we address the assertion that because transmons are not current-biased during operation, dc transport measurements are somewhat irrelevant. Given the fact that most frequency-tunable transmons exist in a two-junction loop through which external flux is thread, it is entirely possible that circulating screening currents tilt the washboard enough to cause phase diffusion. If the diffusion results in dissipation, severe limitations on the coherence time could be imposed.

CHAPTER 6

EXPERIMENTAL RESULTS: SNS JUNCTIONS

How would one create a superconducting qubit from a normal metal wire? SNS junctions have negligible intrinsic capacitance since their superconducting electrodes do not form a parallel plate capacitor. With $C \sim 0$, the RCSJ model breaks down as the notion of a phase "particle" no longer carries meaning. Despite this fact, we know the CPR is still periodic, if not exactly sinusoidal. In principal, one could still leverage the junction nonlinearity to craft a Hamiltonian whose eigenenergies may form a computational basis state. This question of whether a superconducting qubit may be formed from "linear" normal metal Josephson junctions informs the following experiment.

6.1 Single SNS junctions

By way of introduction, we present data on a single SNS junction. Figure 6.1 shows the differential resistance dV/dI and voltage V measured across two superconductors coupled by a normal metal film as a function of bias current I_{dc}. Although the charging energy E_C is undefined, we deploy our definition for the Josephson coupling energy $E_J = \hbar I_c/2e$ from previous chapters. For our purposes, the *measured* I_c corresponds to the actual Josephson energy of the junction since we define $I_c = 9.0\ \mu$A as the dV/dI *peak* according to the figure. Although this choice for I_c is somewhat arbitrary, it allows us to easily track changes in I_c caused from external parameters.

Similarly to SIS junctions, we recover the normal state resistance R_N of the junction at high bias. Since there is no tunneling resistance, R_N is determined by the low-temperature resistance of the normal metal and interface contact resistance between Au and Al. Typically, $R_N \sim 10\ \Omega$ for these SNS junctions. In addition to E_J, another important energy is the Thouless energy

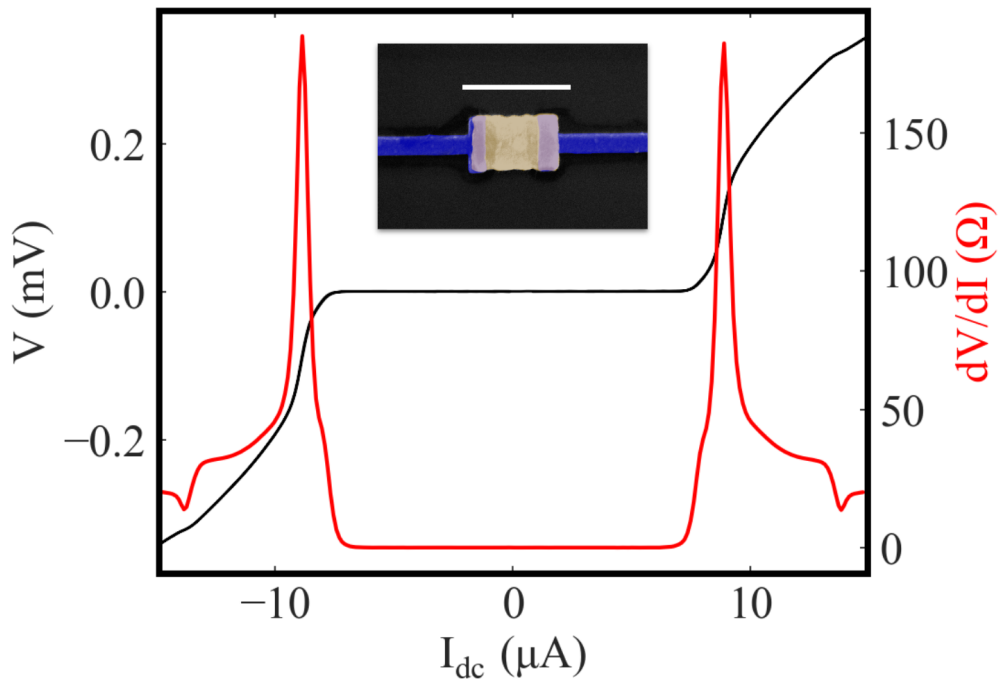

Figure 6.1: **IV curve of a single SNS junction at 400 mK.** Supercurrent branch associated with true zero resistance. $I_c = 9.0$ μA determined by the dV/dI maximum. $R_N = 20.2$ Ω determined from the IV at high bias. Inset: False-colored SEM image. Au is gold and Al is blue. Scale bar denotes 1 μm.

$E_{\text{Th}} = \hbar D/L^2$ which generally characterizes the proximity effect in diffusive normal metals. The representative length L here is the length of the normal metal between superconducting electrodes, and the diffusion constant D is calculated from the sheet resistance R_s discussed in §4.3.4. In this device, $R_s = 0.32$ Ω and $L = 0.5$ μm which results in $E_{\text{Th}} = 65$ μeV. The gap of Al is assumed to be ~ 180 μeV such that the junction is analyzed in the long-junction limit $\Delta > E_{\text{Th}}$.

The maximum possible critical current supported in a single 1D SNS junction is predicted to be $I_{c,\text{max}} = 10.82E_{\text{Th}}/eR_N$ at low temperatures [101]. Using the calculated values of R_N and E_{Th}, we calculate $I_{c,\text{max}} \approx 35$ μA for the junction shown in Fig. 6.1. We suspect $I_c < I_{c,\text{max}}$ due to a combination of factors including imperfect Au/Al interface transparencies, elevated measurement

temperature, and the specific 2D-geometry of the normal metal. Nonetheless, critical currents in diffusive metal junctions are generally much larger than in superconducting tunnel junctions and likewise sensitive to temperature and magnetic field . In terms of temperature, Dubos *et al.* predict $I_c \propto T^{3/2}e^{-L/L_{\text{Th}}}$ using quasiclassical theory for long-limit junctions [101]. Within a limited temperature range, this dependency is numerically similar to $I_c \propto e^{-L/L_{\text{Th}}}$ where $L_{\text{Th}} \propto 1/\sqrt{T}$. In other words, I_c is reduced with temperature according to the Thouless length exponential decay constant. We will use elevated temperature as a tool to reduce I_c for the benefit of data collection on three-terminal devices.

An interesting experiment is to track the behavior of I_c in response to an applied magnetic field B as shown in Fig. 6.2(a). Due to quantum interference of the Josephson current density inside the junction, a Fraunhofer-like diffraction pattern for $I_c(B)$ is predicted for an external field applied perpendicular to the surface area of the normal metal. Contrary to expectations, however, we do not observe a standard Fraunhofer pattern $I_c \propto |\text{sinc}(\pi\Phi/\Phi_0)|$ in the data. I_c does not exhibit a node at $\Phi = \Phi_0$ nor an amplitude peak for $\Phi_0 < \Phi < 2\Phi_0$. See Fig. 6.2(b).

Implicit to conventional Fraunhofer diffraction is a *sinusoidal* current-phase relation. The phase interference pattern is typically derived by summing the components of the line integral $\Phi = \oint \mathbf{A} \cdot ds$ enclosing the flux as shown in the inset of Fig. 6.2(b). Since $\mathbf{A} = (\Phi_0/2\pi)\nabla\phi$, integral contributions taken along the superconducting electrodes are zero (where $\nabla\phi = 0$), leaving $\gamma_1 - \gamma_2 = 2\pi\Phi/\Phi_0 (\text{mod } 2\pi)$ where γ_i are phase differences taken along the normal metal. This relation holds for all contours within the normal metal. Therefore, the local value of the supercurrent density J_s must oscillate with position (x, y) to accommodate this constraint on flux. In junctions for which $I_s = I_c \sin\phi$, this results in "Josephson vortices," cycles of $J_s(x, y)$ which carry no net current. At higher fields, these vortices cancel most of the net supercurrent and the interference pattern decays as $1/\Phi$. We surmise the reason the SNS junction fails to display a stan-

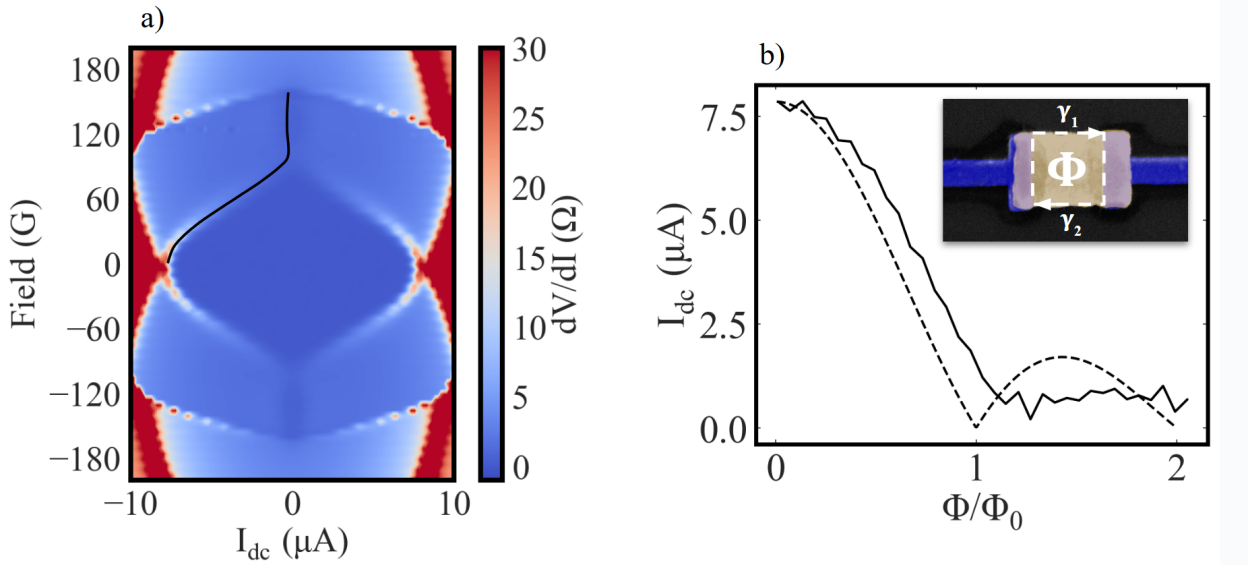

Figure 6.2: **Field dependence of a single SNS junction.** (a) dV/dI heat map measured as a function of I_{dc} at 5-G increments of external field B. Black line traces the steepest negative slope of dV/dI. (b) Data extracted from (a) (solid line) vs Fraunhofer diffraction pattern (dotted line) as a function of normalized flux Φ calculated from the area $A = 0.5 \times 0.5$ μm^2 of the normal metal depicted in the inset.

dard Fraunhofer is two-fold. First, the CPR of this SNS junction is not purely sinusoidal and the vortex structure may be highly irregular. Second, screening currents at high field tend to reduce the effective flux, an effect more pronounced in junctions with large I_c [8].

We have just described how $E_J \propto I_c$ of an SNS junction depends on temperature and magnetic field. If one wishes to create a frequency-tunable qubit, it is unlikely that favorable coherence times would arise from modifying these global degrees of freedom. We require more focused control over I_c without adding excess energy to the system. This brings us to our first multiterminal device — one that allows us to tune I_c *in-situ* without introducing dissipation.

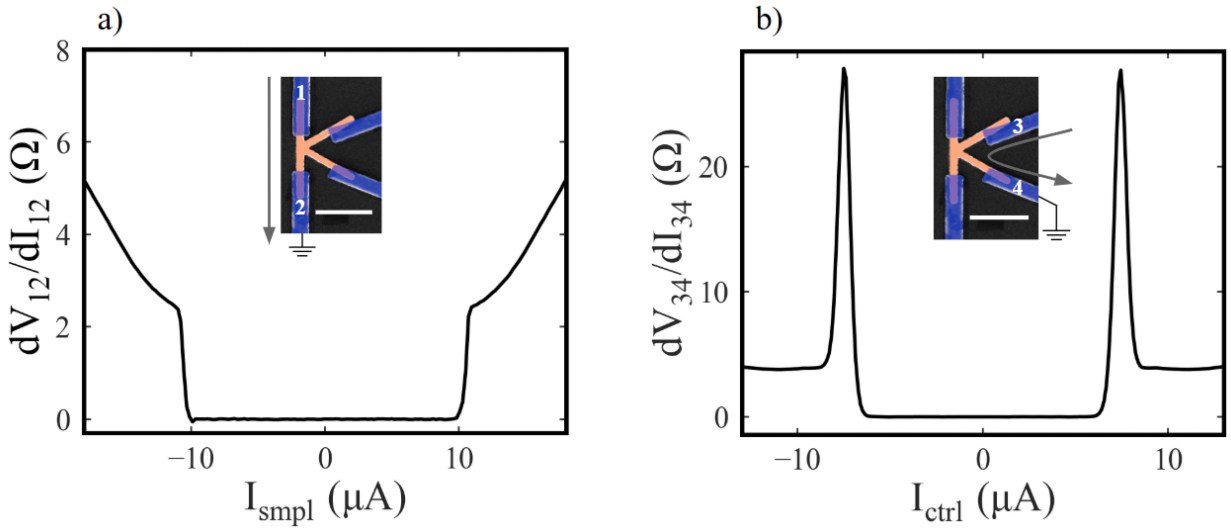

Figure 6.3: **Differential resistance of a four-terminal SNS junction at 300 mK.** (a) ((b)) dV/dI vs I_{smpl} (I_{ctrl}) across sample (control) junction using leads 1 and 2 (3 and 4). Unused leads are floated to ensure they do not draw current. Insets: Colorized SEM image. Arrows show direction of current flow. Au is orange. Al is blue. Scale bar represents 1 μm.

6.2 Supercurrent tuning of the Josephson energy

In this section, we show that driving supercurrent through a pair of superconducting leads coupled to an SNS junction reduces I_c of that junction. Figure 6.3 shows the device under consideration. We distinguish the "sample" junction whose I_c we wish to tune from the "control" junction used to apply the supercurrent. The sample junction leads lie vertically and the control junction leads attach to the sample junction at 45° angles. From the figure, it is clear that, although the junctions share a common normal metal wire, the critical current of the sample junction is $\sim 33\%$ larger than that of the control junction. This follows from $I_c \propto e^{-L/L_{\text{Th}}}$ since L of the sample junction is noticeably shorter than L of the control junction.

We are interested in the behavior of the device when the junctions are measured simultaneously. To achieve this, supercurrent across the control junction I_{ctrl} is driven independently from

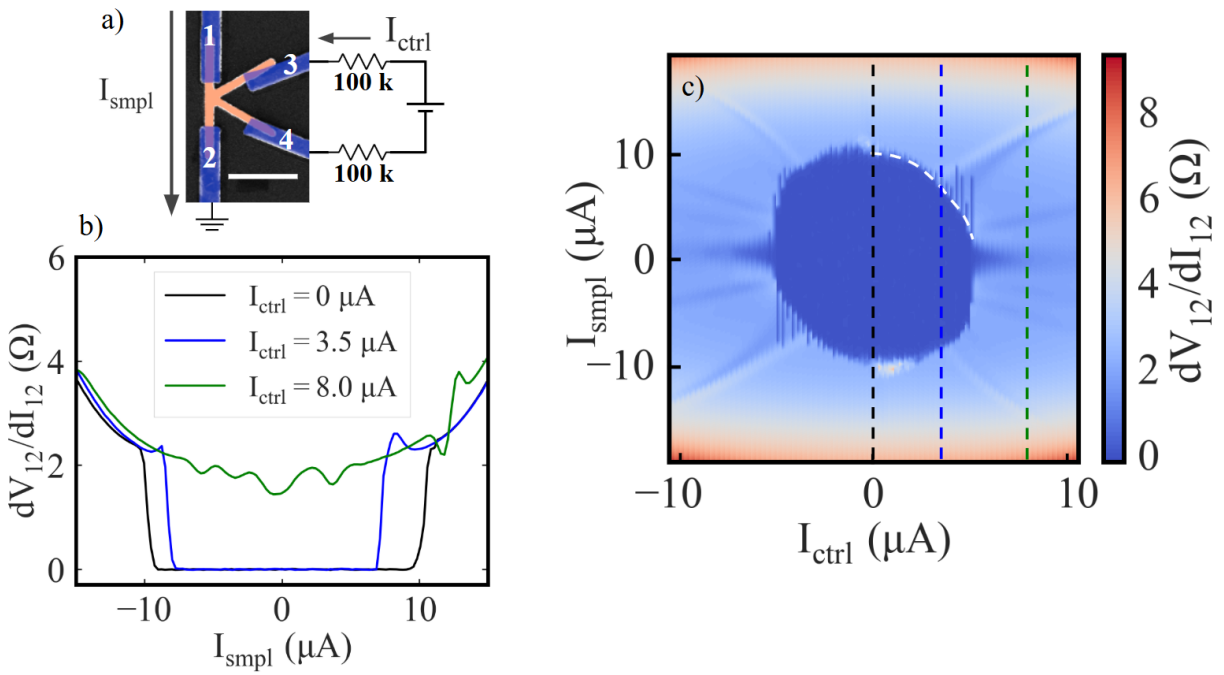

Figure 6.4: **Resistive heat map of a four-terminal junction.** (a) Circuit schematic of the floating current source limiting the device to single grounding point. (b) dV/dI measured across sample junction at three different increments of control current I_{ctrl}. (c) dV/dI heat map of the sample junction interpolated from 0.25-μA steps in I_{ctrl}. Colored vertical dotted lines correspond to the traces in (b). White dotted line outlines the first quadrant of the CCC (from §3.3). Figure adapted from Ref. [102].

supercurrent across the sample junction I_{smpl}. Figure 6.4(a) depicts the measurement setup and Fig. 6.4(b) shows several traces of dV_{12}/dI_{12}, the differential resistance across the sample junction, at various sustained value of I_{ctrl}. A heat map is stitched together from 40 consecutive sweeps of I_{smpl} in Fig. 6.4(c). The most important feature here is the suppression of the sample junction I_c due to I_{ctrl}, indicated by the white dotted line in the figure. From this line, we see that by driving dissipationless supercurrent into the junction, I_c is monotonically reduced from its maximum value to nearly zero.

It is important to emphasize this method of tuning of E_J does not cause energy loss. This

contrasts to earlier experiments by Baselmans *et al.* where I_c was controlled with dissipative quasiparticle charge current driven directly across the normal metal [103]. Microscopically, I_{smpl} is determined by the quasiparticle DOS inside the normal metal. Through the CPR, driving I_{ctrl} imposes a phase difference ϕ across the control junction which modifies the DOS along the entire length of the normal wire including the part that intersects with the sample junction. In this way, we are able to tune the critical current without dissipation — a promising first step towards realizing an SNS-based frequency-tunable qubit.

Also evident in the heat map of Fig. 6.4(c) are radial streaking features that persist to regions of higher current bias. These features appear as modulations in the differential resistance as illustrated by the green trace in Fig. 6.4(b). The streaks are not present when only one junction is measured at a time (Fig. 6.3) suggesting they result from the sample junction cross-coupling with the control junction in the resistive state. Supercurrent flow may be enhanced when the voltage at one superconducting contact is commensurate with a finite potential across another two contacts [104]. Similar radial streaking observed in prior studies were attributed to non-local Andreev processes (see Fig. 3.6(c)). Given the diffusive nature of the normal metal in our devices, however, these streaks are unlikely to arise from bound state resonances [102].

6.2.1 Tuning the critical current of a SQUID

Another way to analyze the critical current is in a two-junction SQUID loop shown in Fig. 6.5(a). In addition to supercurrent, magnetic flux Φ threaded through the SQUID also changes I_c. With two independent variables, the parameter space for dV/dI measurements becomes unwieldy to represent graphically. Therefore, to streamline data collection, we utilize a home-made PID controller locked to I_c of the SQUID. Figure 6.5(b) depicts a feedback circuit referenced to the resistive peak associated with I_c. Since our PID works optimally at a zero-voltage setpoint, the *second* derivative

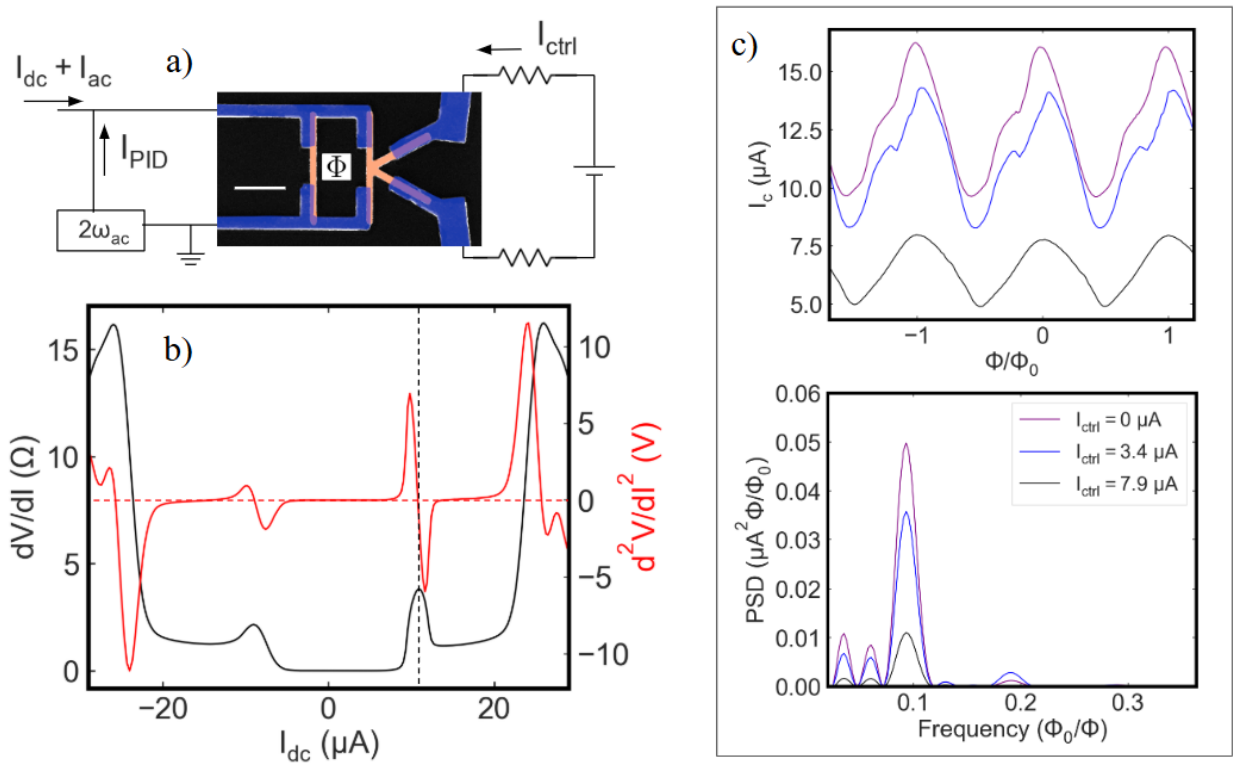

Figure 6.5: **Feedback circuit measurement of SQUID I_c.** (a) Circuit schematic of measurement. PID locks to the zero of d^2V/dI^2 signal extracted from the $2\omega_{ac} = 4\pi f_{LIA}$ component of $V(I)$. (b) First (black) and second (red) derivative of $V(I)$ across the SQUID at $T = 500$ mK. $I_{ac} = 1$ μA to broaden the transition and enable PID locking. Red dotted line denotes PID setpoint. (c) Example traces of the feedback circuit locked to $I_c(\Phi)$. Second harmonic PSD amplitude vanishes for $I_{ctrl} = 7.9$ μA. Subharmonic peaks result from numerical processing discussed in the text. Figure adapted from Ref. [102].

signal dV^2/dI^2 is fed into the PID input. The PID output current I_{PID} is summed with a dc offset current I_{dc} to initialize the SQUID at the critical current $I_c = I_{dc} + I_{PID}$. Since I_{dc} is a constant, simply recording I_{PID} gives I_c of the SQUID. When properly locked, this feedback technique maps $I_c(\Phi, I_{ctrl})$ much quicker than standard differential resistance measurements.

Figure 6.5(c) shows a few traces of $I_c(\Phi)$ using the feedback technique. As expected, periodic oscillations corresponding to the superconducting flux quantum Φ_0 are observed. Due to the device

asymmetry, the amplitude of these oscillations decrease as the supercurrent drive I_{ctrl} is increased. The additional leads on the right side of the SQUID makes the critical current of the right junction $I_{c\text{R}}$ smaller than the critical current across the left junction $I_{c\text{L}}$. As a function of flux, the total SQUID I_c will therefore oscillate between $I_{c\text{L}} + I_{c\text{R}}$ and $I_{c\text{L}} - I_{c\text{R}}$. From the purple trace in Fig. 6.5(c), the minimum I_c is $9.7\ \mu A$ and the maximum is $16.3\ \mu A$ such that $I_{c\text{L}} = 13.0\ \mu$A and $I_{c\text{R}} = 3.3\ \mu$A. Since the SQUID branches act in parallel, I_{ctrl} reduces both $I_{c\text{L}}$ and $I_{c\text{R}}$ simultaneously and we expect the differences between them to converge at higher I_{ctrl}. Indeed, the amplitude of the oscillations at $I_{\text{ctrl}} = 7.9\ \mu$A in black are much smaller than at $I_{\text{ctrl}} = 0\ \mu$A in purple.

In contrast to a conventional SIS-based SQUID, the CPR of SNS SQUIDS are not strictly sinusoidal. The power spectral density (PSD) provided in Fig. 6.5(c) confirms the existence of a higher harmonic component associated with a period $\Phi_0/2 = h/4e$ in oscillations measured at $I_{\text{ctrl}} = 0\ \mu$A and $I_{\text{ctrl}} = 3.4\ \mu$A. The second harmonic does *not* appear in oscillations at $I_{\text{ctrl}} = 7.9\ \mu$A. Subharmonic peaks result from symmetrically "padding" the flux-domain data with several hundred zeroes to smooth the spectral plot — they do not correspond to physical phenomena in the data. The PSD is interpreted from the non-sinusoidal current-phase relation of the four-terminal junction on the right side of the SQUID. It was recently theorized that the relative strength of the 2π- and 4π-periodic contributions in the CPR of one junction may be tuned by applying a phase difference across another junction coupled to the same normal metal wire [54]. Although the phase across the control junction ϕ_{ctrl} in this case cannot be directly known, its value is changed by driving supercurrent I_{ctrl} through the leads. Initially, at $I_{\text{ctrl}} = 0\ \mu$A, $\phi_{\text{ctrl}} = 0$ and the I_c oscillations of the SQUID contain hints of a second harmonic component. The relative strength of these harmonics increases when the ϕ_{ctrl} becomes finite at $I_{\text{ctrl}} > 0$. See the blue curve in Fig. 6.5(c). Eventually, upon further increasing I_{ctrl}, the second harmonic vanishes. At this point, ϕ_{ctrl}

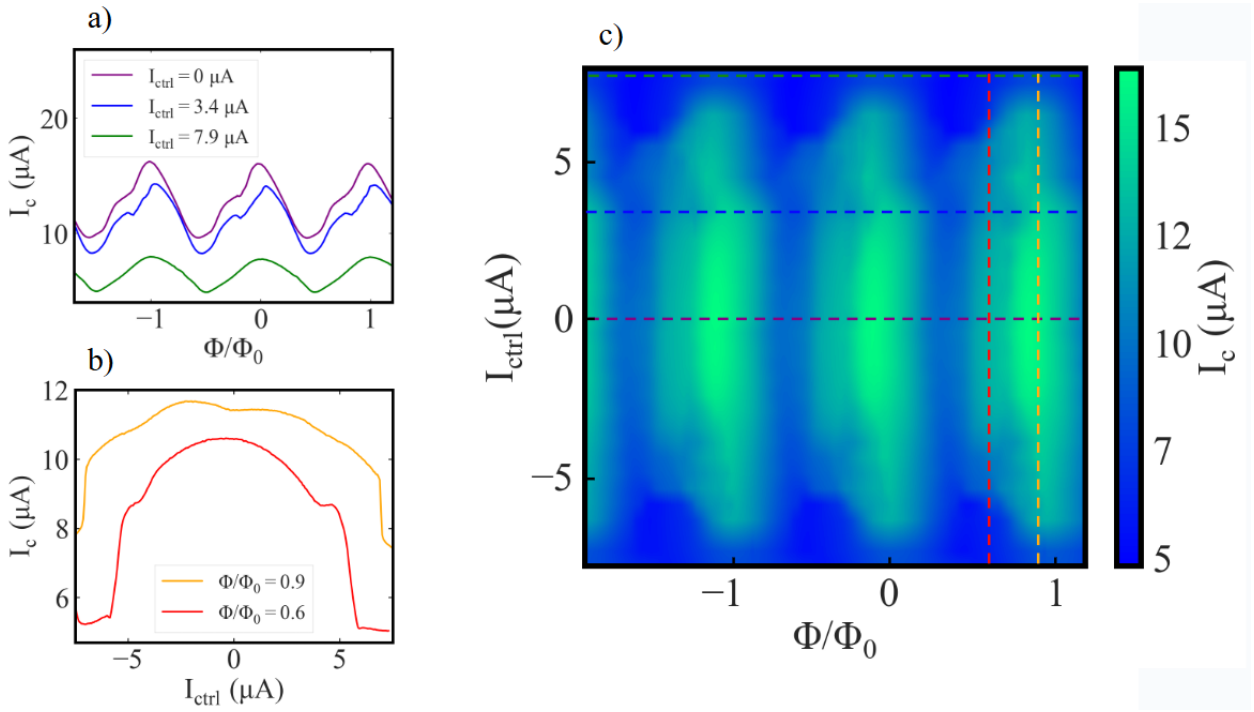

Figure 6.6: **SQUID I_c heat map.** (a) Example traces of measurement locked to $I_c(\Phi)$ at different I_{ctrl}. (b) Measurement locked to $I_c(I_{\text{ctrl}})$ at different sustained fluxes. (c) I_c heat map interpolated from 32 $I_c(\Phi)$ curves at incremental steps of I_{ctrl}. Colored dotted lines indicate traces in (a) and (b). Adapted from Ref. [102].

is undefined since $I_{\text{ctrl}} \sim I_{c,\text{ctrl}}$ the critical current of the control junction. Further increasing I_{ctrl} has no effect on the oscillations. The fact that oscillations in $I_c(\Phi)$ are observed in the SQUID at $I_{\text{ctrl}} \sim I_{c,\text{ctrl}}$ means phase coherence around the loop *remains* even after Josephson coupling is broken, a somewhat unexpected finding. We speculate that pair correlations from the Al electrode on the right side of the SQUID maintain phase continuity around the SQUID loop above $I_{c,\text{ctrl}}$.

We conclude our discussion of the SQUID by presenting the full critical current heat map in Fig. 6.6, accumulated by locking the PID to $I_c(\Phi)$ while incrementing I_{ctrl} by 0.5 μA from -8 μA to $+8$ μA. Two features in the heat map are immediately apparent. First, I_c clearly oscillates with a fundamental period corresponding to Φ_0 for all I_{ctrl}, and second, for $|I_{\text{ctrl}}| \lesssim 3.5$ μA, the

oscillations are skewed with respect to flux. These characteristics are nicely encapsulated in the I_c vs Φ data, reproduced in Fig. 6.6(a).

Most relevant to *qubit* physics is Fig. 6.6(b) which shows the dependence of I_c — the total Josephson energy — on supercurrent bias. The implementation of a flux-biased SQUID enables configuration of the SNS junction at various Josephson energies since the amount of supercurrent circulating around the SQUID depends on the flux. From the data, we see that more supercurrent is required to screen a flux quantum from penetrating the loop at $\Phi = 0.6\Phi_0$ compared to at $\Phi = 0.9\Phi_0$. This results in a smaller I_c as shown by the red curve in Fig. 6.6(b). Regardless of flux, $I_c(I_{\text{ctrl}})$ remains monotonic, implying some degree of control over E_J similarly to the previous four-terminal device. The sharp downward slope for $I_{\text{ctrl}} > 5$ μA occurs when Josephson coupling is destroyed in the right side of the SQUID. For values of I_{ctrl} before this transition, I_c is modulated by roughly 20%, demonstrating that the Josephson energy of the two-junction loop is sensitive to supercurrent flowing through either branch, regardless of the effective initial Josephson energy of the device [102].

Let us take a moment to make a direct connection between these devices and modern SIS-based superconducting qubits. While the SQUID demonstrates a more complete picture of how one may tune E_J with supercurrent, a loop is *not* required to see this effect, as demonstrated by the first four-terminal device. In fact, we suspect a "loopless" geometry would greatly reduce the qubit's susceptibility to flux noise, a problem that has persisted since the advent of the frequency-tunable transmon utilizing a SQUID at its core [25]. We believe the flux-insensitivity to magnetic noise could be one of the greatest strengths of a MTJJ-based qubit. Furthermore, we point out that the good Al/Au interface quality of our device prevents charge from accumulating on the superconducting electrodes. Compared to parallel-plate SIS or superconductor-semiconductor junctions, the multiterminal SNS design likely has inherently less charge noise arising from fluctuations in

the charging energy across the junction. This, along with the absence of a flux-sensitive loop, could also lead to high coherence times in SNS qubits. To investigate the stability of the qubit resonance frequency on bias supercurrent, and to test the noise-insensitivity, we await the implementation of multiterminal SNS devices in microwave readout circuits — experiments that are unfortunately beyond the scope of this thesis.

6.3 Phase interference of a multiterminal junction

The following experiment on a four-terminal SNS junction is inspired by the prediction that superconductor-*topological insulator*-superconductor Josephson junctions may host localized Majorana bound states. One strong piece of evidence for these exotic states is supposedly found in the phase diffraction pattern of $I_c(\Phi)$. In particular, the conventional Fraunhofer pattern is expected to display *lifted* odd-numbered nodes consistent with 4π-periodicity of the CPR [105]. With non-exotic, non-topological materials Au and Al, we investigate whether a similar diffraction pattern may result from a normal weak link biased by supercurrent.

Figure 6.7 shows a four-terminal SNS junction fabricated from a normal metal film wide enough to support several superconducting flux quanta at an applied field of ~ 200 G. Similarly to the previous devices, we label the pair of vertical superconducting leads the "sample" junction and the horizontal leads the "control" junction. The differential resistance curves of Figs. 6.7(a) and (b) serve to highlight the critical current of the control junction $I_{c,\,\mathrm{ctrl}}$ and sample junction $I_{c,\,\mathrm{smpl}}$, respectively. Somewhat unexpectedly, it appears $I_{c,\,\mathrm{smpl}} < I_{c,\,\mathrm{ctrl}}$ despite the fact that L of the sample junction is less than L of the control. Also, $I_{c,\,\mathrm{ctrl}}$ is greater than I_c of the *single* junction of nearly identical size and shape (see Fig. 6.1). We attribute the enhanced critical current in the four-terminal device to a stronger proximity effect arising from the additional superconducting contacts of the sample junction. The double-peaked nature of Fig. 6.7(b) suggests the existence

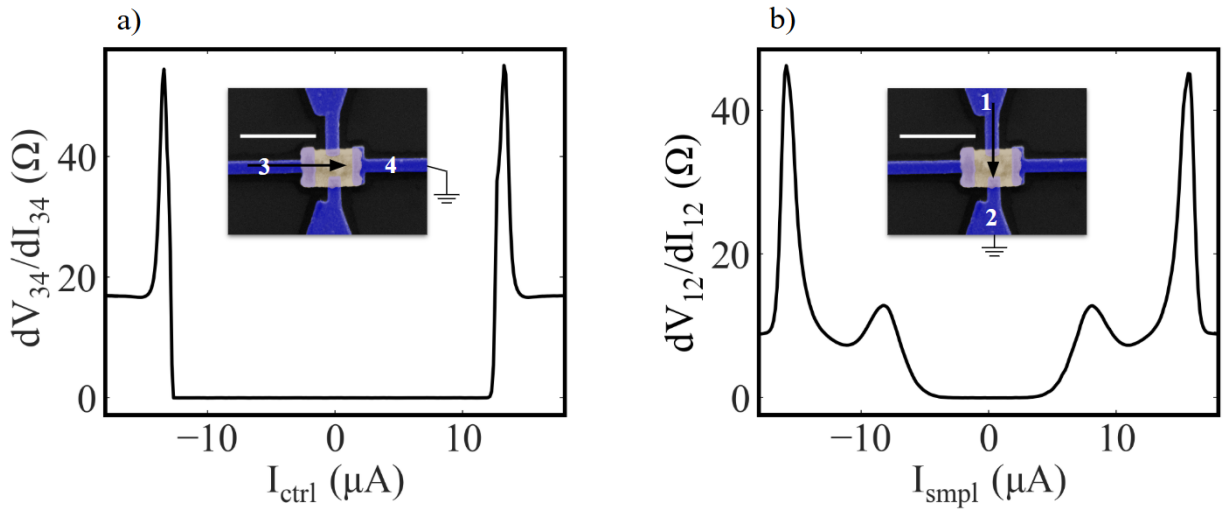

Figure 6.7: **Differential resistance of a four-terminal *wide* SNS junction at 400 mK.** (a) ((b)) dV/dI across leads 3 and 4 (1 and 2) of the control (sample) junction as a function of current bias I_{ctrl} (I_{smpl}). Insets: Colorized SEM images with measurement leads labeled. Unlabeled leads are floating. Scale bar represents 1 μm. Black arrow indicates direction of dc bias.

two critical currents, one associated with supercurrent transported directly between sample leads, and one associated with supercurrent mediated by the control leads. While the control leads are floated during measurement of the sample junction, they are nonetheless characterized by a distinct superconducting phase and may therefore mediate the transfer of supercurrent even if they draw no net current [54].

Our main objective is to investigate the flux-induced phase interference between the four superconducting terminals. Figure 6.8(a) shows differential resistance heat maps for the sample junction in the presence of an externally applied magnetic field B, and Fig. 6.8(b) shows the resulting phase diffraction pattern of $I_{c,\,\text{smpl}}(\Phi)$. Notice that at $I_{\text{ctrl}} = 0$, the heat map reveals a secondary diffraction lobe. Unlike in the case of the single junction, $I_{c,\,\text{smpl}}$ no longer monotonically reduces with field. Apparently, with the addition of two superconducting leads, we regain aspects of the standard Fraunhofer pattern. In the panels in Fig. 6.8(a), as I_{ctrl} is increased transverse to the sample junc-

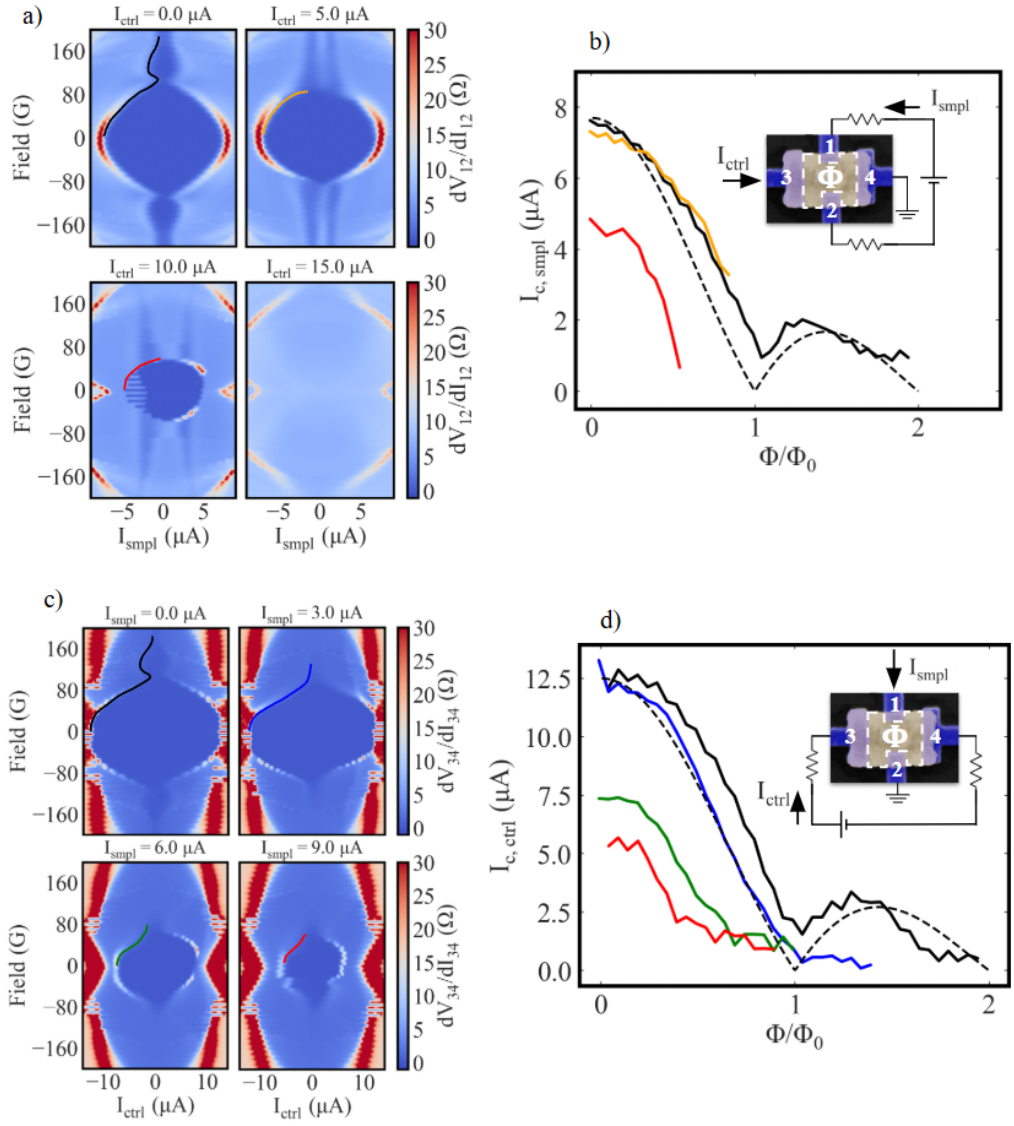

Figure 6.8: **Four-terminal phase diffraction patterns at 400 mK.** (a) ((c)) dV/dI heat maps measured across sample (control) junction as a function of external field at increments of control (sample) current bias. (b) ((d)) Critical current of sample (control) junction extracted from the steepest negative slopes of the (a) ((b)). Curves are color-coordinated with the lines drawn on the heat maps. Dotted black line denotes standard Fraunhofer pattern. Insets: Circuit schematics of the measurement. Dotted white line outlines flux area used to calculate Fraunhofer pattern.

tion, the maximum $I_{c,\,\mathrm{smpl}}$ decreases as we expect from our findings on the previous four-terminal device in §6.2. Additionally, we observe the zero-resistance region shrink with respect to field at larger I_{ctrl}, and, in place of the second diffraction lobe, peculiar vertical streaks associated with lower resistance appear. Finally, in the last panel where $I_{\mathrm{ctrl}} = 15\ \mu\mathrm{A} > I_{c,\,\mathrm{ctrl}}$, the zero-resistance region completely vanishes.

When the roles of the control junction and sample junction are swapped, that is, when $I_{c,\,\mathrm{ctrl}}(\Phi)$ is probed at increments of supercurrent I_{smpl} sustained across the sample junction, a trend emerges. From Figs. 6.8(c) and (d) a diffraction pattern resembling a conventional Fraunhofer is again recovered when the transverse supercurrent is zero, and the maximum critical current $I_{c,\,\mathrm{ctrl}}$ dies down in proportion to the applied supercurrent across the sample junction.

While analysis is ongoing, we offer a preliminary interpretation of the data. Ref. [106] predicts that $I_c(\Phi)$ in "wide" junctions crosses over from a Fraunhofer pattern to a monotonic decay when the width w of the normal wire is shorter than a certain magnetic length $\xi_H = \sqrt{\Phi_0/H}$ where H is the effective magnetic field. In essence, the regular Josephson vortex array derived from 1D JJ cross-sections does not take form in wide junctions where the CPR is non-sinusoidal. Instead, irregular vortex structure causes destructive phase interference for $\Phi > \Phi_0$ in junctions where $w \sim \xi_H$ [106]. Indeed, in our *single* square-like SNS junction $w \sim L \sim \xi_H$, and we do not observe a secondary maxima associated with higher order phase diffraction. In the four-terminal junction, however, the vertical superconducting leads at the halfway point of the normal metal increase E_{Th} and decrease the effective L between superconducting contacts. We suspect the reason a Fraunhofer-like pattern is recovered in the four-terminal junction is because the geometry effectively reduces to one in which the vortex structure more closely resembles that of a 1D junction.

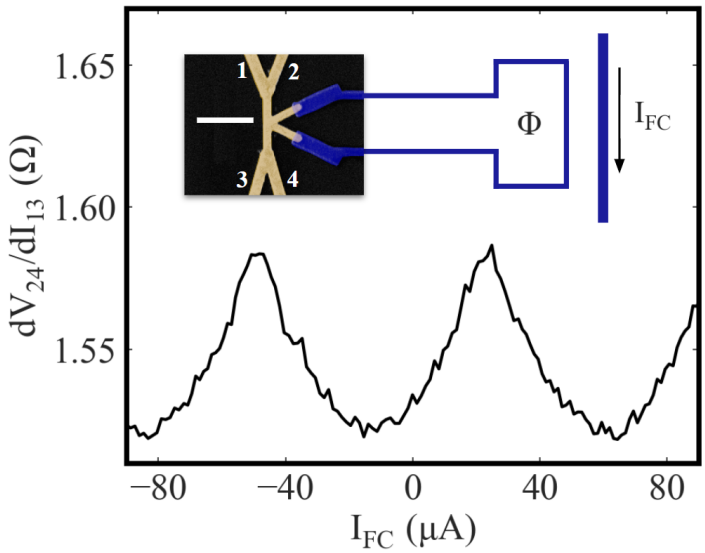

Figure 6.9: **Conductance measurement of a phase-biased junction at 400 mK.** Periodic conductance oscillations reflect the changing DOS from the phase difference across the junction. Period corresponds to Φ_0 threaded through the flux loop. Flux induced by dc current $I_{\rm FC}$ driven through the superconducting field coil. Inset: Schematic of the measurement circuit. V measured across leads 2 and 4. $I_{\rm ac}$ injected into 1 and drained through 3.

6.4 Phase-biased junctions

In the preceding experiments, we have seen how driving current through the junction allows one to measure *macroscopic* junction properties such as I_c. If, on the other hand, one wishes to probe the underlying non-equilibrium quasiparticle dynamics resulting from charge current *inside* the junction, a different device design is required. Here we introduce a "phase-biased" Josephson junction, commonly referred to as an *Andreev interferometer* (see e.g. Ref. [49]), where a phase difference is applied by connecting two superconductors in a loop. Using a single junction as an example, we discuss how the basic working principles of the Andreev interferometer allow us to probe the quasiparticle DOS inside an SNS device.

The advantage of our particular choice of clean Au is that L_ϕ and $L_{\rm Th}$ may be microns long,

and thus the length L of the Josephson junction may be made long enough to attach additional measurement probes. Figure 6.9 shows a junction attached to four normal metal probes used to measure the resistance R of a normal wire attached to an Andreev interferometer. Due to long-range phase coherence, the Green's function along the wire between normal reservoirs depends on the phase difference between the two superconducting reservoirs. At a phase $\phi = 0 \pmod{2\pi}$, R is large and decreases as $\phi \to \pi \pmod{2\pi}$. The exact value of R is due an enhancement of the normal metal diffusion constant D from Andreev pair correlation in conjunction with the so-called re-entrance effect at low temperatures [40]. As a function of temperature, R exhibits non-monotonic behavior with a minimum at $E_T \sim E_{\text{Th}}$ [107]. In our samples, although E_{Th} is too small to produce re-entrant behavior at experimentally accessible temperatures, we are concerned only with $R(\phi)$. This change in conductance is subtle and requires a sensitive measurement. As shown in the figure, the magnitude of variation in conductance is $\sim$10% of the normal state conductance.

The junction is "phase-biased" since we do not drive current directly through the superconducting contacts. Rather, the phase difference is varied by applying an Aharonov-Bohm-type magnetic flux through the area of a loop (see §3.2.4). In our experiments, we extend the main area of the loop ~ 100 μm away from the junction. By biasing dc current through an on-chip field coil, ϕ may be controlled according to $\phi = 2\pi\Phi/\Phi_0$ where Φ is the *net* flux enclosed by the loop. The coupling strength between the loop and coil is maximized and a relatively small bias current is needed to modify the phase by 2π. From Fig. 6.9, the period $\Delta I_{\text{FC}} \sim 72$ μA corresponds to one Φ_0 threaded through the loop.

In an experimental subtlety, the external flux Φ_{ext} created by the field coil may not necessarily equal Φ. Due to the self-inductance L of the loop, a screening current may partially block Φ_{ext} such that $\Phi = \Phi_{\text{ext}} - LI_s$ where I_s is the supercurrent flowing around the flux loop. Based on previous experiments utilizing similar loops [108], we estimate $L \sim 0.1$ nH and $I_s \sim 1$ μA. Effects from

flux loop screening currents are accounted for in the following experiment.

While the Andreev interferometer is a powerful tool for investigating phase-dependent transport phenomena, the addition of normal reservoirs imposes some constraints on quasiparticle dynamics. Namely, the quasiparticle DOS inside the normal metal never completely goes to zero to form a full minigap. Instead, the DOS reduces to about 20% of its normal reservoir value in devices where the length of the normal conductance wire is comparable to L [59]. We recognize that, in an alternative device design, a *fully*-gapped DOS may be directly probed via tunneling spectroscopy. While this latter approach may provide a clearer picture of the behavior of the DOS, we believe it would be very difficult to incorporate a tunneling contact into devices utilizing more than one independent flux loop.

6.4.1 Three-terminal phase-biased junctions

In our final experiment in which we provide both theory and data, we are interested in the topology of a diffusive multiterminal junction. One advantage of phase-biased junctions is that they are somewhat easier to simulate since, in quasiclassical theory, the phases are typically specified in superconducting reservoirs. Using the Riccati parameterization of the Usadel equation, Ref. [59] calculates the conductance of a normal metal wire coupled to three superconducting contacts to probe the topological band structure of diffusive multiterminal junctions in a similar manner to Strambini *et al.* [70]. Results from the quasiclassical simulation are shown in Fig. 6.10.

The addition of normal metal reservoirs to "Device 1" shown in Fig. 6.10(a) has major design implications. Since the DOS varies along the normal wire at scale defined by L_{Th}, the precise location on the device where the energy spectrum is probed will affect the conductance measurements. Also, for normal wires of various lengths coupled to superconductors, E_{Th} is difficult to quantify precisely. Nonetheless, the standard definition of E_{Th} is used to specify the lengths L of the normal

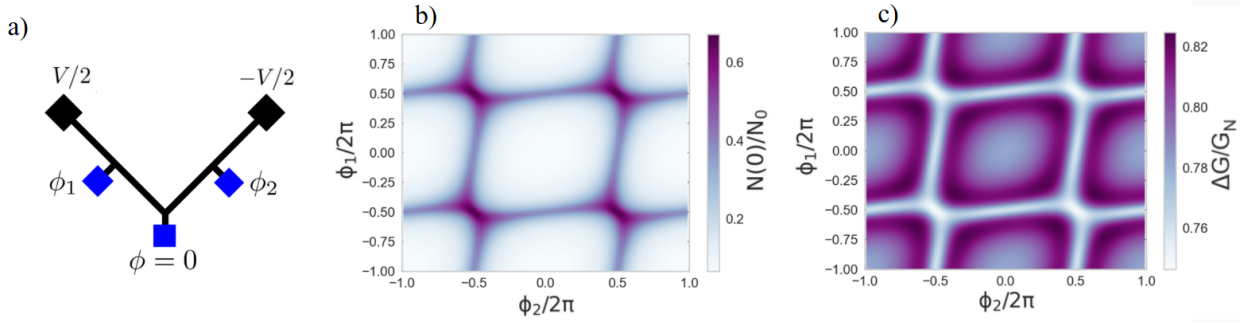

Figure 6.10: **Simulated conductance of Device 1.** (a) Device schematic with blue (black) squares representing superconducting (normal) reservoirs. Black lines represent normal wires with length $2L$ between normal reservoirs. (b) Calculated $N(0)$ at the midpoint of the sample as a function of (ϕ_1, ϕ_2). (c) Resulting change in conductance ΔG of the normal wire. Figure adapted from Ref. [59].

metal wires as well as set the scale for the temperature T and gap Δ in the simulations. Figure 6.10(b) shows the calculated DOS at the center of the device in Fig. 6.10(a), and Fig. 6.10(c) shows the corresponding change in conductance ΔG of the wire between two normal reservoirs. A clear correlation between the DOS at the Fermi energy $N(0)$ and ΔG is observed; the color plots appear as the inverse of the other. Upon careful inspection, however, one notices $N(0)$ never reaches the normal state value N_0 for any value of ϕ_1 or ϕ_2, i.e. there are no complete gap closings that could signify a topological transition. This poses a problem for those interested in probing the topological properties of the three-terminal junction.

Fortunately, in "Device 2," shown in Fig. 6.11(a), we find a solution. Here, the distance between all three superconducting electrodes is identical, and $N(0) = N_0$ at points *nearby* $\phi_1, \phi_2 = \pi \pmod{2\pi}$. See Fig. 6.11(b). Importantly, this plot closely resembles Fig. 3.4(b) which was calculated *without* the inclusion of normal metal reservoirs. It seems the requirement for a complete gap closing is an equivalency between L of the three junctions, regardless of whether or not normal metal probes are attached.

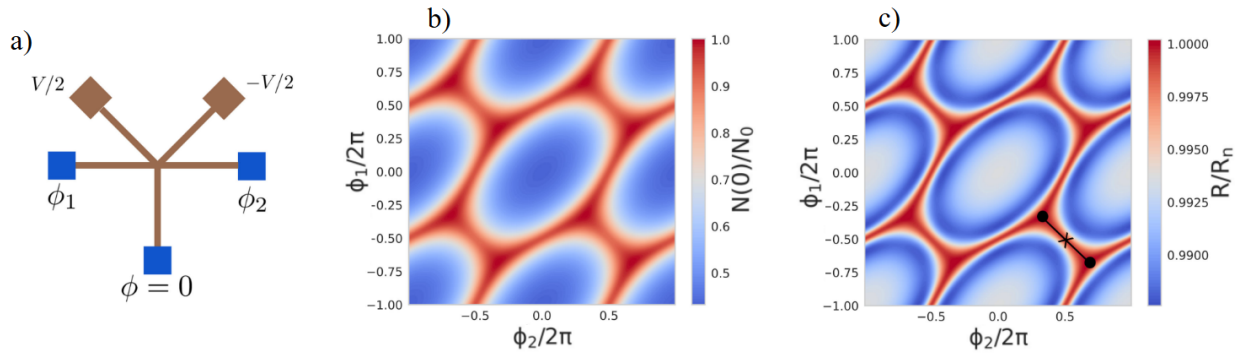

Figure 6.11: **Simulated conductance of Device 2.** (a) Device schematic analogous to Figure 6.10(a). Brown represents normal metal. All reservoirs located a distance L from common centerpoint. (b) Calculated DOS at the centerpoint. $N(0) = N_0$ twice per unit cell. (c) Low-temperature resistance R between the two normal reservoirs. Black dots correspond to gap closings. Figure adapted from Ref. [109].

How does the addition of normal reservoirs affect the Green's function? From §3.2.4, we know the modulation of $R(\phi_1, \phi_2)$ reflects changes in the retarded Green's function

$$\tilde{g}^R = \begin{pmatrix} \cos\theta & \sin\theta e^{i\chi} \\ \sin\theta e^{-i\chi} & -\cos\theta \end{pmatrix} \tag{6.1}$$

parameterized by θ and χ which characterize the strength and phase of the superconducting pair correlations, respectively. Strambini *et al.* show that a unit vector representing $\tilde{g}^R$ may be mapped onto the northern hemisphere of a Bloch sphere. Here, θ represents the polar angle and χ the azimuthal angle such when $\theta > \pi/2$, the Green's function vector lifts off the equator into what Strambini *et al.* define as a gapless state. Since our device has normal metal reservoirs, θ will never equal $\pi/2$ but rather approach some maximum value $\theta_{\text{max}} < \pi/2$. Figures 6.12(a) and (b) show the real part of $\theta(\phi_1, \phi_2)$ and $\chi(\phi_1, \phi_2)$ in the center of the wire of Fig. 6.11(a). Following Strambini *et al.*, we label each gapped region corresponding to the maximum θ with a pair of integer indices (n_1, n_2) as shown in Fig. 6.12(a). These indices represents the topologically distinct winding

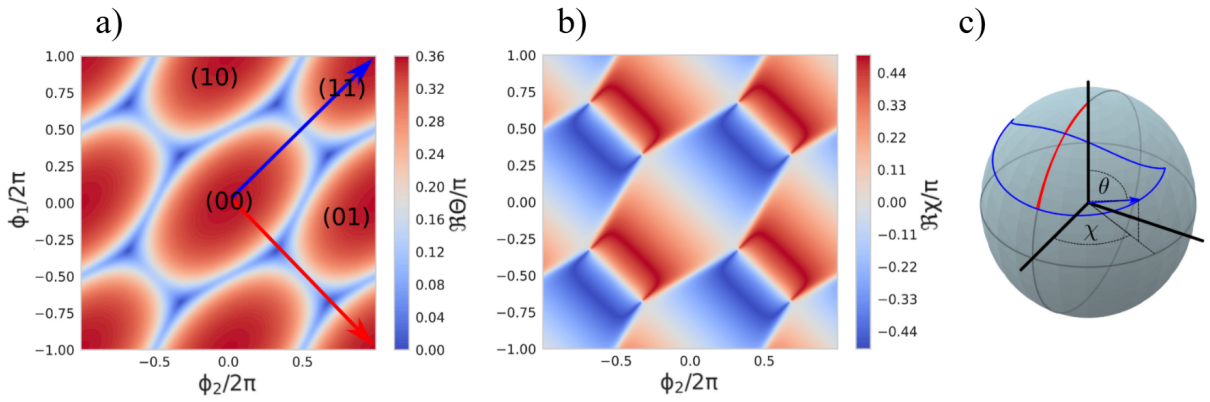

Figure 6.12: **Three-terminal Green's function in phase space.** (a) ((b)) Real part of θ (χ) simulated at the centerpoint of the three-terminal device as a function of ϕ_1 and ϕ_2. Integer indices characterize topologically distinct gapped regions. (c) Bloch sphere representation of $\tilde{g}^R$ where $\Re\theta$ and $\Re\chi$ represent the polar and azimuthal angles, respectively. $\Re\theta_{\text{max}} = 0.36\pi$ represents maximally gapped state. Red and blue trajectories correspond to lines in (a). Figure adapted from Ref. [109].

numbers of the phases ϕ_1 and ϕ_2. In order to move in phase space from one index to another, one must pass over regions in which the system approaches the purely normal state corresponding to $\theta \sim 0$ and $\chi = 0$. In the figure, two possible trajectories are marked in blue and red. Notice the blue trajectory does not pass over $\Re\theta = 0$ whereas the red trajectory does. Both trajectories, however, cause the Green's function to lift from a "gapped" state (following Strambini *et al.*) at $\theta_{\text{max}} \sim 0.36\pi$ in traversing from one topological index to another.

On the experimental side, we prefer L to be as short as possible to maximize the proximity effect and increase $\theta \to \pi/2$. Made too short, however, and the resulting large I_c will cause undesirable hysteresis in the differential resistance. In order to capture the non-hysteretic data, the temperature was intentionally elevated to decrease I_c and prevent stochastic flux "popping" at high screening currents. See Fig. 6.13(e). We present data from two samples: "Sample A," in which the length of each of the three junctions is $L \sim 1$ μm, and "Sample B," where $L \sim 2$ μm. Figure 6.13(a) shows a representative device schematic of the three-terminal junction. Figure 6.13(b)

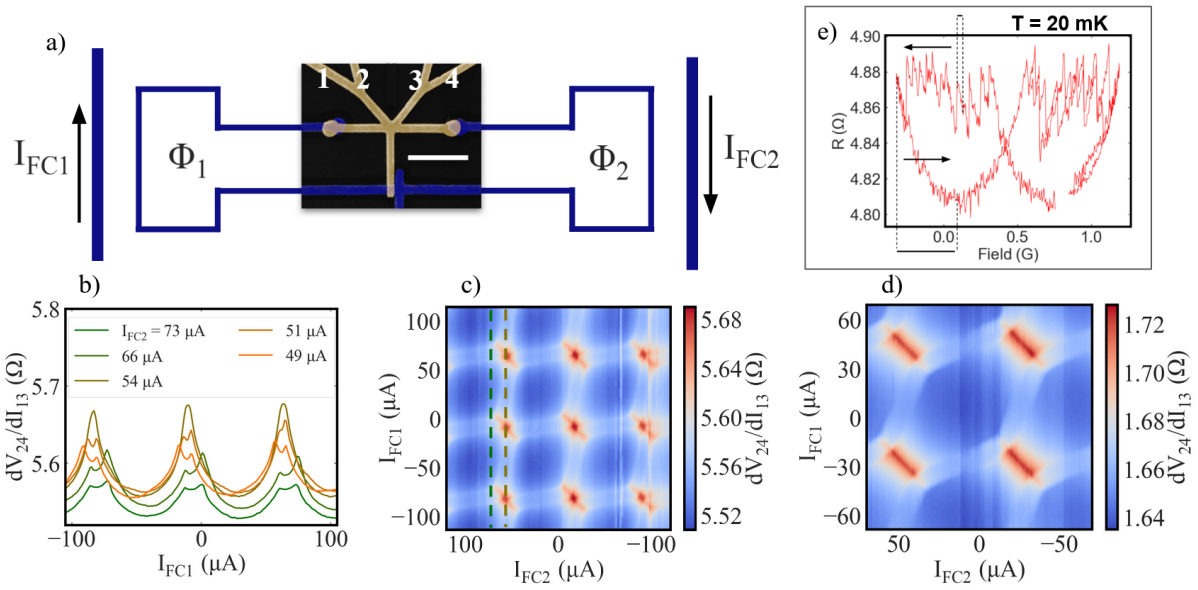

Figure 6.13: **Phase-biased three-terminal junction data.** (a) SEM image of Sample B connected to two independent flux loops. Scale bar is 1 μm. Normal leads are numbered. (b) dV/dI of Sample A as a function of coil bias I_{FC1} at different values of I_{FC2} measured at 600 mK. (c) dV/dI heat map as a function of I_{FC1} and I_{FC2} for Sample A. Vertical dotted lines correspond to $I_{\text{FC2}} = 73$ μA and 54 μA. (d) dV/dI heat map of Sample B taken at 300 mK. (e) Hysteretic magnetoresistance of flux loops at 20 mK. Arrows indicated direction of sweep. Two-level resistance associated with multiple stable energy levels. Figure adapted from Ref. [109].

shows the four-probe differential resistance of Sample A as a function of the current I_{FC1} through "Field Coil 1" at different values of the current I_{FC2} through "Field Coil 2." Immediately, one observes periodic oscillations and overlaying texture in the differential resistance that evolves with I_{FC2}. To draw out these features, we map the entire phase space in Fig. 6.13(c) by continuously sweeping I_{FC1} while incrementally stepping I_{FC2} by 1 μA over the course of six days.

Figure 6.13(c) shares similar features with the simulation shown in Fig. 6.11(c). Each period of ϕ_i corresponds to Φ_0 through each individual flux loop, and the somewhat localized regions of high resistance separate regions of low resistance. The most obvious difference from the simulations is the rhomboidal structure of the regions of high resistance that occur not at points defined by

$\phi_i = (2n+1)\pi$ but at points a slight distance away. In the simulations, narrow strips of high resistance bridge together localized regions of maximum resistance. The experimental data show similar strips, though these appear double-peaked in nature (see the curve associated with $I_{\text{FC2}} = 49\ \mu$A in Fig. 6.13(b), for example). Somewhat unexpectedly, it appears that simulations of Device 1 (Fig. 6.10) provide a better match to the data. We believe this is due to the finite width of the normal wires in the real device providing overlap between the injected quasiparticle current from the normal reservoirs and supercurrent between the junctions [109]. The diagonal "stretching" along $I_{\text{FC2}} \approx -I_{\text{FC1}}$ is even more obvious in the data collected on Sample B, shown in Fig. 6.13(d).

With the entire 2D phase space of a diffusive three-terminal junction mapped, we comment on the topological properties therein. First, because topologically distinct regions are predicted to exist around *complete* gap closings, we must first identify these points in the resistive heat map. As mentioned previously, the normal metal reservoirs added to this device prevent the Green's function from reaching the equator $\theta = \pi/2$ on the Bloch sphere, i.e. $N(0)$ will never vanish and the system will always exists in a gapless state. However, following the convention of Strambini *et al.*, if we redefine the gapped state as the longitudinal line associated with the *maximum* $\Re\theta$, then we may identify regions of minimum resistance in our data as topologically distinct. For example, the topological index associated with $(I_{\text{FC1}}, I_{\text{FC2}}) = (0\ \mu\text{A}, 0\ \mu\text{A})$ is distinct from that of $(I_{\text{FC1}}, I_{\text{FC2}}) = (0\ \mu\text{A}, -50\ \mu\text{A})$. To actually demonstrate the topological properties of the system, one would need to measure a quantized observable from the bulk-boundary correspondence [75]. While no such measurement is made here, the advantage of our particular device geometry is that we may freely traverse in any direction we wish in phase space in search of possible topological signature.

An exciting prospect for diffusive MTJJ comes from the relative easy in which additional superconducting terminals may be introduced. For instance, one imagines adding 4th superconducting

terminal such that the two flux loops do not share a normal arm as in Fig. 6.13(a). This would increase the dimensionality of phase space such that one could map the topology of a 3D "artificial" crystal. Adding terminals becomes even easier in current-biased junctions where supercurrent injector terminals may be placed at will to tune the correlated Josephson effects phenomena found within.

CHAPTER 7
CONCLUSIONS AND FUTURE WORK

There are several directions in which we could expand upon our findings on diffusive MTJJ. A natural progression towards an operational qubit is to incorporate SNS junctions into a high-frequency circuit to measure the microwave response as a function of supercurrent. Given our lab's access to a dry dilution refrigerator kitted with GHz frequency generators and readout electronics, it seems the unification of dc transport and microwave spectroscopy on proximity effect devices is closer than ever. While great effort has been put forth fabricating and post-processing SIS junctions with specific E_J (e.g. see Ref. [110]), we believe it could be more feasible to do the same with SNS junctions by simply controlling the length L of the normal metal wire. Furthermore, graphene-based qubits in the form of "gatemons" which combined the shunt capacitance and circuit nonlinearity into a single element have already been shown to be frequency-tunable in the GHz range [111], [112].

The author has spent considerable time fabricating hBN-encapsulated graphene-based devices in an attempt to create MTJJs with a *ballistic* normal metal weak link. A host of interesting physics may be probed in such a device, not least of which are the well-defined Andreev bound states where a different class of topological effects is predicted [69]. What could be done with diffusive metal could in principle be done with graphene. This includes recasting the role of the field coil as an inductive pick-up coil capable of responding to small ac signals in the flux loop. Such a multi-loop device could be used as a platform to investigate frequency-mixing between phase-biased Andreev interferometers.

Additionally, there appears to be an absence of publications on phase-dependent transport in

ballistic metals injected with diffusive quasiparticles. One potential advantage of hBN-encaspulated devices is the possibility to fabricate a metal electrode on top of the device as a tunnel contact to directly probe the local DOS. While we have shown one does not *require* a tunneling contact to observe interesting phase-dependent transport, the discovery of a reliable recipe to fabricate robust NIN junction onto SNS devices would be a boon to our lab's research goals.

In terms of SIS junctions, one could in principle determine E_C/E_J and the effective shunt resistance R by fitting the dependence of the phase diffusion resistance to current bias. This would give insight into how the qubit frequency responds to environments of arbitrary impedance. However, this calculation requires an exact description of the environmental admittance $Y(\omega)$ which may vary considerably depending on the measurement setup. Nonetheless, the quantum Langevin approach is a powerful tool to study Josephson-based devices in a variety of scenarios. In modeling $Y(\omega)$ for small junctions shunted by a lithographically defined resistor, for example, Joyez *et al.* suggest that the switching process is dominated not by thermal activation over the usual washboard barrier but the so-called *dissipation barrier* determined by an energy $\propto 1/RC$. This explained why distributions of temperature-sensitive I_{sw} were measured to be somewhat independent of E_T/E_J in their study [16]. This particular experiment reiterates two facts: (a) the RCSJ washboard potential may not provide a complete description for switching characteristics, including in the case where the particle mass is modeled equivalently to the total shunt capacitance, and (b) that independent *experimental* verification of the electronic temperature of junctions would strengthen interpretations of temperature-sensitive phase dynamics.

With respect to this later point, we have shown that the width of the measured quasiparticle branch strongly implies that junction electronic temperatures are at or below the temperature reported by our RuO_x thermometer. However, these retraceable features do not appear in every IV curve shown in Chapter 5. To be absolutely sure that elevated electronic temperatures do not give

spurious results, especially in temperature-sensitive switching current measurements, the junction itself must act as a primary thermometer. One possibility is to measure the Johnson noise of the zero-bias resistance. Given $R_0 \approx 1\ k\Omega$ at 20 mK, the Johnson noise $V_{\text{rms}}/\sqrt{Hz} = 0.03$ nV may be measured with an adequate amplifier chain in a cross-correlation noise experiment. Elevations above this voltage noise indicate higher temperatures.

In the RSCJ model, intrinsic capacitance and capacitive circuit elements are treated identically. From this perspective, one expects that amending the junction with macroscopic circuit elements would subsequently alter the phase fluctuations. Our dc transport findings on transmons suggest otherwise. Clearly, at least from the perspective of particle tunneling, there is a marked difference between the intrinsic capacitance formed from the junction barrier and the macroscopic lithographically defined shunt capacitor. Perhaps it is the "leaky" nature of the intrinsic capacitance that matters more for phase fluctuations than previously thought. One imagines the extreme scenario of a ~ 1 pF capacitor replacing the 100 fF shunt, perhaps with the use of interdigitated leads, to definitively prove that the shunt is inconsequential to phase diffusion. Alternatively, one imagines creating a transmon in which the junction itself acts as its own large capacitor as is the case with merged-element transmons [113], [114]. Phase diffusion measurements of such large-area junctions would be an interesting experiment to understand the role of intrinsic capacitance on phase fluctuations.

REFERENCES

[1] B. Josephson, "Possible new effects in superconductive tunnelling," *Physics Letters*, vol. 1, no. 7, pp. 251–253, Jul. 1962.

[2] P. W. Anderson and J. M. Rowell, "Probable observation of the josephson superconducting tunneling effect," *Physical Review Letters*, vol. 10, no. 6, pp. 230–232, Mar. 15, 1963.

[3] P. Krantz, M. Kjaergaard, F. Yan, T. P. Orlando, S. Gustavsson, and W. D. Oliver, "A quantum engineer's guide to superconducting qubits," *Applied Physics Reviews*, vol. 6, no. 2, p. 021 318, Jun. 2019.

[4] M. H. Devoret, J. M. Martinis, and J. Clarke, "Measurements of macroscopic quantum tunneling out of the zero-voltage state of a current-biased josephson junction," *Physical Review Letters*, vol. 55, no. 18, pp. 1908–1911, Oct. 28, 1985.

[5] J. M. Martinis, M. H. Devoret, and J. Clarke, "Energy-level quantization in the zero-voltage state of a current-biased josephson junction," *Physical Review Letters*, vol. 55, no. 15, pp. 1543–1546, Oct. 7, 1985.

[6] J. M. Martinis, S. Nam, J. Aumentado, and C. Urbina, "Rabi oscillations in a large josephson-junction qubit," *Physical Review Letters*, vol. 89, no. 11, p. 117 901, Aug. 21, 2002.

[7] Y. Nakamura, Y. A. Pashkin, and J. S. Tsai, "Coherent control of macroscopic quantum states in a single-cooper-pair box," *Nature*, vol. 398, no. 6730, pp. 786–788, Apr. 1999.

[8] M. Tinkham, *Introduction to Superconductivity: Second Edition* (Dover Books on Physics). Dover Publications, 2004, ISBN: 9780486435039.

[9] V. Ambegaokar and A. Baratoff, "Tunneling between superconductors," *Physical Review Letters*, vol. 10, no. 11, pp. 486–489, Jun. 1, 1963.

[10] K. Ryan, "Transport studies of superconductors for quantum applications," PhD thesis, Northwestern University, Evanston, IL, Dec. 2025.

[11] T. Van Duzer and C. W. Turner, *Principles of superconductive devices and circuits*. Elsevier, Jan. 1981.

[12] W. C. Stewart, "CURRENT-VOLTAGE CHARACTERISTICS OF JOSEPHSON JUNCTIONS," *Applied Physics Letters*, vol. 12, no. 8, pp. 277–280, Apr. 15, 1968.

[13] D. E. McCumber, "Effect of ac impedance on dc voltage-current characteristics of superconductor weak-link junctions," *Journal of Applied Physics*, vol. 39, no. 7, pp. 3113–3118, Jun. 1, 1968.

[14] R. L. Kautz and J. M. Martinis, "Noise-affected i-v curves in small hysteretic josephson junctions," *Physical Review B*, vol. 42, no. 16, pp. 9903–9937, Dec. 1, 1990.

[15] G. Y. Hu and R. F. O'Connell, "Low-voltage resistance in small josephson junctions," *Journal of Physics: Condensed Matter*, vol. 4, no. 48, p. 9635, Nov. 1992.

[16] P. Joyez, D. Vion, M. Götz, M. H. Devoret, and D. Esteve, "The josephson effect in nanoscale tunnel junctions," *Journal of Superconductivity*, vol. 12, no. 6, pp. 757–766, Dec. 1, 1999.

[17] U. K. Poulsen, "Quasiparticle interference current in josephson junctions," *Physics Letters A*, vol. 41, no. 3, pp. 195–196, Sep. 25, 1972.

[18] J. M. Martinis and R. L. Kautz, "Classical phase diffusion in small hysteretic josephson junctions," *Physical Review Letters*, vol. 63, no. 14, pp. 1507–1510, Oct. 2, 1989.

[19] A. O. Caldeira and A. J. Leggett, "Influence of dissipation on quantum tunneling in macroscopic systems," *Physical Review Letters*, vol. 46, no. 4, pp. 211–214, Jan. 26, 1981.

[20] Y. M. Ivanchenko and L. A. Zil'berman, "The josephson effect in small tunnel contacts," *Journal of Experimental and Theoretical Physics*, 1969.

[21] M. Iansiti, A. T. Johnson, W. F. Smith, H. Rogalla, C. J. Lobb, and M. Tinkham, "Charging energy and phase delocalization in single very small josephson tunnel junctions," *Physical Review Letters*, vol. 59, no. 4, pp. 489–492, Jul. 27, 1987.

[22] M. Iansiti, A. T. Johnson, C. J. Lobb, and M. Tinkham, "Crossover from josephson tunneling to the coulomb blockade in small tunnel junctions," *Physical Review Letters*, vol. 60, no. 23, pp. 2414–2417, Jun. 6, 1988.

[23] M. Iansiti, A. T. Johnson, C. J. Lobb, and M. Tinkham, "Quantum tunneling and low-voltage resistance in small superconducting tunnel junctions," *Physical Review B*, vol. 40, no. 16, pp. 11 370–11 373, Dec. 1, 1989.

[24] J. J. Sakurai and J. Napolitano, *Modern quantum mechanics*. Cambridge, 2020, OCLC: 1202949320, ISBN: 978-1-108-64592-8.

[25] J. Koch, T. M. Yu, J. Gambetta, *et al.*, "Charge-insensitive qubit design derived from the cooper pair box," *Physical Review A*, vol. 76, no. 4, p. 042 319, Oct. 12, 2007.

[26] R. Acharya, D. A. Abanin, L. Aghababaie-Beni, *et al.*, "Quantum error correction below the surface code threshold," *Nature*, vol. 638, no. 8052, pp. 920–926, Feb. 2025.

[27] Y. Kim, A. Eddins, S. Anand, *et al.*, "Evidence for the utility of quantum computing before fault tolerance," *Nature*, vol. 618, no. 7965, pp. 500–505, Jun. 2023.

[28] M. Bal, A. A. Murthy, S. Zhu, *et al.*, "Systematic improvements in transmon qubit coherence enabled by niobium surface encapsulation," *npj Quantum Information*, vol. 10, no. 1, p. 43, Apr. 26, 2024.

[29] W.-S. Lu, K. Kalashnikov, P. Kamenov, T. J. DiNapoli, and M. E. Gershenson, "Phase diffusion in low-ej josephson junctions at milli-kelvin temperatures," *Electronics*, vol. 12, no. 2, p. 416, Jan. 2023.

[30] J. A. Blackburn, M. Cirillo, and N. Grønbech-Jensen, "A survey of classical and quantum interpretations of experiments on josephson junctions at very low temperatures," *Physics Reports*, A survey of classical and quantum interpretations of experiments on Josephson junctions at very low temperatures, vol. 611, pp. 1–33, Feb. 5, 2016.

[31] D. Esteve, M. H. Devoret, and J. M. Martinis, "Effect of an arbitrary dissipative circuit on the quantum energy levels and tunneling of a josephson junction," *Physical Review B*, vol. 34, no. 1, pp. 158–163, Jul. 1, 1986.

[32] D. Averin and K. Likharev, "Single electronics: A correlated transfer of single electrons and cooper pairs in systems of small tunnel junctions," in *Modern Problems in Condensed Matter Sciences*, vol. 30, Elsevier, 1991, pp. 173–271, ISBN: 978-0-444-88454-1.

[33] M. Watanabe and D. B. Haviland, "Quantum effects in small-capacitance single josephson junctions," *Physical Review B*, vol. 67, no. 9, p. 094 505, Mar. 17, 2003.

[34] L. S. Kuzmin, Y. V. Nazarov, D. B. Haviland, P. Delsing, and T. Claeson, "Coulomb blockade and incoherent tunneling of cooper pairs in ultrasmall junctions affected by strong quantum fluctuations," *Physical Review Letters*, vol. 67, no. 9, pp. 1161–1164, Aug. 26, 1991.

[35] G. W. Ford, J. T. Lewis, and R. F. O'Connell, "Quantum langevin equation," *Physical Review A*, vol. 37, no. 11, Jun. 1, 1988.

[36] V. Balakrishnan, *Elements of nonequilibrium statistical mechanics*. Springer, 2008, vol. 3.

[37] V. Chandrasekhar, "Current dependence of the low bias resistance of small capacitance josephson junctions," *Physics Letters A*, vol. 507, p. 129 493, May 28, 2024.

[38] M. Wisne, Y. Deng, H. Cansizoglu, C. Kopas, J. Y. Mutus, and V. Chandrasekhar, "Transport signatures of phase fluctuations in superconducting qubits," *Materials for Quantum Technology*, vol. 4, no. 4, p. 046 001, Dec. 2024.

[39] D. J. Thouless, "Maximum metallic resistance in thin wires," *Physical Review Letters*, vol. 39, no. 18, pp. 1167–1169, Oct. 31, 1977.

[40] V. Chandrasekhar, "Proximity-coupled systems: Quasiclassical theory of superconductivity," in *Superconductivity: Conventional and Unconventional Superconductors*, K. H. Bennemann and J. B. Ketterson, Eds., Berlin, Heidelberg: Springer, 2008, pp. 279–313, ISBN: 978-3-540-73253-2.

[41] B. Pannetier and H. Courtois, "Andreev reflection and proximity effect," *Journal of Low Temperature Physics*, vol. 118, no. 5, pp. 599–615, Mar. 1, 2000.

[42] E. Ben-Jacob, D. J. Bergman, B. J. Matkowsky, and Z. Schuss, "Lifetime of oscillatory steady states," *Physical Review A*, vol. 26, no. 5, pp. 2805–2816, Nov. 1, 1982.

[43] I. Giaever and K. Megerle, "Study of superconductors by electron tunneling," *Physical Review*, vol. 122, no. 4, pp. 1101–1111, May 15, 1961.

[44] G. E. Blonder, M. Tinkham, and T. M. Klapwijk, "Transition from metallic to tunneling regimes in superconducting microconstrictions: Excess current, charge imbalance, and supercurrent conversion," *Physical Review B*, vol. 25, no. 7, pp. 4515–4532, Apr. 1, 1982.

[45] A. F. Andreev, "Thermal conductivity of the intermediate state of superconductors," *Zh. Eksperim. i Teor. Fiz.*, vol. Vol: 46, May 1964.

[46] C. W. J. Beenakker, "Random-matrix theory of quantum transport," *Reviews of Modern Physics*, vol. 69, no. 3, pp. 731–808, Jul. 1, 1997.

[47] A. A. Golubov, M. Y. Kupriyanov, and E. Il'ichev, "The current-phase relation in josephson junctions," *Reviews of Modern Physics*, vol. 76, no. 2, pp. 411–469, Apr. 26, 2004.

[48] Y. Nambu, "Quasi-particles and gauge invariance in the theory of superconductivity," *Physical Review*, vol. 117, no. 3, pp. 648–663, Feb. 1960.

[49] W. Belzig, F. K. Wilhelm, C. Bruder, G. Schön, and A. D. Zaikin, "Quasiclassical green's function approach to mesoscopic superconductivity," *Superlattices and Microstructures*, vol. 25, no. 5, pp. 1251–1288, May 1999.

[50] G. Eilenberger, "Transformation of gorkov's equation for type ii superconductors into transport-like equations," *Zeitschrift für Physik A Hadrons and nuclei*, vol. 214, no. 2, pp. 195–213, Apr. 1968.

[51] K. D. Usadel, "Generalized diffusion equation for superconducting alloys," *Physical Review Letters*, vol. 25, no. 8, pp. 507–509, Aug. 24, 1970.

[52] L. Keldysh, "Diagram technique for nonequilibrium processes," *JETP*, 1965.

[53] A. Schmid and G. Schön, "Linearized kinetic equations and relaxation processes of a superconductor near tc," *Journal of Low Temperature Physics*, vol. 20, no. 1, pp. 207–227, Jul. 1, 1975.

[54] V. Chandrasekhar, "Tuning the fundamental periodicity of the current-phase relation in multiterminal diffusive josephson junctions," *Physical Review B*, vol. 112, no. 10, Sep. 2025.

[55] V. L. M. Yu. Kuprianov, "Influence of boundary transparency on the critical current of "dirty" ss's structures," *JETP*, 1987.

[56] P. Virtanen and T. Heikkilä, "Thermoelectric effects in superconducting proximity structures," *Applied Physics A*, vol. 89, no. 3, pp. 625–637, Nov. 1, 2007.

[57] M. Eschrig, "Distribution functions in nonequilibrium theory of superconductivity and andreev spectroscopy in unconventional superconductors," *Physical Review B*, vol. 61, no. 13, pp. 9061–9076, Apr. 1, 2000.

[58] J. C. Hammer, J. C. Cuevas, F. S. Bergeret, and W. Belzig, "Density of states and supercurrent in diffusive SNS junctions: Roles of nonideal interfaces and spin-flip scattering," *Physical Review B*, vol. 76, no. 6, p. 064 514, Aug. 14, 2007.

[59] V. Chandrasekhar, "Probing the topological band structure of diffusive multiterminal josephson junction devices with conductance measurements," *Applied Physics Letters*, vol. 121, no. 22, p. 222 601, Dec. 1, 2022.

[60] A. D. Zaikin and G. F. Zharkov, "Theory of wide dirty SNS junctions," *Soviet Journal Low Temperature Physics*, vol. 7, no. 3, pp. 184–185, Mar. 1, 1981.

[61] F. Zhou, P. Charlat, B. Spivak, and B. Pannetier, "Density of states in superconductor-normal metal-superconductor junctions," *Journal of Low Temperature Physics*, vol. 110, no. 3, pp. 841–850, Feb. 1, 1998.

[62] D. A. Ivanov, R. von Roten, and G. Blatter, "Minigap in a long disordered SNS junction: Analytical results," *Physical Review B*, vol. 66, no. 5, p. 052 507, Aug. 9, 2002.

[63] H. le Sueur, P. Joyez, H. Pothier, C. Urbina, and D. Esteve, "Phase controlled superconducting proximity effect probed by tunneling spectroscopy," *Physical Review Letters*, vol. 100, no. 19, p. 197 002, May 14, 2008.

[64] S.-K. Yip, "Energy-resolved supercurrent between two superconductors," *Physical Review B*, vol. 58, no. 9, pp. 5803–5807, Sep. 1998.

[65] L. Weithofer, P. Recher, and T. L. Schmidt, "Electron transport in multiterminal networks of majorana bound states," *Physical Review B*, vol. 90, no. 20, p. 205 416, Nov. 17, 2014.

[66] B. van Heck, A. R. Akhmerov, F. Hassler, M. Burrello, and C. W. J. Beenakker, "Coulomb-assisted braiding of majorana fermions in a josephson junction array," *New Journal of Physics*, vol. 14, no. 3, p. 035 019, Mar. 2012.

[67] A. Zazunov, R. Egger, M. Alvarado, and A. L. Yeyati, "Josephson effect in multiterminal topological junctions," *Physical Review B*, vol. 96, no. 2, p. 024 516, Jul. 26, 2017.

[68] L. Fu and C. L. Kane, "Superconducting proximity effect and majorana fermions at the surface of a topological insulator," *Physical Review Letters*, vol. 100, no. 9, p. 096 407, Mar. 6, 2008.

[69] R.-P. Riwar, M. Houzet, J. S. Meyer, and Y. V. Nazarov, "Multi-terminal josephson junctions as topological matter," *Nature Communications*, vol. 7, no. 1, p. 11 167, Apr. 4, 2016, Number: 1.

[70] E. Strambini, S. D'Ambrosio, F. Vischi, F. S. Bergeret, Y. V. Nazarov, and F. Giazotto, "The ω-SQUIPT as a tool to phase-engineer josephson topological materials," *Nature Nanotechnology*, vol. 11, no. 12, pp. 1055–1059, Dec. 1, 2016.

[71] M. Amundsen, J. A. Ouassou, and J. Linder, "Analytically determined topological phase diagram of the proximity-induced gap in diffusive n-terminal josephson junctions," *Scientific Reports*, vol. 7, no. 1, p. 40 578, Jan. 17, 2017, Number: 1.

[72] F. Vischi, M. Carrega, E. Strambini, *et al.*, "Coherent transport properties of a three-terminal hybrid superconducting interferometer," *Physical Review B*, vol. 95, no. 5, p. 054 504, Feb. 13, 2017.

[73] H.-Y. Xie, M. G. Vavilov, and A. Levchenko, "Weyl nodes in andreev spectra of multi-terminal josephson junctions: Chern numbers, conductances, and supercurrents," *Physical Review B*, vol. 97, no. 3, p. 035 443, Jan. 31, 2018.

[74] J. A. Sauls, "Andreev bound states and their signatures," *Philosophical Transactions of the Royal Society A: Mathematical, Physical and Engineering Sciences*, vol. 376, no. 2125, p. 20 180 140, Jun. 20, 2018.

[75] X.-L. Qi and S.-C. Zhang, "Topological insulators and superconductors," *Reviews of Modern Physics*, vol. 83, no. 4, pp. 1057–1110, Oct. 2011.

[76] N. Pankratova, H. Lee, R. Kuzmin, *et al.*, "Multiterminal josephson effect," *Physical Review X*, vol. 10, no. 3, p. 031 051, Sep. 2, 2020.

[77] E. G. Arnault, T. F. Q. Larson, A. Seredinski, *et al.*, "Multiterminal inverse AC josephson effect," *Nano Letters*, vol. 21, no. 22, pp. 9668–9674, Nov. 2021.

[78] A. W. Draelos, M.-T. Wei, A. Seredinski, *et al.*, "Supercurrent flow in multiterminal graphene josephson junctions," *Nano Letters*, vol. 19, no. 2, pp. 1039–1043, Feb. 2019.

[79] E. G. Arnault, S. Idris, A. McConnell, *et al.*, "Dynamical stabilization of multiplet supercurrents in multiterminal josephson junctions," *Nano Letters*, vol. 22, no. 17, pp. 7073–7079, Sep. 2022.

[80] G. V. Graziano, J. S. Lee, M. Pendharkar, C. J. Palmstrøm, and V. S. Pribiag, "Transport studies in a gate-tunable three-terminal josephson junction," *Physical Review B*, vol. 101, no. 5, p. 054 510, Feb. 24, 2020.

[81] M. Gupta, G. V. Graziano, M. Pendharkar, *et al.*, "Gate-tunable superconducting diode effect in a three-terminal josephson device," *Nature Communications*, vol. 14, no. 1, p. 3078, May 2023.

[82] Y. Cohen, Y. Ronen, J.-H. Kang, *et al.*, "Nonlocal supercurrent of quartets in a three-terminal josephson junction," *Proceedings of the National Academy of Sciences of the United States of America*, vol. 115, no. 27, pp. 6991–6994, Jul. 3, 2018.

[83] K.-F. Huang, Y. Ronen, R. Mélin, *et al.*, "Evidence for 4e charge of cooper quartets in a biased multi-terminal graphene-based josephson junction," *Nature Communications*, vol. 13, no. 1, p. 3032, May 2022.

[84] A. H. Pfeffer, J. E. Duvauchelle, H. Courtois, R. Mélin, D. Feinberg, and F. Lefloch, "Subgap structure in the conductance of a three-terminal josephson junction," *Physical Review B*, vol. 90, no. 7, p. 075 401, Aug. 4, 2014.

[85] M. Gupta, V. Khade, C. Riggert, *et al.*, "Evidence for π-shifted cooper quartets and few-mode transport in PbTe nanowire three-terminal josephson junctions," *Nano Letters*, vol. 24, no. 44, pp. 13 903–13 910, Nov. 2024.

[86] P. Cadden-Zimansky, "Nonlocal coherence in normal metal-superconductor nanostructures," PhD thesis, Northwestern University, Evanston, IL, Dec. 2008.

[87] T. Noh, "Nonlocal correlations in a proximity-coupled normal metal," PhD thesis, Northwestern University, Evanston, IL, Dec. 2019.

[88] J. Eom, "Electrical properties of mesoscopic spin glasses," PhD thesis, Northwestern University, Evanston, IL, Jun. 1998.

[89] C.-J. Chien, "Transport phenomena near the normal-metal/superconducting interface in mesoscopic devices," PhD thesis, Northwestern University, Evanston, IL, Dec. 1998.

[90] J. Aumentado, "Nonequilibrium and quantum transport phenomena in mesoscopic ferromagnet/superconductor heterostructures," PhD thesis, Northwestern University, Evanston, IL, Dec. 2000.

[91] Z. Jiang, "Thermal transport near the normal-metal/superconductor interface in mesoscopic devices," PhD thesis, Northwestern University, Evanston, IL, Jun. 2005.

[92] F. Lecocq, I. M. Pop, Z. Peng, *et al.*, "Junction fabrication by shadow evaporation without a suspended bridge," *Nanotechnology*, vol. 22, no. 31, p. 315 302, Jul. 2011.

[93] G. J. Dolan, "Offset masks for lift-off photoprocessing," *Applied Physics Letters*, vol. 31, no. 5, pp. 337–339, Sep. 1, 1977.

[94] V. Chandrasekhar, "Electron quantum interfernce in small metal wires and loops," PhD thesis, Yale University, May 1989.

[95] N. W. Ashcroft and N. D. Mermin, *Solid State Physics*. Holt-Saunders, 1976.

[96] V. Chandrasekhar, "Current dependence of the low bias resistance of small capacitance josephson junctions," *Physics Letters A*, vol. 507, p. 129 493, May 28, 2024.

[97] M. H. Devoret, D. Esteve, H. Grabert, G.-L. Ingold, H. Pothier, and C. Urbina, "Effect of the electromagnetic environment on the coulomb blockade in ultrasmall tunnel junctions," *Physical Review Letters*, vol. 64, no. 15, pp. 1824–1827, Apr. 1990.

[98] A. A. Murthy, M. Bal, M. J. Bedzyk, *et al.*, *Identifying materials-level sources of performance variation in superconducting transmon qubits*, 2025. arXiv: 2503.14424 [quant-ph].

[99] V. Chandrasekhar, Z. Ovadyahu, and R. Webb, "Single-electron charging effects in insulating wires," *Physical Review Letters*, vol. 67, no. 20, pp. 2862–2865, Nov. 1991.

[100] A. Nersisyan, S. Poletto, N. Alidoust, *et al.*, *Manufacturing low dissipation superconducting quantum processors*, 2019. arXiv: 1901.08042 [quant-ph].

[101] P. Dubos, H. Courtois, B. Pannetier, F. K. Wilhelm, A. D. Zaikin, and G. Schön, "Josephson critical current in a long mesoscopic s-n-s junction," *Physical Review B*, vol. 63, no. 6, p. 064 502, Jan. 18, 2001.

[102] M. Wisne and V. Chandrasekhar, "Supercurrent tuning of the josephson coupling energy," *Physical Review B*, vol. 113, no. 5, Feb. 2026.

[103] J. J. A. Baselmans, A. F. Morpurgo, B. J. van Wees, and T. M. Klapwijk, "Reversing the direction of the supercurrent in a controllable josephson junction," *Nature*, vol. 397, no. 6714, pp. 43–45, Jan. 1999.

[104] M. P. Nowak, M. Wimmer, and A. R. Akhmerov, "Supercurrent carried by nonequilibrium quasiparticles in a multiterminal josephson junction," *Physical Review B*, vol. 99, no. 7, p. 075 416, Feb. 2019.

[105] G. Yue, C. Zhang, E. D. Huemiller, *et al.*, "Signatures of majorana bound states in the diffraction patterns of extended superconductor–topological insulator–superconductor josephson junctions," *Physical Review B*, vol. 109, no. 9, p. 094 511, Mar. 2024.

[106] J. C. Cuevas and F. S. Bergeret, "Magnetic interference patterns and vortices in diffusive SNS junctions," *Physical Review Letters*, vol. 99, no. 21, p. 217 002, Nov. 2007.

[107] M. J. Black and V. Chandrasekhar, "Influence of temperature-dependent inelastic scattering on the superconducting proximity effect," *Europhysics Letters (EPL)*, vol. 50, no. 2, pp. 257–263, Apr. 2000.

[108] P. Cadden-Zimansky, Z. Jiang, and V. Chandrasekhar, "Thermopower oscillation symmetries in a double-loop andreev interferometer," *Physica E: Low-dimensional Systems and Nanostructures*, vol. 40, no. 1, pp. 155–159, Oct. 2007.

[109] M. Wisne, Y. Deng, I. M. A. Lilja, P. J. Hakonen, and V. Chandrasekhar, "Mapping the topological proximity-induced gap in multiterminal josephson junctions," *Physical Review Letters*, vol. 133, no. 24, p. 246 601, Dec. 2024.

[110] J. B. Hertzberg, E. J. Zhang, S. Rosenblatt, *et al.*, "Laser-annealing josephson junctions for yielding scaled-up superconducting quantum processors," *npj Quantum Information*, vol. 7, no. 1, p. 129, Aug. 2021.

[111] L. Casparis, T. W. Larsen, M. S. Olsen, *et al.*, "Gatemon benchmarking and two-qubit operations," *Phys. Rev. Lett.*, vol. 116, p. 150 505, 15 Apr. 2016.

[112] N. Aparicio, S. Messelot, E. Bonet-Orozco, *et al.*, "Gate-tunable spectrum and charge dispersion mitigation in a graphene superconducting qubit," *Phys. Rev. Lett.*, vol. 135, p. 266 001, 26 Dec. 2025.

[113] H. Mamin, E. Huang, S. Carnevale, *et al.*, "Merged-element transmons: Design and qubit performance," *Phys. Rev. Appl.*, vol. 16, p. 024 023, 2 Aug. 2021.

[114] R. Zhao, S. Park, T. Zhao, *et al.*, "Merged-element transmon," *Phys. Rev. Appl.*, vol. 14, p. 064 006, 6 Dec. 2020.